

Washington University in St. Louis

Washington University Open Scholarship

Arts & Sciences Electronic Theses and
Dissertations

Arts & Sciences

Summer 8-15-2020

Separating Signal from Noise in High-Density Diffuse Optical Tomography

Arefeh Sherafati

Washington University in St. Louis

Follow this and additional works at: https://openscholarship.wustl.edu/art_sci_etds



Part of the [Nanoscience and Nanotechnology Commons](#), and the [Physics Commons](#)

Recommended Citation

Sherafati, Arefeh, "Separating Signal from Noise in High-Density Diffuse Optical Tomography" (2020). *Arts & Sciences Electronic Theses and Dissertations*. 2344.
https://openscholarship.wustl.edu/art_sci_etds/2344

This Dissertation is brought to you for free and open access by the Arts & Sciences at Washington University Open Scholarship. It has been accepted for inclusion in Arts & Sciences Electronic Theses and Dissertations by an authorized administrator of Washington University Open Scholarship. For more information, please contact digital@wumail.wustl.edu.

WASHINGTON UNIVERSITY IN ST. LOUIS

Department of Physics

Dissertation Examination Committee:

Ralf Wessel, Chair

Joseph P. Culver, Co-Chair

Tamara Hershey

Shankar Mukherji

Jonathan E. Peelle

Abraham Z. Snyder

Separating Signal from Noise in High-Density Diffuse Optical Tomography

by

Arefeh Sherafati

A dissertation presented to
The Graduate School
of Washington University in
partial fulfillment of the
requirements for the degree
of Doctor of Philosophy

August 2020
St. Louis, Missouri

© 2020, Arefeh Sherafati

Table of Contents

List of Figures	xiv
List of Tables	xvii
Acknowledgments.....	xviii
Abstract	xxii
Chapter 1: Introduction	1
Chapter 2: Data Processing Methods for High-Density Diffuse Optical Tomography	6
2.1 Basic ideas behind functional near-infrared imaging.....	6
2.2 Modified Beer-Lambert law	9
2.3 Forward model for the diffusion of near-infrared light	10
2.4 Inverse problem	13
2.5 HD-DOT data processing pipeline	14
2.5.1 Log-mean of light-levels	15
2.5.2 Noisy channel detection	16
2.5.3 Bandpass filtering	17
2.5.4 Superficial signal regression	17
2.5.5 Secondary low-pass filtering and resampling	18
2.5.6 Light modeling.....	19
2.5.7 Image reconstruction.....	20
2.5.8 Spectroscopy	22
2.5.9 Spatial resampling.....	23
2.5.10 Spatial smoothing.....	23
2.6 Conclusion.....	25
Chapter 3: Global Motion Detection and Censoring in High-density Diffuse Optical Tomography	27
3.1 Introduction	27
3.2 Methods	30
3.2.1 Novel motion detection methods	30
3.2.1.1 The global variance of the temporal derivatives (GVTD)	30
3.2.1.2 Independent measurement of head motion	30
3.2.1.3 Angular rotation	31

3.2.1.4 Artifact-to-background ratio (ABR)	31
3.2.2 Motion removal methods	32
3.2.2.1 Motion censoring using GVTD.....	32
3.2.2.2 Correlation-based signal improvement (CBSI).....	32
3.2.2.3 Targeted principal component analysis (tPCA)	32
3.2.2.4 Wavelet filtering	33
3.2.2.5 Kurtosis-based wavelet filtering (kbWF).....	33
3.2.2.6 Hybrid (Spline + Savitzky Golay)	33
3.2.2.7 Temporal derivative distribution repair (TDDR).....	34
3.2.3 Datasets and their objective	34
3.2.4 HD-DOT systems, image reconstruction, and spectroscopy.....	35
3.2.5 Functional MRI (fMRI) system and imaging.....	36
3.2.6 Paradigms.....	36
3.2.7 HD-DOT pre-processing.....	37
3.2.8 fMRI pre-processing	38
3.2.9 Statistical analysis	39
3.2.9.1 HW task response mapping in datasets 1, 2, and 3	39
3.2.9.2 Seed-based correlation analysis of functional connectivity in datasets 1 and 4.....	40
3.2.9.3 Similarity metric	40
3.2.9.4 Receiver operator characteristic curve.....	40
3.3 Results	41
3.3.1 Effect of motion artifacts on HD-DOT data	41
3.3.2 GVTD and its correlation with the head angular rotation.....	43
3.3.3 Motion detection strategy using GVTD.....	47
3.3.4 Determining the best stage for performing GVTD-based motion detection and censoring.....	49
3.3.5 Indexing data quality with GVTD in task HD-DOT data by comparison against fMRI	51
3.3.6 Comparison between motion removal methods applied to HW task HD-DOT data	54
3.3.7 Comparison between motion removal methods applied to resting state HD-DOT data	58
3.4 Discussion	61
3.4.1 A general summary of the novel strategies and findings	61
3.4.2 Optimizing the implementation of GVTD in the HD-DOT processing pipeline	62
3.4.3 Evaluation and validation of denoising through comparisons to fMRI	63
3.4.4 On the different performance of motion correction methods in fNIRS literature.....	64

3.4.5 Strengths and limitations of the GVTB-based motion censoring	65
3.4.6 Summarizing the consensus regarding the top-performing denoising strategies in the fNIRS literature	66
3.5 Conclusion.....	67
Chapter 4: Mapping Deep Brain Stimulation's Impact on Cortical Networks Using HD-DOT ..	68
4.1 Introduction	68
4.2 Methods	71
4.2.1 Subjects	71
4.2.2 Study design.....	72
4.2.3 HD-DOT system	73
4.2.4 Functional MRI (fMRI) system	75
4.2.5 Paradigms (fMRI and HD-DOT)	75
4.2.6 Data processing	76
4.2.6.1 HD-DOT pre-processing.....	76
4.2.6.2 fMRI pre-processing	77
4.2.7 Motion and tremor censoring.....	78
4.2.8 Subject-specific light modeling	78
4.2.9 Statistical analysis	79
4.2.9.1 Hearing words and visual task response mapping	79
4.2.9.2 Seed-based correlation analysis of functional connectivity in resting state data	80
4.2.9.3 Functional connectivity analysis.....	80
4.2.10 Behavioral measurements	81
4.2.10.1 Motor measurements.....	81
4.2.10.2 Cognitive measurements.....	81
4.3 Results	81
4.3.1 The effects of motion censoring on resting state FC mapping.....	81
4.3.2 Cross-modality comparison in mapping single subject task activations.....	85
4.3.3 Mapping auditory and visual task activations.....	86
4.3.4 Mapping resting state	87
4.3.5 DBS STN within and between network FC	88
4.3.6 DBS STN activation.....	89
4.4 Discussion	92
4.4.1 Regional cortical effects of DBS STN	92

4.4.2 Mapping cortical networks in PD	93
4.4.3 Cortical networks in DBS STN.....	94
4.4.4 Limitations and future directions	96
4.5 Conclusion.....	97
Chapter 5: Mapping Neural Mechanisms Underlying Speech Perception in Listeners with Cochlear Implants Using HD-DOT	98
5.1 Introduction	98
5.2 Methods.....	100
5.2.1 Dataset.....	100
5.2.2 HD-DOT system	100
5.2.3 Experimental design.....	101
5.2.4 Paradigms.....	103
5.2.4.1 Hearing words.....	103
5.2.4.2 Sentences and noise	104
5.2.4.3 Movie watching	104
5.2.4.4 Spatial working memory.....	105
5.2.5 Data processing.....	105
5.2.6 Hearing words task response mapping.....	106
5.2.7 Sentence and noise response mapping	107
5.2.8 Audiovisual feature extraction from the movie viewing task	107
5.3 Results	108
5.3.1 Mapping the brain response to the hearing words task	108
5.3.2 Mapping the brain response to the sentences and noise-vocoded speech	108
5.3.3 Mapping the brain response to movie features	109
5.3.4 Mapping the brain response to all speech-related paradigms	111
5.3.5 Mapping the brain response to the spatial working memory task.....	112
5.3.6 Statistical analysis and group differences for the hearing words task.....	113
5.3.7 Behavioral measurements	114
5.3.7.1 Speech intelligibility	115
5.4 Discussion	115
5.5 Conclusion.....	117
Chapter 6: Conclusion.....	119
Appendix A: Supplementary Materials for Chapter 3	122

A.1 Finding the histogram mode based on the parabolic interpolation	128
A.2 Finding the mode of GVTD values based on the kernel density estimation.....	129
Appendix B: Supplementary Materials for Chapter 5	131
B.1 Data quality measures.....	131
B.2 Linear logarithmic falloff	131
B.3 Presence of the heartbeat frequency in the signal.....	133
B.4 Motion detection using GVTD	134
References/Bibliography/Works Cited	135

List of Figures

Figure 2.1: Hemoglobin absorption spectra	7
Figure 2.2: Oxy, deoxy, and total hemoglobin response functions	9
Figure 2.3: Near-infrared light diffusion	11
Figure 2.4: HD-DOT data processing overview	15
Figure 2.5: Noisy channel detection	16
Figure 2.6: Superficial signal regression	18
Figure 2.7: HD-DOT data processing pipeline	26
Figure 3.1: Effects of head motion on HD-DOT optode-scalp coupling	30
Figure 3.2: Effects of head motion on single-channel HD-DOT measurements	42
Figure 3.3: Data-driven vs. direct measures of head motion	44
Figure 3.4: Efficacy of GVTD in motion detection	47
Figure 3.5: Motion threshold determination using GVTD	49
Figure 3.6: Implementing GVTD in HD-DOT data processing pipeline	51
Figure 3.7: Indexing motion using GVTD in HD-DOT hearing words HbO ₂ maps	54
Figure 3.8: Efficacy of motion removal methods in task HD-DOT data	57
Figure 3.9: Efficacy of motion removal methods in resting state HD-DOT data	60
Figure 4.1: Data quality of HD-DOT vs. sparse NIRS	70
Figure 4.2: DOT-DBS study design	73
Figure 4.3: HD-DOT measurement array and field of view	74
Figure 4.4: HD-DOT head modeling steps in DBS patients	79

Figure 4.5: Effects of motion censoring on resting state FC HD-DOT data	84
Figure 4.6: Motion censoring increases the similarity of HD-DOT FC maps to fMRI	85
Figure 4.7: More reliable HD-DOT single subject maps using subject-specific light models	86
Figure 4.8: Task responses in controls with HD-DOT and fMRI and in PD with HD-DOT	87
Figure 4.9: Resting state FC in controls with HD-DOT and fMRI and in PD with HD-DOT ...	88
Figure 4.10: Within and between network FC differences in PD DBS using HD-DOT.....	89
Figure 4.11: DBS activation study.....	91
Figure 4.12: Increased spatial variance in HD-DOT maps in PD DBS with tremor	92
Figure 5.1: Schematic of the HD-DOT measurement array and field of view	101
Figure 5.2: CI-DOT study design	103
Figure 5.3: Hearing words task response mapping in controls and CI users	108
Figure 5.4: Sentence and noise task response mapping in controls and CI users	109
Figure 5.5: Movie feature mapping in controls and CI users	111
Figure 5.6: Summarizing the response to all speech paradigms in controls and CI users	112
Figure 5.7: Defining the left DLPFC ROI using the spatial working memory task	113
Figure 5.8: ROI-based analysis for the hearing words task in controls vs. CI users	114
Figure 5.9: Speech intelligibility score across controls and CI users	115
Figure A.1: Motion removal methods in HD-DOT data processing pipeline	122
Figure A.2: The placement of the motion sensor on HD-DOT cap	123
Figure A.3: The ROC curves for signal amplitudes and windowed signal amplitudes	123
Figure A.4: Motion censoring process for the hearing words task	124
Figure A.5: Indexing motion using GVTD in HD-DOT hearing words HbR maps	125

Figure A.6: Efficiency of motion removal methods in task HD-DOT data with different motion levels; thresholded.....	126
Figure A.7: Efficiency of motion removal methods in task HD-DOT data with different motion levels; no threshold	127
Figure A.8: Parabolic interpolation	129
Figure B.1: Examples of a good and a bad light falloff plot in HD-DOT data	132
Figure B.2: Examples of a good and a bad heartbeat SNR plot in HD-DOT data	133
Figure B.3: Examples of GVTD time-traces for a low-motion and a high-motion HD-DOT data	134

List of Tables

Table 2.1: Optical properties of segmented head tissue	20
Table 2.2: Extinction coefficients of HbO ₂ and HbR for 750 nm and 850 nm light.....	22
Table 3.1: Demographic information	35
Table 3.2: Percent of the noisy measurements across five different instructed movements	42
Table 3.3: The AUC of the ROC curves for different motion detection methods	45
Table 4.1: A comparison of imaging modalities for studying PD with DBS	69
Table A.1: List of the parameters for motion correction in task data	128
Table A.2: List of the parameters for motion correction in resting state data	128

Acknowledgments

I am sincerely grateful for all my teachers who taught me how to think and how to learn. First and foremost, I would like to thank my Ph.D. adviser Dr. Joseph Culver for giving me the opportunity to work in his lab and for being such an amazing human being and mentor for me for five years. I cannot thank him enough for all the opportunities he created for me to grow and for his deep understanding beyond scientific matters that made this journey enjoyable for me with all its difficulties. I very much appreciated the flexible working hours in his lab and the relaxed research environment he created, which made research fun and not stressful. I couldn't visit my family for five years because of the travel ban for the Iranians in the U.S., and I cannot thank Joe enough for always listening to my concerns and for motivating me to finish this journey.

I would like to thank Dr. Tamara Hershey, my co-PI in the DOT-DBS project, and her team of collaborators including Dr. Mwiza Ushe, Dr. Sarah Eisenstein, Heather Lugar, Tasha Doty, Samantha Ranck, Beth Beato, Dr. Amjad Samara, Jonathan Koller and other members for making this highly interdisciplinary project possible. Working on the DOT-DBS project and submitting and receiving an R01 NIH grant with Dr. Hershey was an unforgettable experience for me.

I would also like to thank Dr. Jonathan Peelle, my co-PI in the CI-DOT project, for his amazing mentorship and positive attitude. I also thank Dr. Jill Firszt, Dr. Mahlega Hassanpour, Noel Dwyer, and Aahana Bajracharya for their contributions to the CI-DOT project.

Special thanks to Dr. Abraham Snyder for spending endless hours reading and editing my manuscripts, helping me understand different aspects of the fMRI data processing, and for trying to facilitate my publication process.

I would also like to thank the members of Wash. U. physics department for the welcoming environment throughout these years, and for celebrating the Iranian new year, Norouz, with us

every spring. Special thanks to Sarah Akin, Julia Hamilton, Alison Verbek, Dr. Ralf Wessel, Dr. Mark Alford, Dr. Jim Schilling, Dr. Wim Dickhoff, Dr. Anders Carlsen, and other members of the department for supporting my Ph.D. application from the beginning and for their support throughout this journey.

Special thanks to Drs. James Miller, Ralf Wessel, Shankar Mukherji, Mark Anastasio, Tamara Hershey, Jonathan Peelle, and Abraham Snyder for accepting to be in my Ph.D. committee and giving me the opportunity to grow and learn in their community.

I also thank the Optical Radiology Lab community and Dr. Samuel Achilefu for creating a warm and welcoming environment for work and for buying a ping pong table for our lab.

I am grateful of all my mentors and lab-mates throughout these years, Dr. Adam Eggebrecht for his mentorship when I joined the lab, Dr. Andrew Fishell for all the jokes and fun times he created in the office and also for always being available to fill in for me in my sick days, Dr. Karla Bergonzi, Dr. Mathew Reisman, Dr. Jonathan Bumstead, and Dr. Patrick Wright for helping me with my very first posters and listening to my practice talks and for answering all my questions from neuroimaging to English, Zachary Markow and Dr. Broc Burke for activating the mathematician inside me and for getting to the bottom of the problems with me, Kalyan Tripathy for being such a kind human being and a great office-mate that would bring hope, smile, and music to our room, Alvin Agato, Rachel Rahn, Lindsey Brier, Dr. Hunter banks, Chen Hao Lin, Dr. Monalisa Munsu, Annie Bice, Seana Gaines, Sean Rafferty, Dana Wilhelm, Louise Burkette, Calamity Svoboda, Martin Ogelvitich, Alexa Svoboda, Mariel Schroeder, Tracy Burns-Yocum, Dr. Jason Torobaugh, Dr. Adam Bauer, Dr. Mikhail Brezin, Dr. Monica Shokeen, Debbie Hesse, Shengxuan Chen, Xiaodan Wang, and all other lab members for their warm presence in the neighboring offices and for their support anytime there was a need. I would also like to thank

Edward Richter for being such a friendly person around, and for always asking me how I feel when there was yet another ban for the Iranians in the U.S. Also thanks to Kiana Shahverdi for all the delicious Persian food and the warmth she shared with me in the past couple of years.

I am thankful for Fatemeh and Mahdi Naghiloo for being my family in St. Louis and treating me as my own family would. Their presence in my life in the past six years was one of the biggest joys. I would also like to thank all my friends and family in the U.S. and back home for continually checking on me and making my life happier by their support.

I am also grateful for having met Louie in my life, for all the fun moments and all the table tennis. Thanks for always reminding me to follow my passions and for teaching me to be more like the physicists I admire. I am also thankful of his sweet family for embracing me with love in the past couple of years.

Last but not least, I would like to thank my family. I am grateful of my mom, who envisioned my dreams with me since childhood and for always believing in me. I am thankful of my dad for being such a light in my life and for supporting me to overcome all the difficulties on my way to get here. I am thankful of my sister for being my first and forever mentor and for always helping me find what makes me happy. This path wouldn't have been possible without all these people's love and support.

Arefeh Sherafati

Washington University in St. Louis

August 2020

Dedicated to my parents Farideh and Ali, and my sister Rayhaneh.

ABSTRACT OF THE DISSERTATION

Separating Signal from Noise in High-Density Diffuse Optical Tomography

by

Arefeh Sherafati

Doctor of Philosophy in Physics

Washington University in St. Louis, 2020

Professor Ralf Wessel, Chair

Professor Joseph Culver, Co-Chair

High-density diffuse optical tomography (HD-DOT) is a relatively new neuroimaging technique that detects the changes in hemoglobin concentrations following neuronal activity through the measurement of near-infrared light intensities. Thus, it has the potential to be a surrogate for functional MRI (fMRI) as a more naturalistic, portable, and cost-effective neuroimaging system. As in other neuroimaging modalities, head motion is the most common source of noise in HD-DOT data that results in spurious effects in the functional brain images. Unlike other neuroimaging modalities, data quality assessment methods are still underdeveloped for HD-DOT. Therefore, developing robust motion detection and motion removal methods in its data processing pipeline is a crucial step for making HD-DOT a reliable neuroimaging modality.

In particular, our lab is interested in using HD-DOT to study the brain function in clinical populations with metal implants that cannot be studied using fMRI due to their contraindications. Two of these populations are patients having movement disorders (Parkinson Disease or essential tremor) with deep brain stimulation (DBS) implants and individuals with cochlear implants (CI). These two groups both receive tremendous benefit from their implants at the statistical level; however, there is significant single subject variability. Our overarching goal is to use HD-DOT to

find the relationships between the neuronal function and the behavioral measures in these populations to optimize the contact location of these implant surgeries. However, one of the challenges in analyzing the data in these subjects, especially in patients with DBS, is their high levels of motion due to tremors when their DBS implant is turned off. This further motivates the importance of the methods presented herein for separating signal from noise in HD-DOT data.

To this end, I will first assess the efficacy of state-of-the-art motion correction methods introduced in the fNIRS literature for HD-DOT. Then, I will present a novel global metric inspired by motion detection methods in fMRI called GVTD (global variance of the temporal derivatives). Our results show that GVTD-based motion detection not only outperforms other comparable motion detection methods in fNIRS, but also outperforms motion detection with accelerometers.

I will then present my work on collecting and processing HD-DOT data for two clinical populations with metal implants in their brain and the preliminary results for these studies.

Our results in PD patients show that HD-DOT can reliably map neuronal activity in this group and replicate previously published results using PET and fMRI. Our results in the CI users provide evidence for the recruitment of the prefrontal cortex in processing speech to compensate for the decreased activity in the temporal cortex. These findings support the theory of cognitive demand increase in effortful listening situations.

In summary, the presented methods for separating signal from noise enable direct comparisons of HD-DOT images with those of fMRI in clinical populations with metal implants and equip this modality to be used as a surrogate for fMRI.

Chapter 1: Introduction

The physics behind imaging the neuronal function through hemodynamic contrasts was first discovered in magnetic resonance imaging (MRI) with the development of the blood oxygen level-dependent (BOLD) signal in 1990 [1, 2]. BOLD signal measures the absolute amount of the deoxyhemoglobin (HbR) concentration in the brain driven by localized changes in the blood flow and oxygenation. These localized blood flow changes are coupled to underlying neuronal activity by a process called neurovascular coupling [3-5].

Functional MRI (fMRI) is the current gold standard neuroimaging technique mainly due to its good spatiotemporal resolution and is widely used in neuroscience and medicine for measuring the neuronal activity underlying different cognitive and behavioral states. However, as applications of functional neuroimaging expand to more clinical and naturalistic settings, fMRI's contraindication with metal implants and its non-portability become more limiting.

Functional near-infrared spectroscopy (fNIRS) is another neuroimaging modality that measures similar hemoglobin contrast changes as fMRI by shining and detecting the safe near-infrared light to the scalp [6]. Although standard fNIRS has been developed around the same time as fMRI, it has been less popular mainly because of its lower spatial resolution and lower depth of sensitivity due to the absorption and scattering of the near-infrared light by the tissue [7]. However, since most cognitive functions in the brain happen on the cortical areas (~2-3 cm deep from the scalp), fNIRS has a lot of potential for neuroimaging in situations that fMRI is either contraindicated or is limiting [8-11].

Standard fNIRS systems are critically hampered by sparse measurement distributions that lead to poor anatomical specificity and unreliable image quality due to the crosstalk with scalp signals [12-14]. They also have poor spatial resolution, limited field of view (FOV) [15], unstable point spread functions (PSF) [15], and uneven spatial coverage [6, 16].

Our lab pioneered an fNIRS-based 3D tomographic brain imaging device called high-density diffuse optical tomography (HD-DOT) [7] that solves these problems by using high-density interlaced source and detector imaging arrays that support densely overlapping measurements and by creating anatomical head models [17-20]. These advances result in higher spatial resolution [15], stable PSFs, and significantly improved isolation of brain signals from scalp signals, compared to the standard fNIRS [15, 21].

This increased spatial resolution opened the door for the use of HD-DOT as a real surrogate in many clinical applications that were not feasible with fMRI, such as studying the brain function in people with deep brain stimulation (DBS) implants or cochlear implants (CI) [22-24].

Other clinical applications of HD-DOT include situations where a continuous bedside monitoring of patients is desirable, such as monitoring patients with acute stroke in intensive care units [25] or monitoring brain-injured infants in neonatal intensive care units (NICU).

Besides these clinical applications, wearable HD-DOT could be the best candidate for understanding the cognitive function of a healthy brain in real-time, in BCI applications, and in studying concepts such as attention, emotion, and learning in more naturalistic and real-life settings than the fMRI magnet.

With all these potentials, a limiting factor for HD-DOT is that its data processing methods are still underdeveloped, and this is one of the reasons that its use has been limited in all these areas.

Since the time our lab has developed the densest HD-DOT imaging system to its date in 2014 with 96 sources of light and 92 detectors [20], a baseline data processing software (NeuroDOT) [7, 26] has been established for this system that includes preliminary preprocessing and image reconstruction steps. However, these methods were not optimized for different imaging scenarios, such as when motion artifacts are present or when a more precise localization of the brain activity is desired.

The design and architecture of new generations of HD-DOT are constantly being optimized in our lab to provide better fMRI-like imaging outputs. However, in addition to device development, an in-depth understanding of the optical signal is crucial for developing suitable image processing methods and data quality control measures from these devices.

The purpose of this thesis is to present a comprehensive assessment of data quality measures for HD-DOT data along with updates to the current data quality processing pipeline to equip this technology for its broader application in the clinic and real-time settings.

I will start the thesis by presenting an overview of the HD-DOT imaging methods and its current data processing pipeline, in chapter 2.

In chapter 3, I will present new methods for analyzing the effects of motion artifacts in HD-DOT data and assess all state-of-the-art motion correction methods introduced in the fNIRS literature for HD-DOT. One important difference between fNIRS and HD-DOT is that fNIRS devices have a limited number of measurements. Thus, motion detection and motion correction are usually done on the single-channel level [27, 28]. In HD-DOT with thousands of measurements, channel by channel signal cleaning is computationally inefficient and does not take into account the impacts of motion across the field of view. Therefore, we developed a novel global motion metric inspired by motion tracking methods in fMRI [29] called GVTD (global variance of the temporal

derivatives). We show that GVTD-based motion detection not only outperforms other common motion detection methods in fNIRS but also outperforms motion detection with accelerometers by using an instructed motion paradigm. We designed GVTD to be used as a motion index for rank-ordering the quality of HD-DOT data in real-time and offline and for predicting the similarity of the resulting HD-DOT images to those of fMRI. We also show that censoring motion artifacts with GVTD outperforms other correction methods proposed in the fNIRS literature by removing the spurious effects of artifacts and increasing the statistical significance of the group results in multiple datasets and imaging paradigms [29].

Motion removal is a very important step in processing data from any imaging modality. For example, many recent fMRI papers have shown that the conclusions of some clinical studies needed to be corrected after newer motion censoring methods were developed, and the spurious effects caused by motion artifacts were removed [30]. Therefore, the presented methods in this thesis are crucial for making HD-DOT's processing pipeline more reliable for its use in broader applications.

Equipped with these data quality assessment methods, I will then present my work on collecting and processing HD-DOT data for two clinical populations with metal implants in their brain and the preliminary results for these studies. In chapter 4, I will review the challenges of the current neuroimaging modalities for imaging people with Parkinson disease (PD) with DBS and the importance of neuroimaging tools like HD-DOT. This population was selected for this thesis because PD is a neurological movement disorder, and these patients have high levels of tremor, especially during their DBS off condition. Therefore, without data quality assessment methods presented in this thesis, processing their HD-DOT data would not have been possible. With a dataset of 15 PD patients with DBS and 15 controls and adopting the data quality assessment

methods proposed in chapter 3, we could replicate the results obtained for neuroimaging of PD patients without DBS using fMRI [31]. We could also present the very first high-quality fMRI-like functional connectivity neuroimaging results in the same group of PD patients with their DBS on [24]. The results in this chapter were possible by the new advances in the HD-DOT software for motion removal in this high-motion population.

In chapter 5, I will apply the denoising methods presented in chapter 3, for studying the cortical language networks in listeners with cochlear implants (CIs), another clinical population that cannot be studied with fMRI due to their contraindications. Cochlear implants compensate for the dysfunction in the cochlea by stimulating the auditory nerve and enabling their users to perceive sounds [32, 33]. However, due to the crosstalk between the CI electrodes, there is a lack of spatial selectivity in the internal representation of the sound frequency content [34, 35]. This distortion of the sound contributes to the tremendous variability in how well listeners with CIs understand the spoken speech [36, 37]. Our preliminary results in a group of 18 controls and 18 CI users provide evidence for the functional brain differences in this population and how these people recruit parts of their prefrontal cortex to compensate for their effortful listening with a lower sound quality.

In conclusion, the chapters in this dissertation provide a comprehensive guideline for evaluating data quality in HD-DOT (including motion detection and motion censoring) and the software needed for applying these measures. These methods help to make HD-DOT a more reliable imaging technique for imaging populations with brain implants and with high-motion levels.

Chapter 2: Data Processing Methods for High-Density Diffuse Optical Tomography

2.1 Basic ideas behind functional near-infrared imaging

HD-DOT, similar to near-infrared spectroscopy (NIRS), takes advantage of two key ideas related to the interaction of the near-infrared light with the tissue. First, there is a window in the frequency spectrum of the near-infrared light (650 to 1350 nm) called *optical window* that the dominant light-tissue interaction is scattering, and the light has its maximum depth of penetration [38]. This phenomenon occurs since most parts of the tissue are transparent to the near-infrared light in this optical window, and the main source of attenuation is absorption by blood at short wavelengths and by water at long wavelengths. Blood as the main absorber of the near-infrared light in shorter wavelengths consists of oxyhemoglobin (HbO_2) and deoxyhemoglobin (HbR) molecules that exhibit different absorption spectra commonly represented by molar extinction coefficients (Figure 2.1) [39, 40]. The peaks of absorption of the near-infrared light for HbO_2 and HbR are different (420 nm for HbO_2 and 850 nm for HbR), and there is a point where the molar extinction coefficient spectra of these two molecules are equal (isosbestic point).

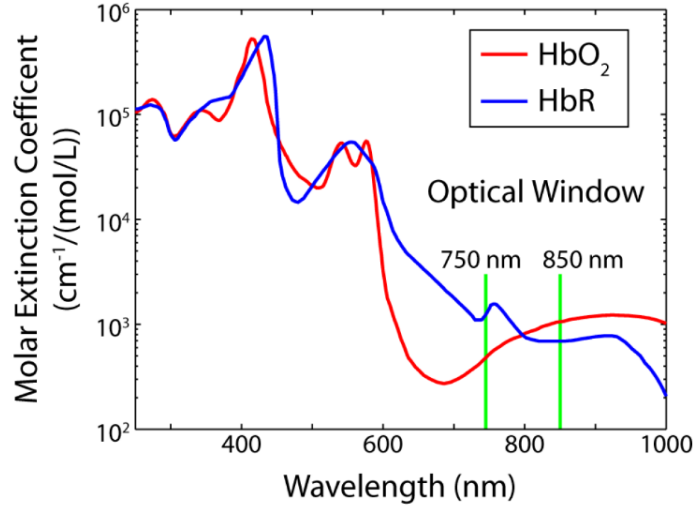


Figure 2.1 Hemoglobin absorption spectra. The divergent extinction coefficients of oxy- and deoxyhemoglobin in the optical window (650 to 1350 nm) and their peaks around the isosbestic point enable near-infrared spectroscopy.

The second key idea for NIRS is that by using two different wavelengths of near-infrared light, one below and one above the isosbestic point (normally 750 nm and 850 nm), we will have two equations for calculating the concentration changes of HbO_2 and HbR as shown in the following equations [7]:

$$\mu_{a, 750} = \epsilon_{HbO_2, 750} [HbO_2] + \epsilon_{HbR, 750} [HbR] \quad (2.1)$$

$$\mu_{a, 850} = \epsilon_{HbO_2, 850} [HbO_2] + \epsilon_{HbR, 850} [HbR] \quad (2.2)$$

In this equation, μ_a is the absorption coefficient; ϵ is the extinction coefficient.

Writing these two equations in the matrix form leads to a single equation that is the key idea behind all near-infrared-based imaging techniques:

$$\begin{bmatrix} \mu_{a, 750} \\ \mu_{a, 850} \end{bmatrix} = \begin{bmatrix} \epsilon_{HbO_2, 750} & \epsilon_{HbR, 750} \\ \epsilon_{HbO_2, 850} & \epsilon_{HbR, 850} \end{bmatrix} \begin{bmatrix} [HbO_2] \\ [HbR] \end{bmatrix} \quad (2.3)$$

Which can be simplified to:

$$x_{\mu_a} = E x_{Hb} \quad (2.4)$$

Therefore, we can calculate the changes in the HbO₂ and HbR concentrations by inverting the extinction coefficient matrix, E, and have:

$$x_{Hb} = E^{-1} x_{\mu_a} \quad (2.5)$$

This calculation shows that similar to the BOLD signal in fMRI, near-infrared spectroscopy can enable functional brain imaging using the changes in HbO₂ and HbR based on the local changes in the absorption of near-infrared light at two selected wavelengths. It is also common in NIRS to combine these two images and define a new image, HbT = HbO₂ + HbR, called total hemoglobin change. However, the important point is that following each neuronal activity, we always expect to see an increase in HbO₂ and a decrease in HbR concentrations. Since the increase in HbO₂ is normally greater than the decrease in HbR, there is also an overall increase in HbT signal. These changes in the oxy- and deoxyhemoglobin following the neuronal activity are commonly known as the hemodynamic response function (an example is shown in Figure 2.2 from [21]).

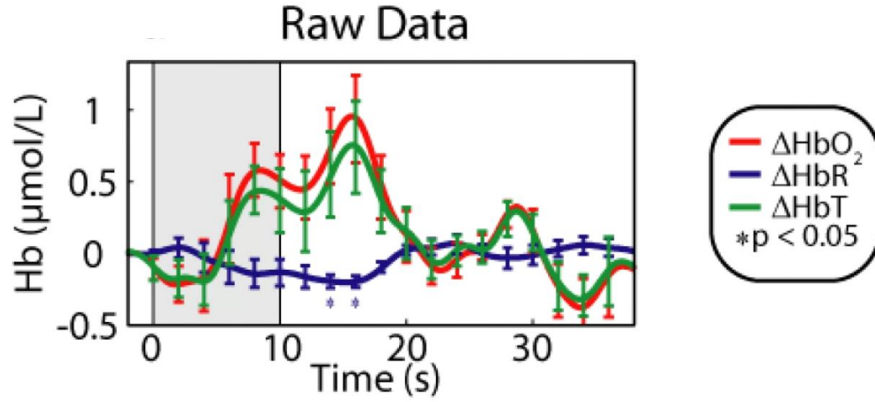


Figure 2.2 Oxy, deoxy, and total hemoglobin response functions. Time-traces of the hemodynamic response to six blocks of a visual stimulus with HbO_2 in red, HbR in blue, and HbT in green mapped using DOT. Greg et al. 2010.

In the next two sections (§2.2 and §2.3), I will review two common models for calculating the changes in the absorption of the HbO_2 and HbR using near-infrared light intensity measurements.

2.2 Modified Beer-Lambert law

In most near-infrared-based imaging techniques, the near-infrared light is shined to the head using a group of sources, and the attenuated light is collected through a group of detectors. The shined light gets absorbed and scattered in the tissue. A simple empirical method to model the propagation of the near-infrared light in the tissue is proposed by Cope et al., and is called the modified Beer-Lambert Law (MBLL) [41]. MBLL describes the relationship between the changes in the absorption coefficient (μ_a) of an absorbing and scattering medium and the changes in the optical density (OD). With optical density defined as the negative log-ratio of the intensity of the collected light (I) with respect to the intensity of the incident light (I_0) [39]. The key difference between MBLL and the traditional BLL is that the former takes into account the increased path-length of

light through a highly scattering sample like the tissue by adding a differential path-length factor (D_{PF}):

$$\Delta OD = -\log \frac{I}{I_0} = L D_{PF} \Delta \mu_a \quad (2.6)$$

Where ΔOD is the changes in the optical density, L is the distance traveled by light from the source to the detector, and $\Delta \mu_a$ is the changes in the absorption coefficient [39].

In NIRS, it is common to convert the collected light-level intensities (I) to the optical density changes using Eq. 2.6. However, since the MBLL assumes that the absorption changes are evenly distributed over the photon's path, there is no ability to distinguish between the changes that happen at different locations along the measurement path. Therefore, a more accurate model can describe the propagation of the light in the tissue using a differential model of the light flow [7].

2.3 Forward model for the diffusion of near-infrared light

The path of the photons in the tissue is following a random walk from one scattering event to the next (Figure 2.3 [42]). This chain of scattering events in the tissue is called diffusion. Therefore, the flow of the near-infrared light can be modeled by the diffuse approximation to the radiative transfer equation (RTE) [43] as follows:

$$D \nabla^2 \Phi(r) - v \mu_a(r) \Phi(r) = -v S(r) \quad (2.7)$$

In this equation, Φ is the photon fluence (light intensity), v is the speed of light in the medium, S is a source distribution, and D is the diffusion coefficient defined as:

$$D = \frac{v}{3(\mu'_s + \mu_a)} \quad (2.8)$$

Where μ_a is the absorption coefficient, μ'_s is the *reduced* scattering coefficient that is correlated to μ_s , the scattering coefficient, by the scattering anisotropy factor g :

$$\mu'_s = (1 - g) \mu_s \quad (2.9)$$

This correction of the scattering coefficient results in a longer effective scattering mean free path due to the biased forward scattering of tissue (in biological tissue, g is approximately 0.9; so, a photon can be considered isotropically scattered after 10 scattering events) [7].

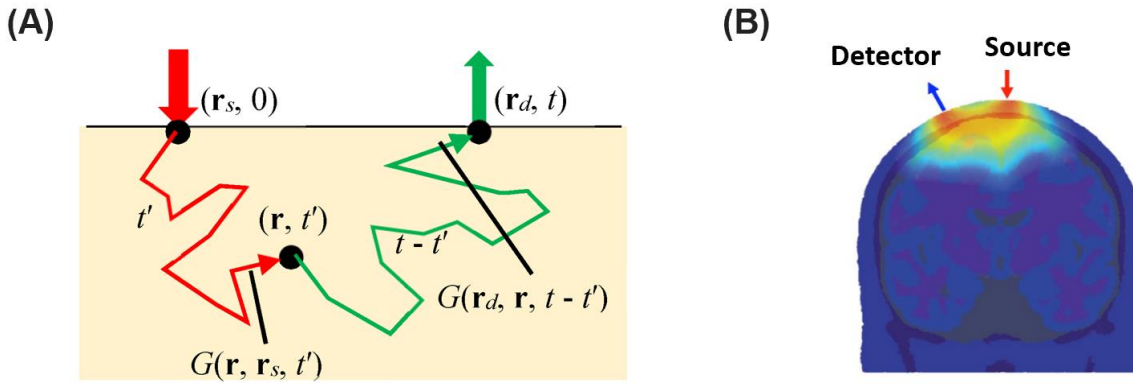


Figure 2.3 Near-infrared light diffusion. (A) Light propagation (random walk) from the source position, \mathbf{r}_s , to the detector position, \mathbf{r}_d , through an arbitrary position, \mathbf{r} . Yamada et al., 2019. (B) The distribution of detected photon paths through an anatomical head model for one source and one detector location. Credit: Gowerlabs.

This differential Eq. 2.7 can be solved using approximation models. Here, by defining the effective Green's functions for modeling the source-detector geometries:

$$\tilde{G}_s(\mathbf{r}_v) = \int G(\mathbf{r}_s, \mathbf{r}_v) S(\mathbf{r}_s) d\mathbf{r}_s \quad (2.10)$$

$$\tilde{G}_d(\mathbf{r}_v) = \int G(\mathbf{r}_v, \mathbf{r}_d) S(\mathbf{r}_d) d\mathbf{r}_d \quad (2.11)$$

$$\tilde{G}_{sd} \equiv - \int \int G(\mathbf{r}_s, \mathbf{r}_d) S(\mathbf{r}_s) D(\mathbf{r}_d) d\mathbf{r}_s d\mathbf{r}_d \quad (2.12)$$

and using Born and Rytov approximations, we can find an approximation solution for the original differential RTE as follows (the derivation steps can be found in [7]):

$$-\ln\left(\frac{\Phi}{\Phi_0}\right) = \frac{\nu}{D} \int \frac{\tilde{G}_s(\mathbf{r}_v) \tilde{G}_d(\mathbf{r}_v)}{\tilde{G}_{sd}} \Delta\mu_a(\mathbf{r}_v) d\mathbf{r}_v \quad (2.13)$$

However, our goal is to discretize this integral equation and assign an absorption change value to each brain voxel from the light-level measurements. Therefore, we can convert the integral to a summation over voxels as follows:

$$-\ln\left(\frac{\Phi}{\Phi_0}\right) = \frac{\nu V_{vox}}{D} \sum_{j \in voxels} \frac{\tilde{G}_s(\mathbf{r}_j) \tilde{G}_d(\mathbf{r}_j)}{\tilde{G}_{sd}} \Delta\mu_a(\mathbf{r}_j) \quad (2.14)$$

In this equation, V_{vox} is the volume of a voxel. This solution can be written in the following matrix format:

$$\begin{bmatrix} y_1 \\ \vdots \\ y_M \end{bmatrix} = \frac{-\nu V_{vox}}{D} \begin{bmatrix} A_{1,1} & \cdots & A_{1,N} \\ \vdots & \ddots & \vdots \\ A_{M,1} & \cdots & A_{M,N} \end{bmatrix} \begin{bmatrix} \Delta\mu_a(r_1) \\ \vdots \\ \Delta\mu_a(r_N) \end{bmatrix} \quad (2.15)$$

M is the number of measurements and N is the number of voxels, and $A_{i,j}$ is defined based on the Green's functions defined in 2.9, 2.10, and 2.11 as follows:

$$A_{i,j} = \frac{\tilde{G}_{s_i}(\mathbf{r}_j) \tilde{G}_{d_i}(\mathbf{r}_j)}{\tilde{G}_{s_i d_i}} \quad (2.16)$$

The whole coefficient term in 2.15 is usually defined as the sensitivity matrix (or A-matrix) as follows, which characterizes the light propagation model:

$$A = \frac{-\nu V_{vox}}{D} \begin{bmatrix} A_{1,1} & \cdots & A_{1,N} \\ \vdots & \ddots & \vdots \\ A_{M,1} & \cdots & A_{M,N} \end{bmatrix} \quad (2.17)$$

Defining the A-matrix simplifies Eq. 2.15 to a simple linear formula for the forward model:

$$y = Ax \quad (2.18)$$

Where x is the vector of absorption changes. This equation indicates that for a given set of near-infrared absorption changes, x [$N \times 1$], and a light propagation model, A [$M \times N$], we can calculate the expected changes in the light intensity measurements, y [$M \times 1$]. M is the number of measurements, and N is the number of voxels.

2.4 Inverse problem

The goal in DOT is to find the voxel-wise absorption changes from the light intensity measurements. Therefore, the forward problem in 2.18 reduces to an inverse problem that solves the values of absorption changes for each voxel from the changes in the light-level measurements:

$$x = A^{-1}y \quad (2.19)$$

However, since the number of measurements, M , and the number of voxels, N , are not equal, matrix A [$M \times N$] is not a square matrix, and thus, it is not invertible. Therefore, we should construct a pseudo-inverse:

$$x = \hat{A}^\# y \quad (2.20)$$

where

$$\hat{A}^\# = (A^T A)^{-1} A^T \quad (2.21)$$

since $A^T A$ is square, it can be inverted, and our inverse problem is solved [7].

2.5 HD-DOT data processing pipeline

HD-DOT's data processing shares common steps with both fNIRS and fMRI. In a standard fNIRS data processing pipeline, the collected light-levels from the source-detectors are being preprocessed by conversion to optical density changes, and then signal denoising and filtering steps are done. Then the denoised optical density signal is converted to the changes in the absorptions of the two shined wavelengths following the MBLL (Eq. 2.6), and then to ΔHbO_2 and ΔHbR through spectroscopy (Eq. 2.5). In DOT, the forward model of the light flow (Eq. 2.18) is used, which is equivalent to the MBLL in fNIRS, but DOT data processing also includes calculation of the sensitivity matrix that maps the measurements to the voxels. The goal in DOT is to solve for the voxelated images of ΔHbO_2 and ΔHbR using Eq. 2.20. This step in DOT is called image reconstruction and is explained in §2.5.7. This voxelated image can then be resampled to the desired anatomical image (subject's anatomical data or an anatomical atlas). These last two steps (image reconstruction and resampling) make DOT images similar to fMRI images. Figure 2.4 [44] demonstrates all data processing steps that we use for our HD-DOT systems. Details of all processing steps are explained in the following sections.

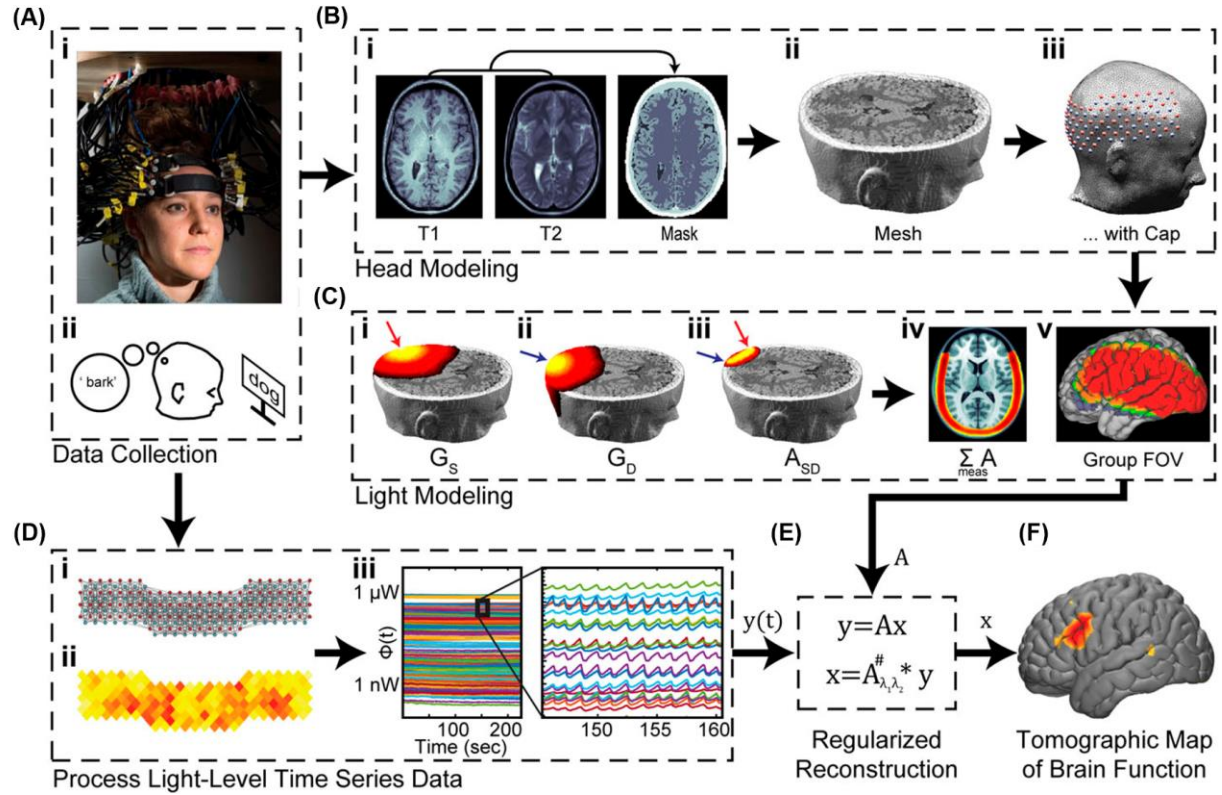


Figure 2.4 HD-DOT data processing overview. (A) Data collection involves (i) locating the source and detector positions on the head and (ii) recording light levels from the head of a participant. In this example, a stimulus paradigm involves the participant generating novel verbs in response to nouns presented on a monitor. (B) A head model for a given participant is created by (i) generating a subject-specific or atlas-based volumetric segmentation of the head tissue, (ii) building a high-density mesh, and (iii) placing the sources and detectors on the head mesh surface. (C) Using the head model, the sensitivity profile for (i) each source (G_s), and (ii) each detector (G_d) are calculated and (iii) combined into a sensitivity profile for each source-detector measurement pair A_{SD} . (iv) The full system sensitivity ΣA can be visualized by summing the sensitivity of each measurement pair. (v) The modeled sensitivity can then be spatially registered to an atlas space for group-level analyses. (D) Separately, the collected light-level data are assessed for (i) noise and (ii) signal level quality, (iii) with high-quality optical data clearly showing a pulse waveform. (E) After preprocessing, the optical data are combined with a regularized inverse of the sensitivity model to generate (F) anatomically-registered maps of cerebral hemodynamics reflecting brain function. Adapted with permission from Eggebrecht et al., Nat. Photonics 8, 448–454 (2014). Copyright 2014 Springer Nature Publishing.

2.5.1 Log-mean of light-levels

First, raw source-detector pair measurements are converted to the optical density changes (ΔOD) by calculating the log-mean ratio of light-levels following the modified Beer-Lambert law (Eq. 2.6):

$$\Delta OD = -\log \frac{I}{I_0} \quad (2.22)$$

Where I is the intensity of the detected light and I_0 is the intensity of the incident light. Note that in NIRS-based techniques, we can only calculate the *changes* in the optical densities (ΔOD) and, following that, the *changes* in HbO₂ and HbR concentrations (ΔHbO_2 , ΔHbR). However, in fMRI, the *absolute* value of the HbR concentration is obtained. Therefore, direct cross-modality comparisons between HD-DOT and fMRI are only possible via comparisons of ΔHbR .

2.5.2 Noisy channel detection

Noisy source-detector channels are empirically defined as those with greater than 7.5% temporal standard deviation [45] and are excluded from further processing. This early pruning of the channels guarantees that noisy channels are not included in further processing. A common reason for these noisy measurements is a poor optode-scalp coupling for an area of the cap due to hair or a mismatch between the HD-DOT cap model (circumference or width) and the head size. Using the NeuroDOT toolbox, we can visualize these noisy channels by circles around the channels in the flat view of the HD-DOT cap for further inspection (Figure 2.5) [26, 29].

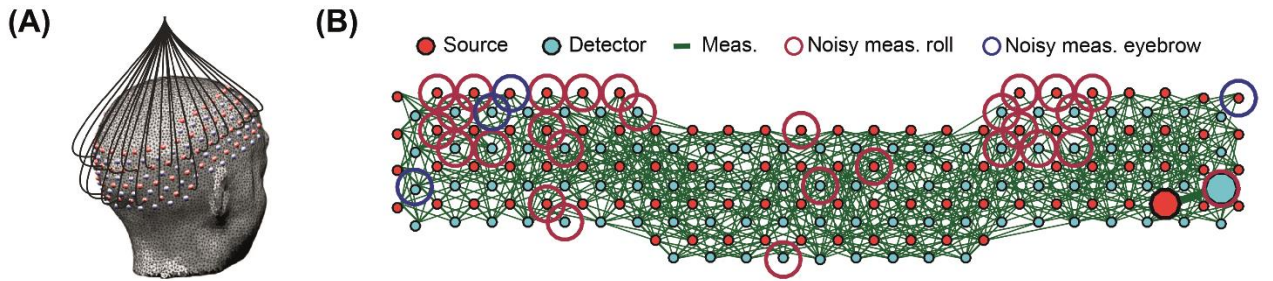


Figure 2.5 Noisy channel detection. (A) Adult HD-DOT cap structure illustrating a subset of optical fibers. (B) Flat view of the cap. Green lines indicate source-detector pairs that have a standard deviation of less than 7.5%. Source or detector locations with greater than 7.5% standard deviation are identified as noisy for roll (large red circles) and eyebrow (large blue circles) motion, respectively.

2.5.3 Bandpass filtering

An important step in any NIRS data processing pipeline is filtering the ΔOD signal to a narrower frequency band. The reason behind this step is that the collected light-levels contain a range of frequencies that are not in the range of brain activity, such as low-frequency drifts (< 0.003 Hz) in long data runs, respiration (~ 0.25 Hz), heartbeat (~ 1 Hz), and other high-frequency contents (> 0.5 Hz) due to noise (systemic or motion artifacts). On the other hand, based on many studies, we now know that the hemodynamic changes in the brain in response to different task stimuli are in the range of 0.02 Hz to 0.5 Hz, and resting state fluctuations are in the range of 0.009 Hz to 0.08 Hz. Therefore, at this step of the HD-DOT data processing, we perform a bandpass filtering depending on the type of data (0.02 – 1 Hz for tasks and 0.009 – 1 Hz for rest) to limit our signal to around the frequency of the physiological signal. The reason that we do not filter the data to lower than 1 Hz at this step is to first estimate the superficial signal (containing respiratory and heartbeat frequencies).

2.5.4 Superficial signal regression

HD-DOT enables a unique denoising step called superficial signal regression (SSR) or global signal regression (GSR). The idea behind SSR is that the high-density grid of the HD-DOT system provides measurements with multiple source-detector separations; 1st- through 4th-nearest neighbors (abbreviated as nn1, nn2, nn3, nn4) with source-detector distances of 13 mm, 30 mm, 39 mm, and 47 mm, respectively (Figure 2.6A). Most functional brain activities are obtained via nn2, nn3, and longer separations because these measurements go deep enough to contain physiological brain information. First-nearest neighbors, on the other hand, are sensitive mostly to the scalp and skull, and thus do not contain any physiological content. However, they contain all other frequencies that we do not care about (respiratory, heartbeat, noise). Therefore, we can leverage this fact and estimate this global signal by averaging over all nn1 measurements. This

global signal estimate can then be regressed from all measurements [21]. Figure 2.6B shows how SSR can lead to only the frequencies that are due to the changes in the physiological signal [7, 21].

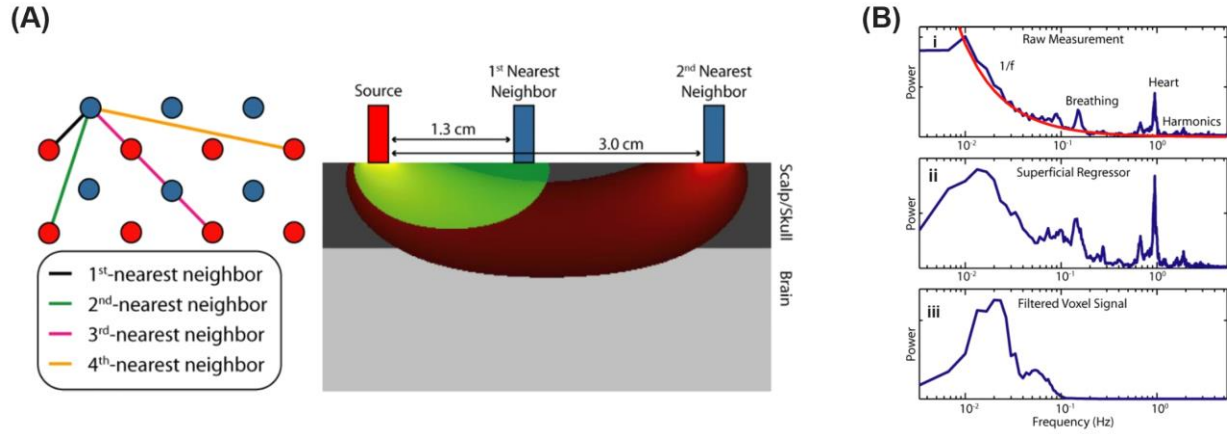


Figure 2.6 Superficial signal regression. (A) Definitions of nearest neighbor measurements and slices through a semi-infinite simulation of photon flow for 1st- and 2nd-nearest neighbor separation. We see that 1st-nearest neighbors are sensitive mostly to scalp and skull, while 2nd-nearest neighbors sample into the brain, Greg et al., 2010. (B) Power spectra of resting-state DOT signals (i) Spectral power of a single 2nd-nearest-neighbor resting-state time trace, sampling both brain and superficial tissues, before the application of any filters. The low-frequency components follow a $1/f$ curve (red), and there are peaks at the respiratory (0.16 Hz) and cardiac rates (0.95 Hz). (ii) Spectral power of the superficial regressor derived from all 1st-nearest-neighbor measurements in the visual pad. These systemic low-frequency fluctuations are removed from the data prior to performing functional connectivity mapping. (iii) Spectral power of a filtered imaged signal (5 min from a single voxel under the measurement in (i)). This remaining spectral power within the desired frequency range is used to perform fcDOT. All traces have been smoothed with a moving average filter, width five voxels. White 2010.

2.5.5 Secondary low-pass filtering and resampling

After data were bandpass filtered, and the superficial signal is estimated and regressed, at this step, we perform the final low-pass filtering and narrow the frequency of our signal to the expected physiological activity frequency. For task-based data, we use the 0.5 Hz cut-off to remove the cardiac oscillations [28, 46-48]. For resting state data, a low-pass filter of 0.08 Hz is performed to remove the cardiac oscillations and to narrow the signal to the spontaneous, low-frequency fluctuations following the previous recommendations for functional connectivity analysis [49-52]. Task data provides two advantages over the resting state. First, the task design can impart high

amplitude and high-frequency dynamics beyond what would normally be found in the resting state. Second, the block averaging of the tasks provides an approach to lower the noise and physiological clutter in the data. So while resting state uses the common infra-slow band (0.009-0.08 Hz) of the vast majority of the functional connectivity MRI literature [49-52], the task preprocessing uses a higher filter band (0.02 to 0.5 Hz) to avoid 1/f noise [28, 46-48]. Following this low-pass filtering, the time-courses were then down-sampled from 10 Hz to 1 Hz and then passed for image reconstruction [29].

Most fNIRS data processing pipelines end here by calculating an estimate of $\Delta\mu_a$ using the MBL (Eq. 2.6) and following that estimating ΔHbO_2 , ΔHbR using the spectroscopy methods explained in Eq. 2.5. However, most DOT processing pipelines estimate the $\Delta\mu_a$ by solving the inverse problem explained in Eq. 2.20. This inverse problem step is not common in fNIRS, due to the sparsity of the measurements, lower spatial resolution, and low depth of profile [7].

2.5.6 Light modeling

After performing the preprocessing steps, measurements are ready for image reconstruction by solving the inverse problem ($x = \hat{A}^\#y$, Eq. 2.20). However, an important step is to calculate the sensitivity matrix (A-matrix, Eq. 2.17). A-matrix is an $M \times N$ matrix (M is the number of measurements, and N is the number of voxels) that models the light-paths (from the measurement space) to the brain (voxel space). This simulation is done either using an anatomical atlas head model (average structural MRI images across many people) or a subject-specific head model using an MRI T1, MRI T2*, or CT image. The steps of the anatomical light modeling are as follows: **1.** Anatomical MRI data (either atlas T1 image, subject-specific T1 or T2*, or atlas T1 transformed to the subject CT space) are used to segment the head to five putative tissue regions (scalp, skull, gray matter, white matter, CSF). **2.** This initial segmentation (that includes scalp and skull regions)

is then combined with another high-quality brain segmentation of the same anatomical data obtained with the Freesurfer software. **3.** The optical properties of these five segments are then assigned based on the common values in the literature (Tabel 2.1, [45, 53]). **4.** A high-quality tetrahedral mesh with an average internode distance of 1.5 mm is then generated from the segmented volume using the NIRVIEW software [54]. **5.** The grid of the source-detector positions for the finite element model (FEM) is then placed on the head following the spring relaxation approach [19, 55]. **6.** A finite-element solution to the diffusion approximation of the RTE within the anatomical space of the data was generated using the NIRFAST software [56]. This solution of the sensitivity matrix relates the light-level changes at the scalp surface to the hemoglobin absorption changes at nodes throughout the volume. The A-matrix is then resampled and interpolated to an isotropic voxel space [20].

Table 2.1 Optical properties of segmented head tissue. Eggebrecht et al., 2012.

	750 nm		850 nm		Index of refraction
	μ_a [mm ⁻¹]	μ_s [mm ⁻¹]	μ_a [mm ⁻¹]	μ_s [mm ⁻¹]	n
Scalp [*]	0.0170	0.74	0.0190	0.64	1.4
Skull [*]	0.0116	0.94	0.0139	0.84	1.4
CSF ^{**}	0.004	0.3	0.004	0.3	1.4
Gray matter ^{***}	0.0180	0.8359	0.0192	0.6726	1.4
White matter ^{***}	0.0167	1.1908	0.0208	1.0107	1.4

^{*} Strangman et al., 2002.

^{**} Custo et al., 2006.

^{***} Bevilacqua et al., 1999.

2.5.7 Image reconstruction

At this step, we completed the signal processing in the measurement space (y) and also created the sensitivity matrix (A-matrix). We are now ready to solve the inverse problem $x = \hat{A}^\# y$. For this

step, we can calculate the pseudo-inverse of the A-matrix ($\hat{A}^\#$ as described in §2.20) by performing the Tikhonov regularization:

$$A^\# = [A^T A + \lambda_1 \max \{diag(S)\} I]^{-1} A^T \quad (2.23)$$

Where S is the singular value decomposition (SVD) of A , I is the identity matrix, λ_1 is the regularization parameter, $\{diag(S)\}$ is a normalization term so that λ_1 can be set independent of the absolute values in A [7].

$A^T A$ is a square matrix ($N \times N = [N \times M] \times [M \times N]$), where N is the number of voxels, M number of measurements, where M is always much smaller than N). Therefore, this equation can be re-written as follows for efficiency (AA^T is an $M \times M$ square matrix) [7]:

$$A^\# = A^T [AA^T + \lambda_1 \max \{diag(S)\} I]^{-1} \quad (2.24)$$

The second regularization term needed here is to correct for an artificially shallow image reconstruction due to the exponential attenuation of light. One way to correct for this artifact is to add a spatially variant regularization term to normalize the sensitivity within each voxel [7].

$$diag(L) = \sqrt{diag(A^T A) + \lambda_2 \max \{diag(A^T A)\}} \quad (2.25)$$

Which results in a new inversion problem using the spatially normalized A-matrix, $\tilde{A} = L^{-1}A$.

Therefore, Eq. 24 can be re-written as:

$$\tilde{A}^\# = \tilde{A}^T [\tilde{A} \tilde{A}^T + \lambda_1 \max \{diag(S')\} I]^{-1} \quad (2.26)$$

Where S' is the SVD of \tilde{A} . After the pseudo-inverse matrix $\tilde{A}^\#$ is calculated, the spatial regularization can be inverted $\hat{A}^\# = \tilde{A}^\# L^{-1}$. Therefore, the final reconstruction equation will be:

$$x = \hat{A}^\# y \quad (2.27)$$

In the current data processing pipeline for HD-DOT, the empirical values of $\lambda_1 = 0.01$ and $\lambda_2 = 0.1$ are chosen.

2.5.8 Spectroscopy

The image reconstruction solution in Eq. 2.27 can be calculated for both 750 and 850 nm light-level signals:

$$x_{\mu_a, 750} = \hat{A}^\# y_{750} \quad (2.28)$$

$$x_{\mu_a, 850} = \hat{A}^\# y_{850} \quad (2.29)$$

Then, by plugging in the extinction coefficient values for $\epsilon_{HbO_2, 750}$, $\epsilon_{HbR, 750}$, $\epsilon_{HbO_2, 850}$, $\epsilon_{HbR, 850}$ from the literature (Table 2.2 [57]) in Eq. 2.5 ($x_{Hb} = E^{-1}x_{\mu_a}$), we can find the corresponding values for x_{Hb} (HbO_2 , HbR).

Table 2.2 Extinction coefficients of HbO₂ and HbR for 750 nm and 850 nm light. Wray et al. 1988.

ϵ (1/mM \times 1/cm)	750 nm	850 nm
HbO ₂	0.5	1.1
HbR	1.6	0.8

This step concludes the imaging problem and the standard data processing pipeline for HD-DOT. The following two steps, spatial resampling, and spatial smoothing are common steps in fMRI imaging and thus can easily be performed on HD-DOT images after the image reconstruction step.

2.5.9 Spatial resampling

Spatial resampling or spatial normalization is transforming an image from one space into a target space using an affine (or other types of) transformation. It is common practice in neuroimaging to transform the voxelated images from the native subject space into a standard brain atlas space (MNI, Talairach, etc.). This step is helpful, especially when an average image over multiple subjects is desired. A key point regarding transforming the images is to keep track of their *coordinate space*. Most neuroimaging image formats (e.g., 4dfp, nifti) keep track of two pieces of information regarding the coordinate space of an image by defining parameters such as *center* and *mmpix* (mm per pixel (or mm per voxel)). *Center* determines the origin of the image, and *mmpix* reveals the resolution of the voxels (e.g., 1mm, 2mm, etc.). The coordinate space of a reconstructed image is determined by the type of anatomical data used for making the sensitivity matrix (A-matrix). If the A-matrix was computed using the MNI T1 image, the reconstructed images will be in the MNI coordinate space. However, if the A-matrix was computed using either subject's MRI or a transformation of MNI T1 to the subject's CT image, the reconstructed images will be in the space of the subject anatomical MRI or CT data. Therefore, in the process of spatial resampling of an image, the values of the *center* and *mmpix* parameters will be updated to their values in the target image.

2.5.10 Spatial smoothing

Spatial smoothing is also a common step in fMRI image visualization. Smoothing blurs the sharp edges in an image and pronounces spatial correlations. The most important advantage of this process is that the neighboring patterns of activity will be averaged together, and the spatial patterns become more visible. However, the disadvantage of this process is losing spatial resolution.

Mathematically, smoothing is performed by convolving the image with a smoothing kernel. The most common type of kernel for smoothing neuroimages is Gaussian (Eq. 2.30):

$$G(x) = \frac{1}{\sqrt{2\pi}\sigma} e^{-\frac{x^2}{2\sigma^2}} \quad (2.30)$$

Where x is the distance from the origin, and σ is the standard deviation of the Gaussian kernel.

Since the Fourier transform of a Gaussian is another Gaussian, thus, applying a Gaussian blur is equivalent to reducing higher frequencies from the image (similar to low-pass filtering). When applying a Gaussian blur (with a certain standard deviation σ) to an image, we can calculate the final resolution of the image based on the full width at half maximum (FWHM) of the Gaussian function as follows:

$$\begin{aligned} \frac{1}{2\sqrt{2\pi}\sigma} &= \frac{1}{\sqrt{2\pi}\sigma} e^{-\frac{x^2}{2\sigma^2}} \\ \frac{1}{2} &= e^{-\frac{x^2}{2\sigma^2}} \\ -\ln(2) &= -\frac{x^2}{2\sigma^2} \\ 2\ln(2)\sigma^2 &= x^2 \\ HWHM = x &= \sqrt{2\ln(2)}\sigma \\ FWHM = 2x &= 2\sqrt{2\ln(2)}\sigma = 2.355\sigma \\ \sigma &= \frac{FWHM}{2\sqrt{2\ln(2)}} \end{aligned} \quad (2.31)$$

Where $HWHM$ is half-width half maximum, and $FWHM$ is full width half maximum.

It is also common to use the smoothing parameters of the Fourier transform of the Gaussian as follows:

$$F(G(x)) = \sigma \sqrt{2\pi} e^{-2\sigma^2 \pi^2 k^2} \quad (2.32)$$

Where k is the frequency.

For finding the relationship between k and σ at FWHM, we need to set the $F(G(x))$ as half of its maximum value:

$$\frac{1}{2} \sigma \sqrt{2\pi} = \sigma \sqrt{2\pi} e^{-2\sigma^2 \pi^2 k^2} \quad (2.33)$$

Therefore, we will have:

$$k = \frac{\sqrt{\ln(2)}}{\sqrt{2} \pi \sigma} \quad (2.34)$$

On the other hand, using Eq. 2.31 we can find the relationship between the frequency and the *FWHM*:

$$k = \frac{2\sqrt{\ln(2)}}{\pi FWHM} = \frac{0.4413}{FWHM} \quad (2.35)$$

2.6 Conclusion

In this chapter, I presented a review of the physics behind near-infrared spectroscopy (NIRS) and high-density diffuse optical tomography (HD-DOT), as well as the data processing stream of HD-DOT used in the NeuroDOT MATLAB toolbox [26]. All the data processing steps explained in §2.5 of this chapter are summarized in Figure 2.7 [20]. An important missing step in the current HD-DOT pipeline is data quality assessment steps, including motion artifact detection and removal, which is the topic of the next chapter.

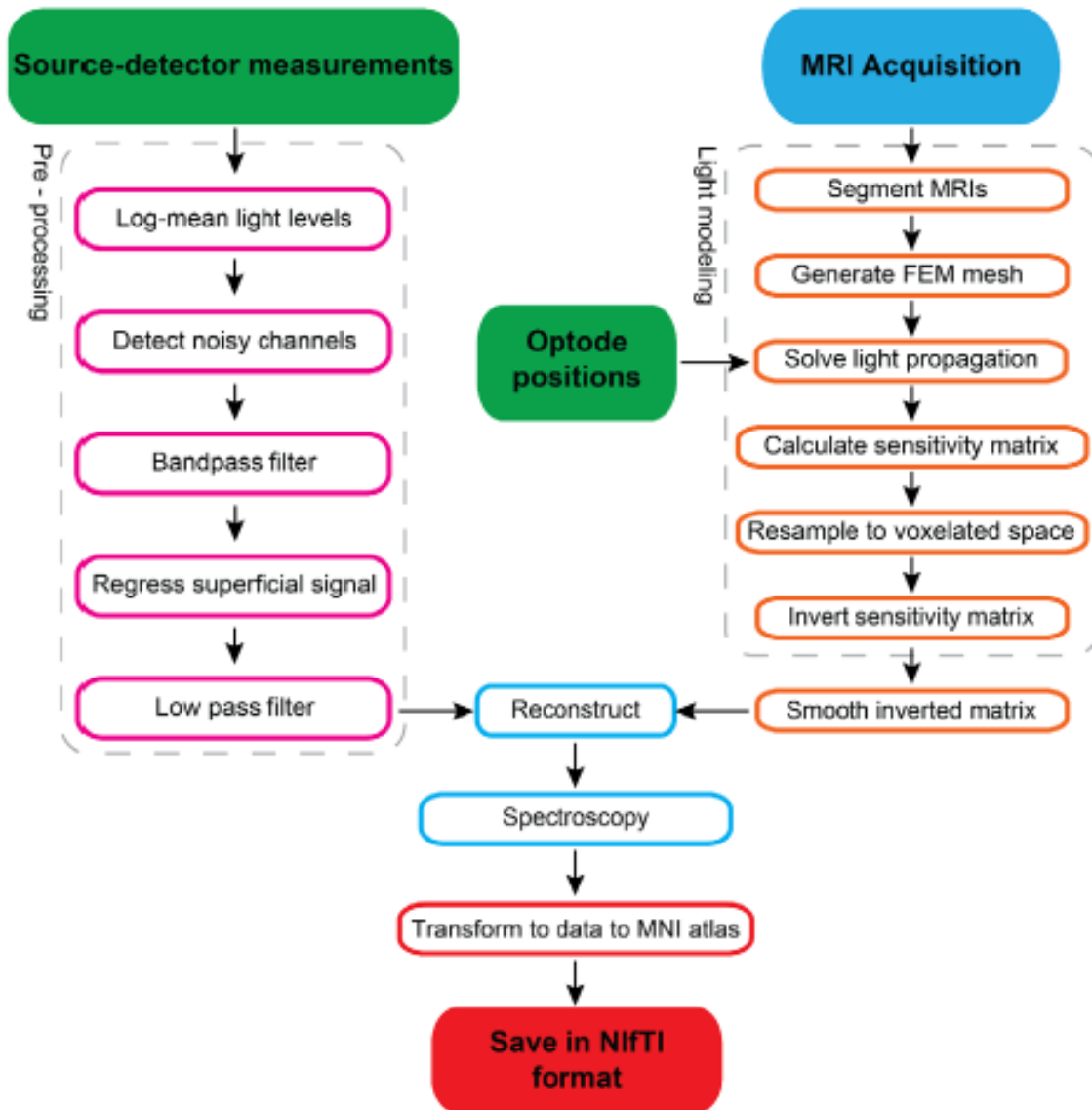


Figure 2.7 HD-DOT data processing pipeline. Pre-processing steps are shown in pink, light modeling steps in orange, image reconstruction steps in blue, spatial transformation in red. Eggebrecht et al., 2014.

Chapter 3: Global Motion Detection and Censoring in High-Density Diffuse Optical Tomography¹

3.1 Introduction

High-density diffuse optical tomography (HD-DOT) has tremendous potential to be a surrogate for functional magnetic resonance imaging (fMRI) [22, 23, 49, 50, 58, 59]. However, methods for dealing with detection and suppression of motion artifacts in HD-DOT data are relatively underdeveloped, which limits its application to many important clinical populations. While fMRI has become a gold standard for cognitive neuroimaging, it is contraindicated in subjects with metal implants and cannot be used in many clinical settings, and studies seeking more naturalistic imaging environments. In contrast, fNIRS-based methods are portable, suitable for naturalistic imaging, and are not contraindicated in subjects with electronic or metal implants [8, 11, 47, 60-70]. Sparse fNIRS imaging arrays yield poor resolution and low image quality. HD-DOT provides improved image resolution and depth profiling, particularly when used with anatomical head models [45, 71, 72]. However, as in both fMRI and fNIRS, detection, classification, and removal of motion-induced artifacts remain a challenge for HD-DOT.

Multiple fMRI studies have documented the spurious effects of motion artifacts in blood oxygen level-dependent (BOLD) fMRI despite the use of common motion suppression methods [30, 73-

¹ A version of this chapter has been published the Human Brain Mapping journal: **Sherafati A**, Snyder AZ, Eggebrecht AT, Bergonzi KM, Burns-Yocum TM, Lugar HM, Ferradal SL, Robichaux-Viehoever A, Smyser CD, Palanca BJ, Hershey T, Culver JP. Global motion detection and censoring in High-density diffuse optical tomography. Human Brain Mapping, July 2020. <https://doi.org/10.1002/hbm.25111>

77]. Motion-induced changes in T2*-weighed fMRI signals are shared across brain voxels, hence generate spatially structured artifacts. Such artifacts alter functional connectivity by decreasing long-distance correlations and increasing short-distance correlations [30, 75-77]. However, two simple data quality indices, frame-wise displacement (FD) and root mean squared (RMS) signal change over sequential frames (DVARs), are commonly used in fMRI data processing pipelines to identify and exclude data segments (motion censoring or scrubbing) from behaviorally relevant fMRI measures [30, 78, 79].

In HD-DOT, similar to fMRI, the effects of head motion are global across the field of view (FOV) and impact a majority of measurements or voxels. In fMRI, head movements shift the position of the brain in space and modulate the BOLD signal [80, 81], in HD-DOT, head motion induces a torque on the fibers in the optical imaging array that, in turn, modulates the location (Figure 3.1B center), angle, or both location and angle of optode-scalp coupling (Figure 3.1B right). Thus, motion induces artifacts in the optical signals that can appear as brief transient spikes or baseline shifts. These artifacts propagate from measurement space to voxel space in the image reconstruction process and corrupt the neuroimaging results.

Numerous strategies for managing motion-induced artifacts have been described in the fNIRS literature. However, a consensus on how best to correct for motion artifacts has not emerged [27, 28, 82]. Extant motion correction methods in fNIRS largely involve two steps: first, motion detection, and second, signal correction [46, 48, 83-87]. The fNIRS literature has largely focused on correcting motion artifacts on individual source-detector pair measurements, and much less attention has been placed on multichannel or full-array assessments. Moreover, most fNIRS studies have not assessed the efficacy of the denoising methods through comparison against fMRI.

We address these limitations by conducting a comprehensive evaluation of motion artifact removal methods for HD-DOT data by including independent measures of motion (accelerometry) and comparisons against gold-standard matched fMRI datasets. We introduce a novel index of motion, the global variance of the temporal derivatives (GVTD) for multichannel optical devices, inspired by the DVARS in fMRI [88]. For each time point, GVTD, similar to DVARS, is computed as the RMS of the temporal derivatives across time-courses. In fMRI, DVARS is calculated based on the voxels time-courses, and in optical imaging, it can be calculated based on either measurements or voxels time-courses. In HD-DOT, the equivalent of the framewise displacement (FD) cannot be defined, since there is no access to the absolute x, y, z coordinates of the image, and thus, we use an external motion sensor as the direct measurement for translational and rotational movements.

We first evaluate the efficacy of GVTD by calculating its correlation with directly transduced measures of motion using an accelerometer. We then optimize the parameters of GVTD and compare its application to voxel time-courses vs. measurement time-courses using an artifact-to-background ratio as a metric of quality. Finally, we investigate the efficiency of the GVTD-based motion detection and censoring on the HD-DOT task and resting state images by comparisons with fMRI gold standards and to other fNIRS motion removal methods.

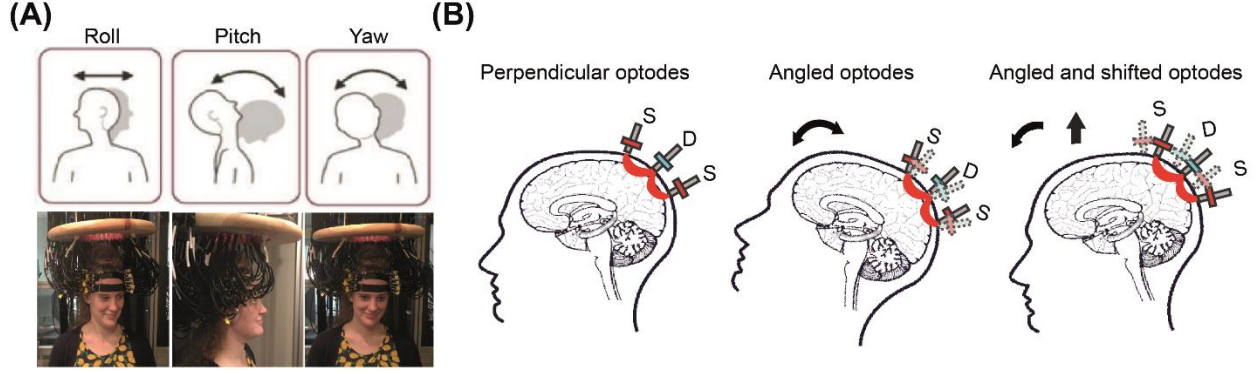


Figure 3.1 Effects of head motion on HD-DOT optode-scalp coupling. (A) Research participant wearing an HD-DOT imaging cap. Head rotation may occur about three axes (roll, pitch, and yaw). (B) Schematic illustration of how head motion can affect optode couplings. The far-left figure shows the ideal perpendicular angle between the SD optodes and the head. The middle figure shows the angled optodes as a result of nodding up and back to the center. The far-right figure shows the angled and shifted optodes as a result of nodding up and body movement.

3.2 Methods

3.2.1 Novel motion detection methods

3.2.1.1 The global variance of the temporal derivatives (GVTD)

GVTD indexes global instantaneous change in the optical time-courses. For each time point,

GVTD is computed as the RMS of the temporal derivatives across a set of measurements or voxels

(Eq. 3.1). The simple analytic formula for GVTD is:

$$\mathbf{g} = \begin{bmatrix} g_1 \\ \vdots \\ g_M \end{bmatrix}, g_i = \sqrt{\frac{1}{N} \sum_{j=1}^N (y_{ji} - y_{ji-1})^2}, \quad g_i \in \mathbb{R}_{>0}, \quad (3.1)$$

where \mathbf{g} is the GVTD vector, $y_{ji} \in \mathbb{R}$ is either the optical density change or molar HbO₂ or HbR change at spatial coordinate j . i indexes the time points, N is the number of coordinates, and M is the number of time points.

3.2.1.2 Independent measurement of head motion

A motion sensor (3-space™ USB/RS232; Yost Labs, Portsmouth, Ohio) was attached to the top strap of the HD-DOT cap in a subset of the data acquired with instructed motion (more details in

§2.6). This sensor includes a triaxial inertial measurement unit (IMU), which uses a gyroscope, an accelerometer, and a compass sensor (Figure A.2). Onboard electronics compute and report in real-time, the quaternion-based orientation relative to an absolute reference. We synchronized the outputs of the motion sensor with our HD-DOT data acquisition system using audio pulses at the start and end of data streams. The motion sensor data were down-sampled from 200 Hz to 1 Hz to match the final sampling rate of the HD-DOT data. Then, the motion sensor and HD-DOT signals were aligned by delaying the earlier signal based on the cross-correlation delay time with maximum correlation value.

3.2.1.3 Angular rotation

The angular rotation (Φ) time-course was defined as the norm of the temporal derivatives of the head orientation in terms of Euler angles (α roll, β pitch, and γ yaw), measured by the motion sensor. This index was defined in a manner similar to that of GVTd to facilitate comparisons between GVTd and motion sensor outputs (Eq. 3.2).

$$\Phi = \begin{bmatrix} \phi_1 \\ \vdots \\ \phi_M \end{bmatrix}, \quad \phi_i = \sqrt{(\alpha_i - \alpha_{i-1})^2 + (\beta_i - \beta_{i-1})^2 + (\gamma_i - \gamma_{i-1})^2}, \quad \phi_i \in \mathbb{R}_{>0} \quad (3.2)$$

In this notation, i indexes the time points, and M is the number of time points.

3.2.1.4 Artifact-to-background ratio (ABR)

To quantify the magnitude of the motion artifacts, we defined the artifact-to-background ratio (ABR; ρ), where ABR is the mean GVTd of all time points above the noise threshold (defined in §3.3), divided by the mean GVTd of all the time points below the noise threshold (Eq. 3.3).

$$\rho = (n/m) \sum_i (g_i | g_i > g_{thresh}) / \sum_i (g_i | g_i < g_{thresh}) \quad (3.3)$$

In this formula, g_i is the GVTd value at time index i , g_{thresh} is the threshold value, n is the number of time points below the threshold, and m is the number of time points above the threshold.

3.2.2 Motion removal methods

3.2.2.1 Motion censoring using GVTD

Motion censoring (scrubbing) excludes the time points (blocks) exceeding the GVTD noise threshold from further analysis of resting state and task data [89, 90]. Details concerning the noise threshold criterion are explained in §3.3. This proposed HD-DOT censoring strategy follows a similar practice that resulted in statistical improvements in the resting state as well as task fMRI data [30, 88, 91, 92].

3.2.2.2 Correlation-based signal improvement (CBSI)

CBSI motion correction is based on the assumption that oxygenated and deoxygenated hemoglobin signals are negatively correlated under all circumstances. In the presence of motion artifacts, the correlation between these two signals becomes more positive. CBSI corrects the oxyhemoglobin concentrations by subtracting the scaled deoxyhemoglobin to match the variance of the oxygenated signal. This process removes the positive correlation content between the two signals, taking into account their different amplitudes. Then, the corrected deoxy-hemoglobin is calculated by multiplying the corrected oxy-hemoglobin by the inverse of the same scaling factor between the original signals [46]. In this paper, we performed this motion correction method after spectroscopy on the down-sampled 1 Hz (Figure A.1).

3.2.2.3 Targeted principal component analysis (tPCA)

Principal component analysis (PCA) projects an arbitrary set of signals onto orthogonal principal components. Then, the principal components with the least variance are excluded, and the signal is reconstructed from the remaining components. Targeted PCA (tPCA) applies PCA to temporal epochs of the data that is identified to contain motion artifacts. tPCA reduces the risk of eliminating the physiological content in the motion-free epochs of the signal [93]. Hence, this method is

followed by a prior step of motion detection in the temporal domain. Conventionally, this motion detection is performed by setting a threshold on signal amplitudes or the windowed signal amplitude changes. In this paper, we used the Homer function "hmrMotionArtifactByChannel" to detect noisy timepoints and "hmrMotionCorrectPCA" to perform PCA, and set the parameters of this algorithm in the similar range as in the original study [93]; $t_{\text{Motion}} = 0.5$, $t_{\text{Mask}} = 2$, $\text{STDEV}_{\text{thresh}} = 20$, $\text{AMP}_{\text{thresh}} = 0.5$, $n_{\text{SV}} = 0.97$ (Tables A.1 and A.2, Figure A.1).

3.2.2.4 Wavelet filtering

Wavelet-based motion correction is based on a discrete wavelet transformation of single-channel measurements. This method assumes that the distribution of the wavelet coefficients of a motion-free signal should follow a Gaussian distribution. Therefore, motion artifacts are detected based on the deviations from the Gaussian distribution. By setting an outlier detection threshold, the coefficients associated with motion artifacts are excluded, and the clean signal is reconstructed based on the remaining wavelet coefficients [85]. We used the "hmrMotionCorrectWavelet" function, setting the interquartile parameter as 1.5, as suggested in the original paper [85] (Tables A.1 and A.2, Figure A.1).

3.2.2.5 Kurtosis-based wavelet filtering (kbWF)

The kurtosis-based wavelet filtering (kbWF) method optimizes the use of the wavelet filtering motion correction by setting the threshold based on the kurtosis of the coefficient distributions [86]. The "*hmrMotionCorrectKurtosisWavelet*" function was used with the kurtosis threshold parameter set to 3.3, as recommended in the original paper [86] (Tables A.1 and A.2, Figure A.1).

3.2.2.6 Hybrid (Spline + Savitzky Golay)

The spline and Savitzky-Golay hybrid method is a three-step algorithm that aims to identify and correct different types of motion artifact [48]. First, single-channel measurements are passed

through a Sobel filter to identify time points exceeding a threshold of 1.5 times the interquartile interval of the signal gradient. Second, this method performs a spline interpolation on those epochs containing motion to remove the baseline shifts and slow spikes. Steps 1 and 2 were introduced in a previous fNIRS motion removal method, commonly known as the motion artifact removal algorithm (MARA) [83]. After this step, the hybrid method then applies a Savitsky-Golay smoothing filter to remove the remaining fast spikes. We used the "*hmrMotionCorrectSplineSG*" function defined in the original paper with its default parameters and setting $p = .99$ and $\text{FrameSize_sec} = 1.5$ [48] (Tables A.1 and A.2, Figure A.1).

3.2.2.7 Temporal derivative distribution repair (TDDR)

Temporal Derivative Distribution Repair (TDDR) also is a three-step algorithm that aims to automatically identify and correct motion artifacts at the single-channel level. First, by computing the temporal derivative of the signal, TDDR initializes the vector of observation weights. Second, it iteratively estimates the robust observation weights by applying the resulting robust weights to the centered temporal derivative to produce the corrected derivative. Finally, it integrates the corrected temporal derivative to yield the corrected signal [84].

3.2.3 Datasets and their objective

Dataset 1: For validation, we collected an fMRI dataset in which adult subjects ($n = 8$) were scanned in both the resting state and during a hearing words (HW) task. This dataset served as ground truth. Dataset 2: As a positive control, in this HD-DOT dataset, healthy adults ($n = 12$) performed instructed motion while performing the same HW task performed during fMRI. Dataset 3: In this HD-DOT dataset, adult subjects ($n = 13$) performed the same HW task without instructed motion. Dataset 4: In this HD-DOT dataset, healthy adults ($n = 8$) were scanned while awake in a task-free (resting) state. Dataset 5: In this HD-DOT dataset, healthy term infants ($n = 11$) were

imaged in the resting state (awake or asleep). This is a previously published dataset [50]. Demographic information and the objective of using each dataset are reported in Table 3.1.

Table 3.1: Demographic information. HW: hearing words; y: year; d: day; ABR: artifact-to-background ratio.

Dataset	Number of subjects	Sex (f/m)	Age mean (std)	Condition	Modality	Objective
1: adults	8	6/2	62.37(6.3)	Rest and HW	fMRI	Gold standard
2: adults	12	8/4	25.41(2.06)	HW	HD-DOT	Instructed motion, motion sensor
3: adults	13	10/3	42.92 (19.75)	HW	HD-DOT	Natural motion method comparison
4: adults	8	5/3	30.25 (11.18)	Rest	HD-DOT	Natural motion method comparison, ABR test
5: infants	11	6/5	1.1 d (0.4)	Rest	HD-DOT	Validation for ABR test

All aspects of these studies were approved by the Human Research Protection Office of the Washington University School of Medicine. All adult participants in the previous and new datasets were right-handed, native English speakers, and reported no history of neurological or psychiatric disorders. Adults were recruited from the Washington University campus and the surrounding community (IRB 201101896, IRB 201609028). All full-term infants were recruited from the Newborn Nursery at Barnes-Jewish Hospital in St Louis, Missouri, within the first 48 hours of life (IRB 201101813). All subjects (or their guardians) gave informed consent and were compensated for their participation in accordance with institutional and national guidelines.

3.2.4 HD-DOT systems, image reconstruction, and spectroscopy

All adult HD-DOT datasets (datasets 2, 3, and 4) were collected using a previously described continuous-wave HD-DOT system comprising 96 sources (LEDs, at both 750 and 850 nm) and 92

detectors (coupled to avalanche photodiodes, APDs) [49]. Acquisition in infants was performed at the bedside using a previously reported portable continuous-wave HD-DOT system with an optode array consisting of 32 sources (LEDs, at both 750 and 850 nm) and 34 detectors [50]. The setup time for both systems was approximately 5-15 minutes for combing the HD-DOT optode array embedded in a cap design through the hair to ensure the maximum optode scalp coupling using a real-time software for light level readouts. More detailed descriptions of the imaging systems and the setup process are given in the corresponding references. Light modeling was computed using the standard MNI atlas-based absorption model; details can be found in [71]. Volumetric movies of relative changes in absorption at 750 nm and 850 nm were reconstructed after inverting the sensitivity matrix using Tikhonov regularization and spatially variant regularization [49]. Relative changes in hemoglobin concentration were obtained via a spectral decomposition of the absorption data, as previously described [49, 50].

3.2.5 Functional MRI (fMRI) system and imaging

All fMRI data were collected on a research-dedicated Siemens 3.0T Magnetom Prisma system (Siemens Medical Solutions, Erlangen, Germany) with an iPAT compatible 20-channel head coil. Blood Oxygenation Level Dependent (BOLD) sensitized fMRI data with TR = 1230 ms, TE = 33 ms, voxel resolution = 2.4 mm³, FA = 63 degrees, with a multi-band factor of 4 for both resting state functional connectivity MRI (3 runs each 10 min) and HW task BOLD (1 run, 3.5 min) were acquired for all subjects in dataset 1.

3.2.6 Paradigms

Hearing words: Subjects were seated for HD-DOT or supine for fMRI and instructed to fixate on a white crosshair against a gray background while listening to words. The HW task was administered as block design. Each trial consisted of 15 seconds of hearing words followed by 15

seconds of silence. Each run included multiple trials, $n = 10$ for dataset 2, and $n = 6$ for datasets 1 and 3. The total number of acquired runs per session was 7 (dataset 2) or 1 (datasets 1 and 3).

Instructed motion: The instructed motion was performed by subjects during the HW task (dataset 2), with 15% of the trials, including instructed motion. Participants viewed a screen with a crosshair and were instructed to perform a specific motion type when the crosshair color changed. Movements were performed for about 2 seconds every 3-5 seconds over a 15-second word presentation section. Subjects were monitored in real-time using a digital camera to ensure that they were engaged in the assigned tasks. Specific motions included (i) head turn to the left and back to center (roll, Figure 3.1A left), (ii) head nod up and back to center (pitch, Figure 3.1A center), (iii) shifting body position, (iv) taking deep breaths, and (v) raising eyebrows. Head twist (yaw, Figure 3.1A right) motion was avoided to prevent cap displacement.

Resting state: Resting state data in adults (datasets 1 and 4) were collected over 10 min runs while subjects were seated for HD-DOT or supine for fMRI and visually fixating on a white crosshair against a gray background. Subjects were asked to stay awake and still during data acquisition. The number of runs per session was 3 (dataset 1) or 1 (datasets 4). Resting state HD-DOT in infants was acquired at the bedside (dataset 5) within the first 24-48 hours of life during natural (un-medicated) sleep or quiet rest [50].

3.2.7 HD-DOT pre-processing

All HD-DOT data were processed using the NeuroDOT toolbox following the flowchart in Figure A.1 [49, 94, 95]. HD-DOT light measurement data were converted to log-ratio (using the temporal mean of a given SD-pair measurement as the relative baseline for that measurement). Noisy measurements were empirically defined as those with greater than 7.5% temporal standard deviation in the least noisy (lowest mean GVTD) 60 seconds of each run [45] and were excluded

from further processing. Then the data were high-pass filtered (0.02 Hz cut-off for task-based datasets, 0.009 Hz for resting state datasets) to remove low-frequency drift. To serve as an estimate of the global superficial signal, we computed the average of all remaining first nearest neighbor measurements (13 mm SD-pair separation in the adult system and 10 mm SD-pair separation in the infant system). This global signal estimate was regressed from all measurements [21]. After that, all adult task-based data were low-pass filtered to 0.5 Hz cut-off for to remove the cardiac oscillations [28, 46-48]. All resting state data were low-pass filtered to 0.08 Hz to remove the cardiac oscillations and to narrow the signal to the spontaneous, low-frequency fluctuations of the signal following the previous recommendations for functional connectivity analysis in both adults and infants [49-52]. Task data provide two advantages over the resting state. First, the task design can impart high amplitude and high-frequency dynamics beyond what would normally be found in the resting state. Second, the block averaging of the tasks provides an approach to lower the noise and physiological clutter in the data. So while resting state uses the common infra-slow band (0.009-0.08 Hz) of the vast majority of the functional connectivity MRI literature [49-52], the task preprocessing uses a higher filter band (0.5 to 0.1 Hz) to avoid 1/f noise [28, 46-48]. Following this bandpass filtering, the time-courses were then down-sampled from 10 Hz to 1 Hz and then used for image reconstruction. The efficacy of GVTD was evaluated at four stages of the HD-DOT processing pipeline, as indicated in Figure A.1 (green boxes) on 10 Hz sampled data. All other motion correction methods except CBSI were also performed on the 10 Hz sampled optical density signals (immediately after the log-ratio step) (Figure A.1).

3.2.8 fMRI pre-processing

fMRI pre-processing was performed using in-house 4dfp tools [96]: 1. correction for systematic slice-dependent time shifts; 2. elimination of odd-even slice intensity differences due to interleaved

acquisition; 3. rigid-body realignment for head motion within and across runs; 4. normalization of signal intensity to a mode value of 1000. Signal intensity normalization enables identification of artifact by evaluation of the signal temporal derivative. Atlas transformation was computed by the composition of affine transforms derived by a sequence of coregistration of the fMRI volumes via the T2-weighted and MP-RAGE structural scans. Head motion correction and atlas transformation was applied in a single resampling step that generated volumetric time series in $(3\text{mm})^3$ atlas space. Data underwent spatial smoothing (6 mm full width at half maximum in each cardinal direction) and temporal band-pass filtering (0.02-0.5 Hz for the HW task and 0.009-0.08 for resting state). Nuisance regressors included six rigid body values derived from head motion correction, white matter, and CSF signals and the mean whole-brain signal. Motion artifacts were reduced in resting state data through DVARS-based motion scrubbing using session-specific thresholding expressible as $g_{thresh} = \bar{\kappa} + 2.5\sigma_L$ (see Eq. 3.5 below) [97]. The fraction of censored frames was $21\% \pm 12\%$.

3.2.9 Statistical analysis

3.2.9.1 HW task response mapping in datasets 1, 2, and 3

Another objective of acquiring HW task data was to evaluate GVTd as an index of HD-DOT data quality (dataset 2). To this end, 70 trials of HW (15 sec of HW (On), 15 sec of silence (Off)) were acquired in each session; 10 trials included instructed motion; the remaining 60 trials (ordinary trials) did not. The reconstructed voxel-wise data represent the changes in the hemoglobin concentration (ΔHbO_2) in units of $\mu\text{mol/L}$ [53]. The quantitative response magnitude was then calculated with a standard general linear model (GLM). The design matrix was constructed by convolving the experimental design with a canonical HRF using a two-gamma function fitted to the in-vivo HD-DOT data, as described in [98]. Extracted hemodynamic response estimations for

each subject were then combined in a simple group-level fixed effects analysis [99]. Fixed effect analysis was adopted as we expect the variance in our dataset to be most strongly driven by scan-to-scan variability rather than from subject-to-subject differences.

3.2.9.2 Seed-based correlation analysis of functional connectivity in datasets 1 and 4

Seed regions were 5 mm radius spheres centered on coordinates used in our previous study [49].

Five seeds representing the auditory (AUD), visual (VIS), somatomotor (MOT), dorsal attention network (DAN), and frontoparietal network (FPN) networks were selected within the HD-DOT field of view. Correlation maps were generated by calculating the Pearson correlation between the time-series of each seed region with all other voxels in the field of view. Correlation maps in individuals were Fisher's z-transformed and averaged across subjects.

3.2.9.3 Similarity metric

To summarize the quality of each HD-DOT image into a quantitative reduced metric that doesn't lose the spatial structure information, we computed a Similarity score for each HD-DOT image with the corresponding image in the fMRI dataset. The Similarity metric is calculated as the voxel-wise Pearson correlation between the non-thresholded HD-DOT and the corresponding fMRI images by only including voxels in the HD-DOT field of view. HD-DOT field of view is defined as the voxels greater than 1% of the maximum sensitivity after inverting and smoothing (details explained in the supplementary materials of [49]).

3.2.9.4 Receiver operator characteristic curve

To evaluate the sensitivity and specificity of different motion detection indices, we evaluated the experimental receiver operator characteristic (ROC) curves for binary classification of clean and noisy time points by sweeping the detection threshold. We defined ground truth for motion as the time points during which the subjects performed instructed movements. The ROC curves were

then created by plotting the true positive rate (sensitivity) against the false positive rate (1 – specificity) at various threshold settings for each motion index.

3.3 Results

3.3.1 Effect of motion artifacts on HD-DOT data

We investigated the effects of various types of movements on HD-DOT data using the instructed motion. During the HW task, subjects performed five different types of instructed motion, including large movements (head rotation) and small movements (raising eyebrows) (§2.8). One way to track the effect of motion is to spatially display the measurement pair channels (Figure 3.2B). For example, for all the second nearest neighbor (nn2) pairs, we can mark sources and detectors with very high standard deviations over time during instances of instructed roll rotation (pink circles) and eyebrow motion (blue circles) (Figure 3.2B). Alternatively, one can analyze an SD-pair measurement (pair highlighted by large circles in Figure 3.2B) by comparing its time-course during runs without instructed motion ("ordinary"), or with different levels of instructed motion, i.e., low eyebrow motion or gross roll rotation (Figure 3.2C). The difference in signal quality between the clean and corrupted responses are evident after block averaging (Figure 3.2D).

We assessed the effects of different motion artifacts on the measurements by calculating the number of measurements with excessive noise for each type of motion artifact across all subjects. The HD-DOT array contains $n = 1500$ total measurements per wavelength within nn1 ~ 13 mm, nn2 ~ 30 mm, nn3 ~ 39 mm, and nn4 ~ 47 mm separations, respectively. All five motion types affected multiple SD channels distributed across the field of view; specifically, $51 \pm 8\%$ of the channels for gross body movement and $39 \pm 4\%$ for small eyebrow movement. Based on these observations, we concluded that each type of motion generates global effects. Therefore, we

adopted the GVTD as a global index of motion, taking into account optical signals over the full field of view.

Table 3.2: Percent of the noisy measurements across five different instructed movements. Noisy measurements (nn1 through nn4) in dataset 2 were empirically defined as ones having a temporal standard deviation of 7.5% or greater.

Type of motion	Roll	Pitch	Deep breaths	Body motion	Eyebrow motion
% Noisy measurements	$49 \pm 9\%$	$47 \pm 4\%$	$41 \pm 5\%$	$51 \pm 8\%$	$39 \pm 4\%$

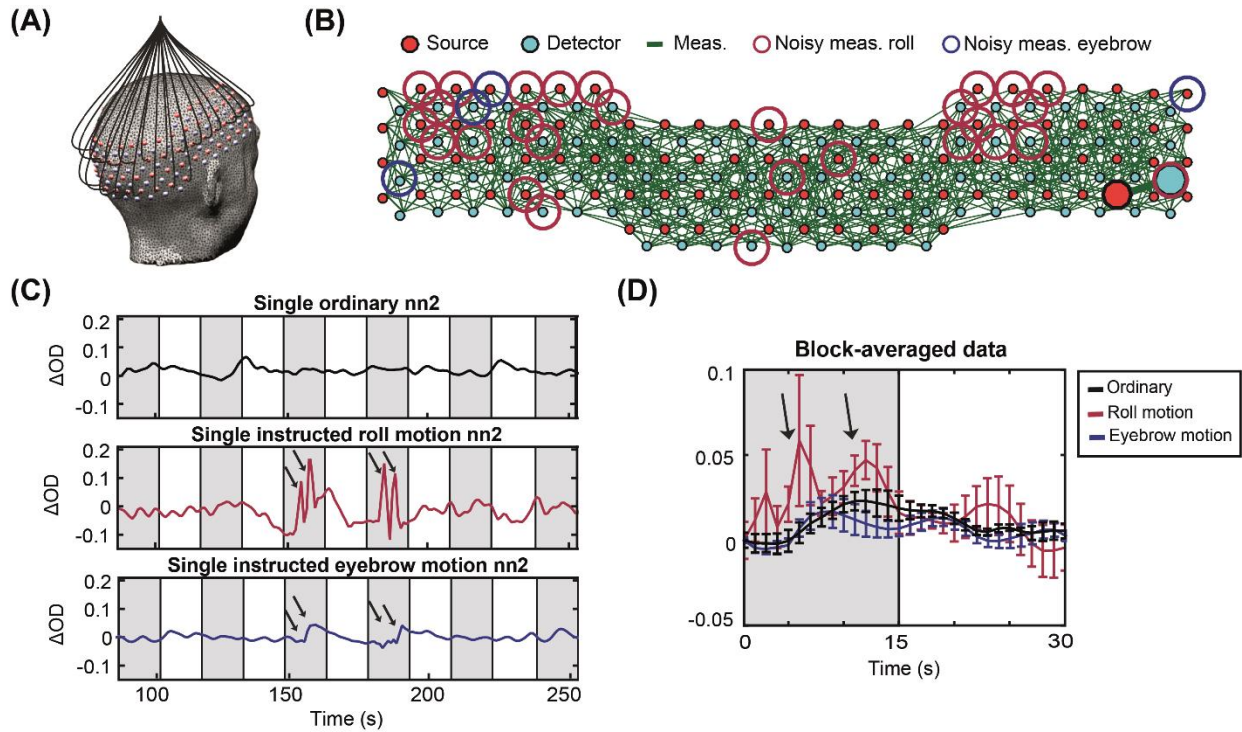


Figure 3.2: Effects of head motion on single-channel HD-DOT measurements. (A) Adult HD-DOT cap structure illustrating a subset of optical fibers. (B) Green lines indicate source-detector (SD) pairs that have a standard deviation of less than 7.5%. Source or detector locations identified as noisy for roll (large red circles) and eyebrow (large blue circles) motion, respectively. (C) Changes in the light levels of a representative SD-pair during HW runs that were ordinary (black), instructed roll motion (pink), and instructed eyebrow motion (blue). Arrows indicate motion. Gray shading indicates auditory stimulus presentation. (D) Block averages of ordinary (black), instructed roll motion (pink), or instructed eyebrow motion run (blue). Error bars represent the standard error of the mean across trials.

3.3.2 GVTd and its correlation with the head angular rotation

The global effect of motion artifacts in HD-DOT can be visualized as a matrix where each row is a measurement signal, and the columns index time (Figure 3.3A). This type of visualization is similar to fMRI "gray plots" [30, 100, 101]. The inspection of Figure 3.3A reinforces the notion that the effects of head motion in HD-DOT are global. GVTd time-course is computed in four steps. First, starting from the matrix of 850 nm μ optical density changes (Figure 3.3A), the matrix of the backward differentiation of the selected time-courses is calculated (Figure 3.3B). Then, from the matrix of the squares of backward differences (Figure 3.3C), GVTd is defined as the square root of the mean across the selected measurement array (Figure 3.3D). This sequence of steps progressively increases the sensitivity and specificity of the measure to motion (Figure 3.3A-D).

To evaluate the sensitivity of GVTd to motion, we concurrently recorded accelerometry as an independent measure in a subset of our instructed motion dataset (Figure 3.3E-H). The graded quantitative motion capture of the accelerometer provided insight into the sensitivity and specificity of GVTd to motion. To facilitate comparisons between the accelerometer and GVTd, the angular rotation was calculated based on the final head orientation time-course (§2.5, Figure 3I).

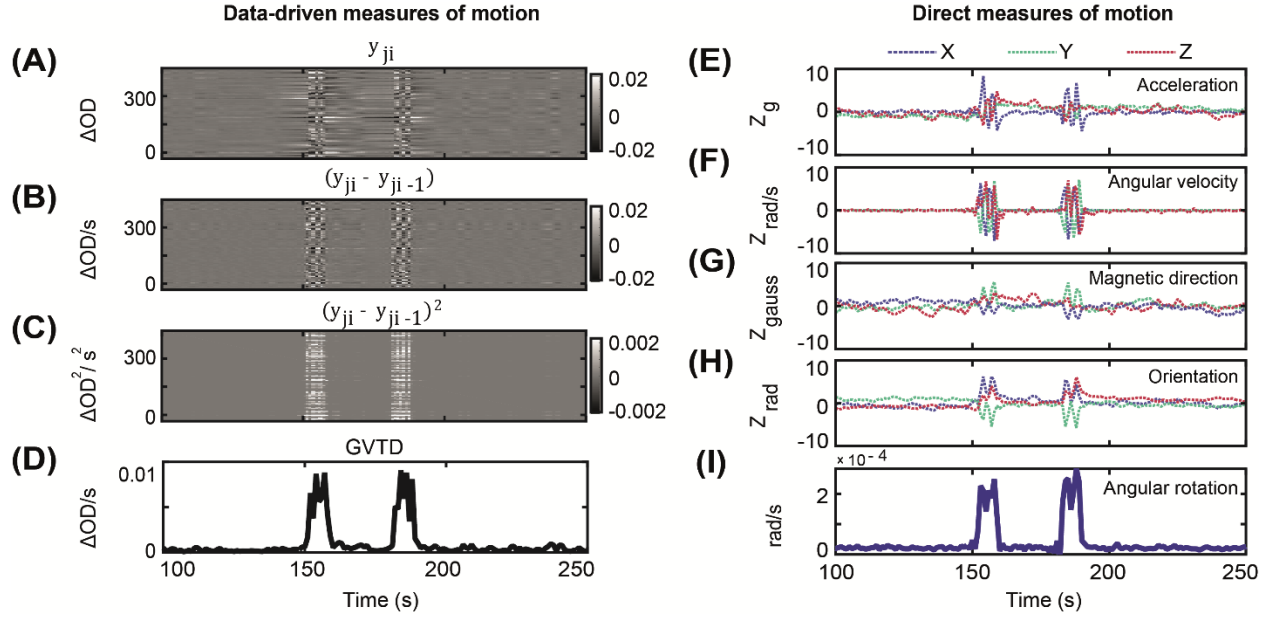


Figure 3.3: Data-driven vs. direct measures of head motion. (A) All 850 nm nn1 measurements ($n = 322$) for a run containing instructed roll motion, represented as a matrix of measurements by time. (B) Temporal derivative of the data shown in (A); note intensified contrast between instructed motion vs. neighboring time points. (C) Squared values (by element) of the matrix shown in (B). (D) GVTD time-course calculated as the RMS of the square values shown in (C). (E-H) Standardized (Z-scored) time-courses captured during instructed head motion in one subject. Colored traces correspond to x-, y-, and z-axes of the (E) accelerometer, (F) gyroscope, (G) compass, and (H) head orientation. (I) Angular rotation is calculated as the norm of the temporally differentiated x, y, and z time-courses shown in (H).

We evaluated the efficacy of GVTD and angular rotation for motion detection through different scenarios. First, we compared these two motion indices for a gross and a small artifact and found that GVTD shows a higher amplitude spike than the angular rotation in the case of small artifacts such as eyebrow motion (Figure 3.4A, B). To quantify these comparisons, we first calculated the Pearson correlation between GVTD and angular rotation (Φ) for all runs containing instructed motion. The correlations were averaged over the six subjects that had concurrent HD-DOT and motion sensor data for all runs in the session (Figure 3.4C). These correlations were greatest in cases of head rotations ($r = 0.86 \pm 0.06$ for roll and pitch) and lowest for eyebrow motion ($r = 0.46 \pm 0.2$). This difference most likely reflects the transducer characteristics of the motion sensor and

the fact that it is not sensitive to the small muscle movements when attached to the top of the HD-DOT cap.

To evaluate the sensitivity of the GVTD to motion, we leveraged the ground truth built into our instructed motion paradigm. Experimental receiver operator characteristic (ROC) curves for GVTD and angular rotation were created for binary classification of clean and noisy time points by sweeping the detection threshold (Figure 3.4D). We defined ground truth for motion as the time points during which the subjects performed instructed movements. We also plotted these ROC curves for two common temporal motion detection methods in fNIRS, i.e., absolute single-channel signal amplitudes and windowed amplitude changes for all motion types and all 850 nm nn1 measurements (Figure A.3) and compared the mean of these ROC curves against GVTD and angular rotation (Figure 3.4D). In all motion types, GVTD showed better or similar performance (AUC) compared to the angular rotation, absolute signal amplitude, and windowed amplitude change (Table 3.3).

Table 3.3: The AUC of the ROC curves across different motion detection methods. The AUC of the ROC curves of GVTD and angular rotation (based on the motion sensor outputs), the mean of the ROC of the absolute signal amplitude and windowed amplitude changes based on the instructed motion as ground truth in dataset 2.

Motion index	GVTD	Angular rotation	Signal amplitude	Windowed amplitude change
AUC	0.88 ± 0.07	0.77 ± 0.08	0.6 ± 0.04	0.76 ± 0.04

We used the instructed motion protocol to examine the relation between GVTD and angular rotation for all runs with instructed motion (Figure 3.4E). Low vs. high-motion time points (black vs. red in Figure 3.4E) were determined based on the ground truth of the instructed motion protocol

(high-motion as defined as time points when the subject performed instructed motion). When the motion was low (black dots), GVTD and angular rotation were not correlated ($r = 0.05 \pm 0.05$), but when the motion was high (red dots), GVTD and angular rotation were highly correlated ($r = 0.8 \pm 0.1$). The same log-log scatter plots for absolute signal amplitudes (Figure 3.4F) and the windowed amplitude (Figure 3.4G), show much lower correlations with the angular rotation (0.2 and 0.1, respectively) compared to GVTD (0.7).

In summary, these results show that GVTD can be used as an alternative or in conjunction with motion sensors in detecting noisy time points of data.

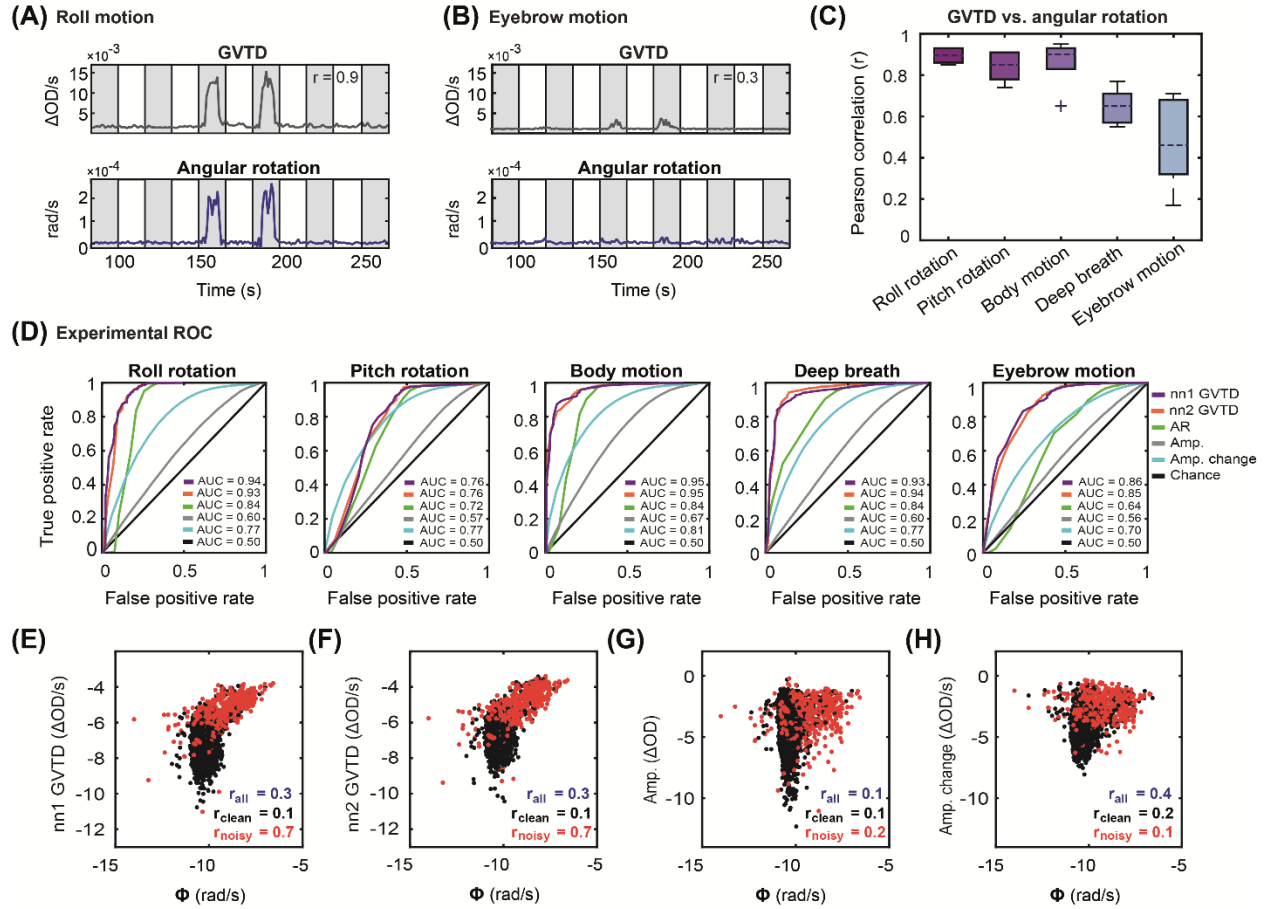


Figure 3.4: Efficacy of GVTD in motion detection. GVTD and angular rotation for an example HW run containing instructed (A) roll and (B) eyebrow motion artifacts. Gray shaded regions indicate auditory stimulation. (C) Pearson correlation between GVTD and angular rotation averaged over the six subjects with instructed motion runs. Note a high Pearson correlation of GVTD with roll, pitch, and body motion. (D) Experimental ROC plots for GVTD based on nn1 and nn2 measurements and angular rotation and the mean of the ROCs for signal amplitudes (Amp.) and windowed amplitude changes (Amp. change) for five types of instructed motion. Log-log scatter plots of (E) nn1 GVTD, (F) nn2 GVTD, (G) 850 nm nn1 signal amplitudes, (H) all 850 nm nn1 windowed amplitude changes vs. angular rotation for all runs with instructed motion. The correlation between the GVTD (either nn1 or nn2) and the motion sensor is higher than both amplitudes and the windowed amplitude changes. The cutoff between black and red dots is based on the instructed motion time points.

3.3.3 Motion detection strategy using GVTD

To censor data using the GVTD time-course, we developed an outlier detection strategy that separates good data from motion artifacts.

We assume that the detected signal, $y(t)$, is a linear combination of the true physiological signal, $S(t)$, and noise, $\epsilon(t)$:

$$y(t) = S(t) + \epsilon(t) \quad (3.4)$$

We followed the fMRI approaches for DVARS and FD and developed a data distribution driven strategy for finding motion criterion. In fMRI, $S(t)$ is approximately normally distributed [102]. Accordingly, the DVARS distribution is right-skewed [103]. Therefore, we investigated the skew of the GVTD distribution as a potential index of head motion artifact in HD-DOT. We evaluated the GVTD distribution for HD-DOT data from a still Styrofoam phantom, a low-motion trial, and a high-motion trial. The phantom GVTD histogram peaked at a relatively small value (mode = 4×10^{-5}) and exhibited a small rightward skew (Figure 3.5A). In the low-motion human data, GVTD values had a higher mode and proportionately smaller skew (Figure 3.5B). In data with instructed motion (high motion), the GVTD distribution is strongly skewed to the right (Figure 3.5C). These results suggest that the skew provides a basis for censoring HD-DOT data.

Thus, we defined a noise threshold (g_{thresh}) based on the GVTD distribution mode ($\tilde{\kappa}$) plus a constant (c) times the standard deviation computed on the left (low) side of the mode (σ_L). The right tail of the GVTD distribution corresponds to motion artifacts (Eq. 3.5). Thus,

$$g_{thresh} = \tilde{\kappa} + c\sigma_L \quad (3.5)$$

where $\tilde{\kappa}$ is the histogram mode and σ_L is computed as $\sigma_L = \sqrt{(1/n_L) \sum_{g_i < \tilde{\kappa}} (g_i - \tilde{\kappa})^2}$, where n_L is the number of GVTD time points less than $\tilde{\kappa}$. The value of c controls the trade-off between the exclusion of artifact vs. data loss. In this study, GVTD mode is simply calculated as the value of the bin with the maximum height. Two alternative approaches for calculating the mode of a histogram are explained in Appendix A (§A.1 and §A.2) using parabolic interpolation and kernel density estimation methods.

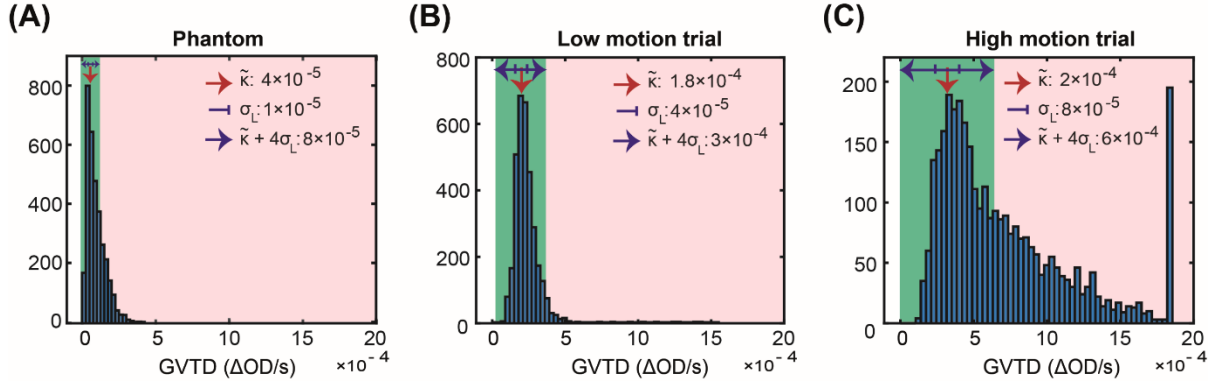


Figure 3.5: Motion threshold determination using GVTD. Histograms of the GVTD values for (A) a Styrofoam phantom, (B) a low-motion run, and (C) a high-motion run in one subject. Note the constant x-axis limits; values above that limit fall into the last bin. Note mode (red arrow), left standard deviation, and noise threshold computed according to Eq. 3.5. Pink and green shading indicates GVTD values that do or do not exceed the noise threshold.

3.3.4 Determining the best stage for performing GVTD-based motion detection and censoring

GVTD is a generic measure that can be applied to any data in the form of channels (or voxels) by time. Therefore, we needed to determine where in the processing pipeline, GVTD should be performed. We evaluated four potential locations (green boxes in Figure A.1). To evaluate GVTD's ability to separate noise from the signal, we defined an artifact-to-background ratio (ABR) as the mean of the GVTD values above a noise threshold over the mean of the GVTD values below the threshold. Specifically, GVTD was calculated for; **a**) SD-pair log-mean optical densities (*"after log-mean"*; unit = optical density change per second (ΔOD/s)), **b**) after temporal filtering before superficial signal regression (SSR) (*"after filtering no SSR"*; unit = ΔOD/s), **c**) after both temporal filtering and SSR (*"after filtering with SSR"*; unit = ΔOD/s), and **d**) on reconstructed image voxels (*"after reconstruction"*; unit = molar HbO₂/s). These results were compared based on their ABR means on two different datasets with the natural motion to determine the most effective GVTD

strategy. GVTD time-courses, GVTD histograms, and their associated gray plots calculated at these four stages for resting state data collected with two HD-DOT systems (example of a run from the adult HD-DOT data in Figure 3.6A-C). The ABR index (Eq. 3.3) was calculated using the motion threshold defined as $g_{thresh} = \tilde{\kappa} + 4\sigma_L$ (Eq. 3.5). Results showed that ABR was consistently highest after both filtering and superficial signal regression but before image reconstruction in both datasets 4 and 5 (Figure 3.6D).

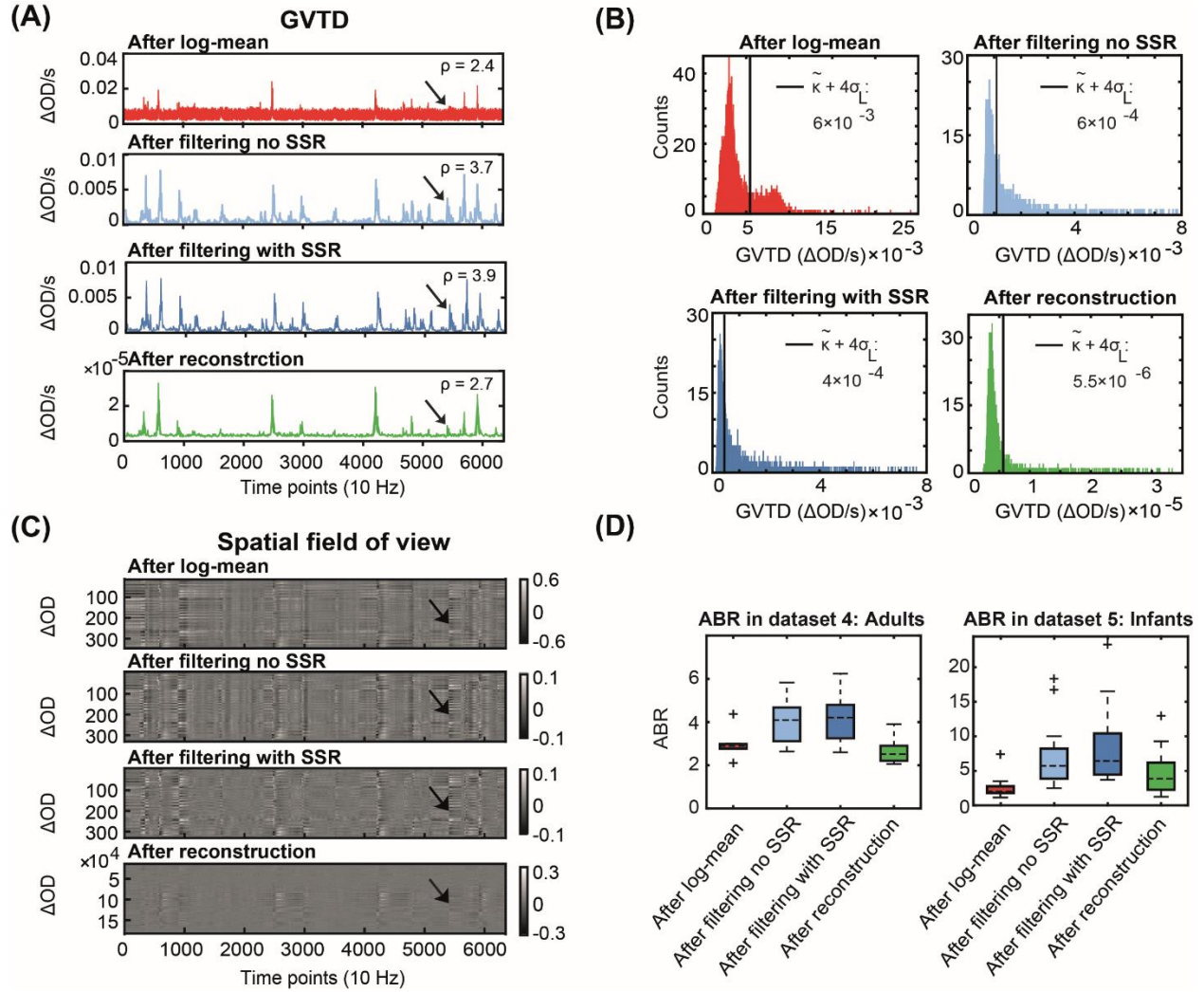


Figure 3.6: Implementing GVTD in HD-DOT data processing pipeline. (A) GVTD computed after log-mean, after filtering and without SSR, after filtering and with SSR, and after reconstruction. (B) Histograms of the GVTD values for the four time-courses; black lines indicate the noise threshold. (C) Four gray plots associated with the four GVTD time-courses shown in (A). Black arrows indicate a small motion artifact. Note the greatest contrast between the motion artifact and the baseline after filtering (third time-course). (D) ABR values calculated for all four processing stages for all subjects in datasets 4 and 5. GVTD after filtering (light and dark blue) was maximal in all cases and the highest after filtering with SSR (dark blue).

3.3.5 Indexing data quality with GVTD in task HD-DOT data by comparison against fMRI

Dataset 2 was used to evaluate the ability of GVTD to index the HD-DOT data quality. HD-DOT responses to hearing words were compared to the group-mean fMRI response to the same task,

which was independently acquired in a separate experiment and treated as a "gold standard". We rank-ordered ordinary HD-DOT trials for each subject according to their mean GVTD value; for each subject, the ten lowest and ten highest GVTD ordinary trials were defined as "low-motion" and "medium motion". The instructed motion trials were defined as "high motion". Responses were extracted from a fixed ROI defined as $P < 0.05$ in the fMRI dataset (Figure 3.8A, 3rd column map), expressed as percent signal change. The Pearson correlation between the HD-DOT and fMRI time-courses were computed for each of the three HD-DOT conditions (Figure 3.7B-D). This correlation progressively decreased from 0.97 for low-motion to 0.86 for medium motion, to 0.78 for instructed motion (Figure 3.7E). Medium motion responses (Figure 3.7C) were comparable to fMRI, but with a smaller peak value and higher mean squared error (0.08). Trials that GVTD identified as low-motion (Figure 3.7B) generated the cleanest maps with the lowest mean squared error (0.06). Accordingly, the GLM-derived beta-values were greater in the low as compared to high-motion trials in most subjects (Figure 3.7G).

A cautionary point regarding GLM-derived beta values is raised by the instructed motion trials, which generated the highest mean squared error (0.12) as well as the greatest BOLD response modulations; hence, the greatest GLM-derived beta values (Figure 3.7H). These response time-courses were the least similar to those obtained by fMRI (Figure 3.7F) and were accompanied by voxel-wise activations outside of the auditory cortex. Thus, the apparently strong HD-DOT responses in the instructed motion condition are attributable to motion artifact, as detected by GVTD (Figure 3.7E). We conclude that the results shown in Figure 3.7 demonstrate that GVTD effectively indexes HD-DOT data quality. Additional results derived from the HW response analysis show a progressively lower similarity of the HW responses for fMRI results in association with greater GVTD values (Figure 3.7E, F). The relationship between low-motion and medium

motion data within each session shows that responses are systematically greater in low-motion as opposed to medium motion (true in 15 out of 17 sessions). The responses are comparably compromised by spontaneous motion in medium motion trials (as indexed by greater GVTD) and spuriously higher in instructed motion trials with the highest GVTD scores (Figure 3.7G, H).

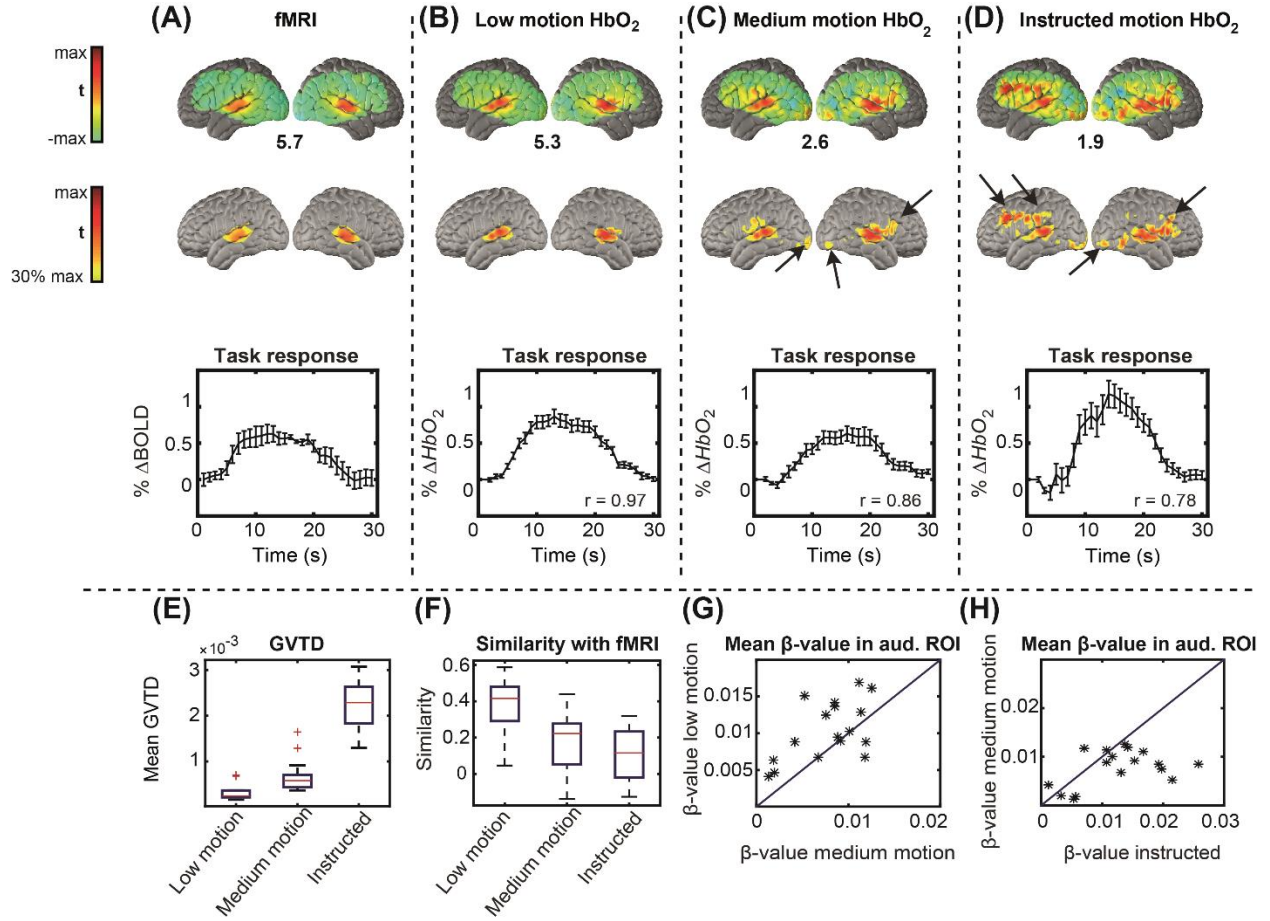


Figure 3.7: Indexing motion using GVTd in HD-DOT hearing words HbO₂ maps. Voxel-wise maps are shown in the first and second rows; the percent signal changes are averaged over a region of interest (ROI) and shown in the 3rd row. Error bars on the time-courses indicate standard error of the mean across sessions. (A) Reference dataset. (B) Low-motion data. (C) Medium motion data. (D) Instructed motion data. Black arrows indicate false-positive responses, designated since they occur outside auditory ROI defined based on the reference fMRI dataset. (E) Mean GVTD values across all trials in low-motion, medium motion, and instructed motion data. (F) Mean similarity of the maps in each condition with the reference dataset, similarity defined as the voxel-voxel Pearson correlation. (G) Scatter plot of responses in low vs. medium motion ordinary trials; GVTd indexed stronger responses in low-motion trials in 15 of 17 sessions. (H) Scatter plot of medium motion vs. instructed motion trials; note the higher spurious response magnitudes for the instructed motion.

3.3.6 Comparison between motion removal methods applied to HW task HD-DOT data

To compare the performance of different motion removal methods on HD-DOT data, we used dataset 3, acquired in older subjects ($n = 13$; 42 ± 19.75 years old) performing the hearing words

task (no instructed motion). Dataset 3 included a wide range of motion contamination levels. The details of the various motion removal methods used in this analysis are explained in §2.3. Responses were evaluated in terms of statistical significance at the voxel and ROI levels as well as time-course similarity with fMRI.

Without motion removal, the group-level t-statistic map contained several spurious activations that are not present in the fMRI results (Figure 3.8A, B). Moreover, the expected superior temporal cortex response did not achieve statistical significance at $P < 0.05$. In this analysis, the GVTD threshold was computed as $g_{thresh} = \tilde{\kappa} + 3\sigma_L$ (Eq. 3.5). Exemplary low and motion and high-motion blocks are illustrated in Supplementary Figure A.4. This threshold excluded all blocks in 6 subjects, leaving 7 subjects contributing to the final result illustrated in Figure 3.8C. Results obtained with TDDR, tPCA, CBSI, kbWF, hybrid (Spline + Savitzky Golay), and wavelet filtering are illustrated in Figure 3.8D-I. GVTD censoring, TDDR, and CBSI methods recovered bilateral superior temporal cortex activations in thresholded t-statistic maps ($P < 0.05$). tPCA and hybrid methods also recovered a unilateral right hemisphere activation. However, no statistically significant ($P < 0.05$) responses were obtained with the other methods (wavelet and kbWF).

We quantified the performance of the results shown in Figure 3.8B-I using two metrics: 1. Similarity score, defined as the voxel-wise Pearson correlation between the non-thresholded maps and the fMRI gold standard map, and 2. Mean t-value in the auditory ROI defined $P < 0.05$ in the fMRI t-map (Figure 3.8A, 3rd column). The spatial similarity to fMRI was greatest for the GVTD-censored map, followed by TDDR, tPCA, hybrid, not-corrected, CBSI, wavelet, and kbWF maps (Figure 3.8J). The mean ROI t-value was greatest for the GVTD-censored maps, followed by TDDR, CBSI, hybrid, not corrected, tPCA, kbWF, and wavelet corrections (Figure 3.8K). As noted above in §3.5, artifacts can spuriously increase apparent response magnitudes; hence, GLM-

derived t-values. This observation underscores the value of comparing HD-DOT results to those of fMRI.

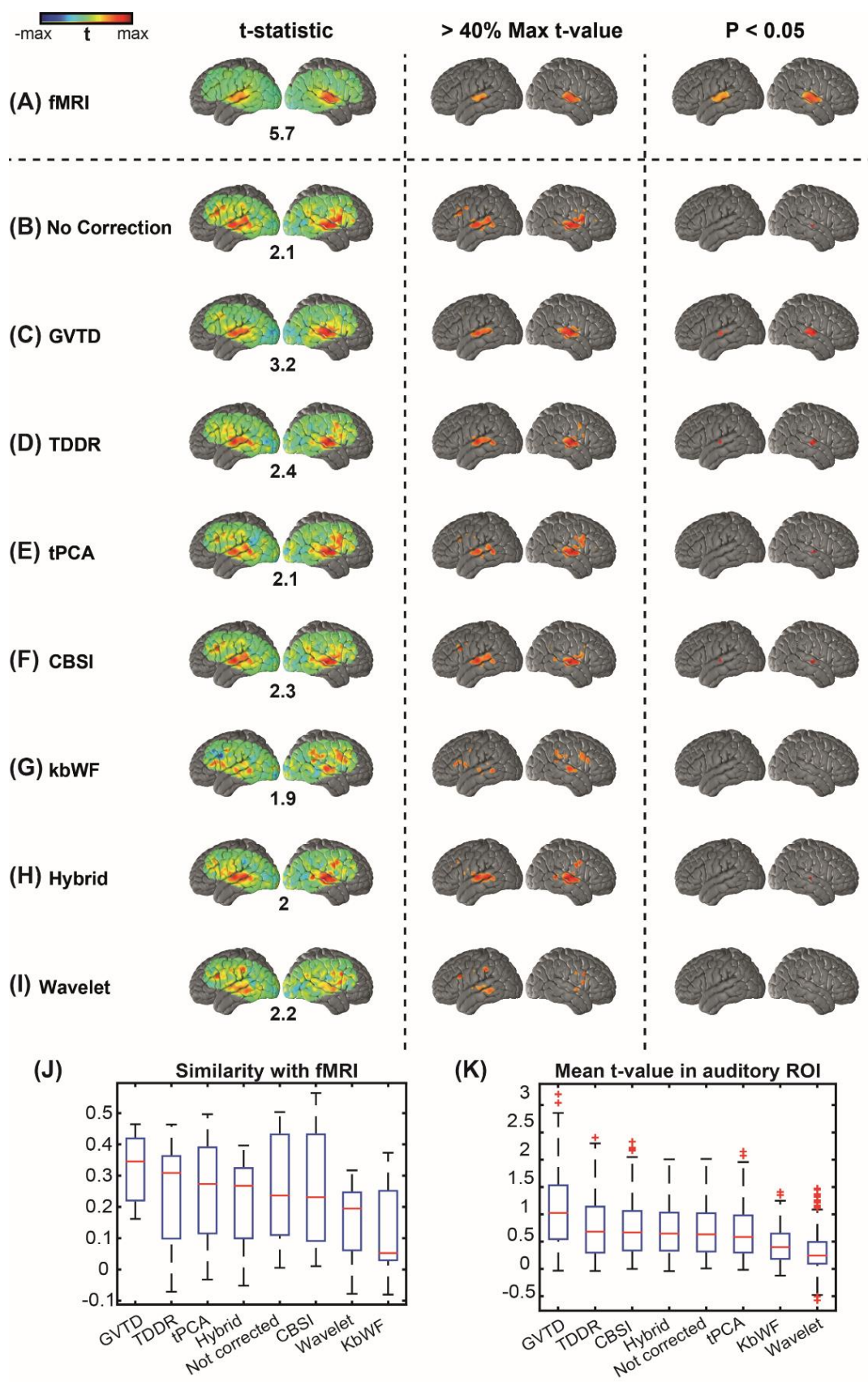


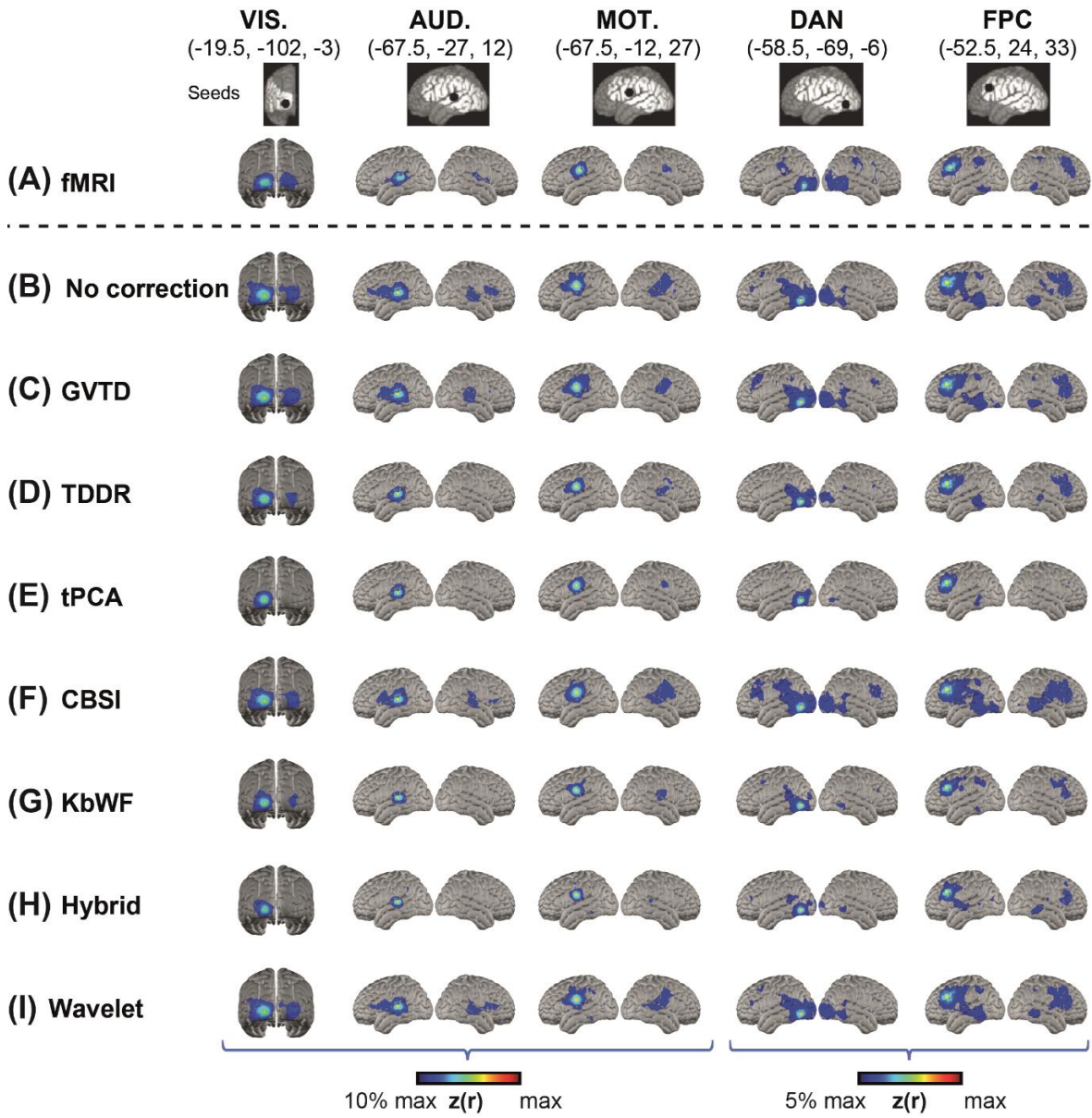
Figure 3.8: Efficacy of motion removal methods in task HD-DOT data. Three columns represent the same t-statistic map for each row with 1. No threshold, 2. thresholded at 40% of the maximum t-value of each method (mapped as an alternative visualization), and 3. Thresholded based on the $P < 0.05$ statistical significance. (A) fMRI maps based on reference dataset 1. HW map for dataset 3 with (B) no motion correction. (C) GVTB-based motion censoring, (D) TDDR (E) tPCA (F) CBSI (G) kbWF (H) hybrid, and (I) wavelet motion correction methods. (J) The similarity between the non-thresholded t-statistic maps is calculated based on the voxel-voxel Pearson correlation with fMRI t-statistic map. (K) The mean t-value is calculated in the auditory ROI based on the fMRI HW map thresholded at $P < 0.05$ shown in panel A column 3.

3.3.7 Comparison between motion removal methods applied to resting state HD-DOT data

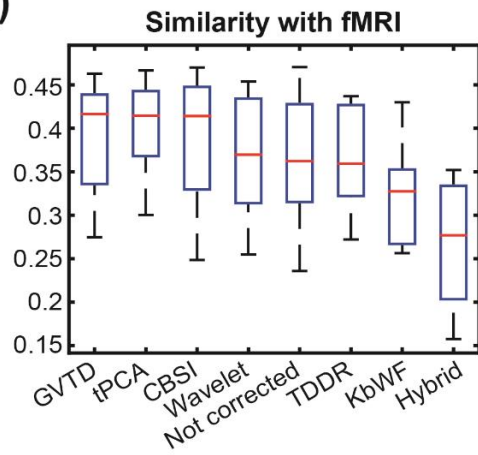
We compared the performance of different HD-DOT motion removal methods in application to resting state HD-DOT data using dataset 4 ($n = 8$ adults, 30.25 ± 11.18 years old). Seed-based functional connectivity (FC) was computed using the 5 seed ROIs (§2.9.4, Figure 3.9 top row). In parallel with §3.6, we quantified the performance of each correction method using two metrics: 1. similarity score, defined as the spatial similarity between the HD-DOT and fMRI FC maps; and 2. Mean FC (Fisher z-transformed correlation) in functionally connected ROIs identified in the fMRI data. The spatial similarity was computed as the Fisher z-transformed Pearson spatial correlation between non-thresholded maps, evaluated over the HD-DOT field of view (white area illustrated in the top row of Figure 3.9). Mean FC was evaluated in the colored ROIs illustrated in Figure 3.9A. Thus, this measure reflected simple homotopic FC in primary cortical areas as well as ipsilateral FC in the higher-order networks (DAN and FPC). The GVTB threshold was computed as $g_{thresh} = \tilde{\kappa} + 10\sigma_L$ (Eq. 3.5). This lenient threshold minimized data loss. On the basis of preliminary testing, GVTB censoring was extended to retain only epochs of duration at least 30 seconds.

The results obtained by the various correction methods are shown in Figure 3.9B-I. The most extensive HD-DOT FC maps were obtained in uncorrected data (Figure 3.9B). However, these

maps were not spatially most similar to the fMRI gold standard dataset. Rather, GVTD censoring (Figure 3.9C) yielded HD-DOT FC maps most similar to fMRI (Figure 3.9J). Of all censoring methods, GVTD yielded the greatest FC in the evaluation ROIs, followed by wavelet, CBSI, TDDR, tPCA, kbWF, and hybrid corrections (Figure 3.9K). As in the HW task responses, strong FC in the evaluation of network ROIs does not necessarily indicate good data quality, especially when accompanied by spurious effects outside of the network identified on the basis of fMRI (e.g., as seen in the no correction, wavelet, and CBSI maps). On the other hand, some methods may overcorrect, leading to falsely weak correlations (TDDR, tPCA, kbWF, and hybrid methods).



(J)



(K)

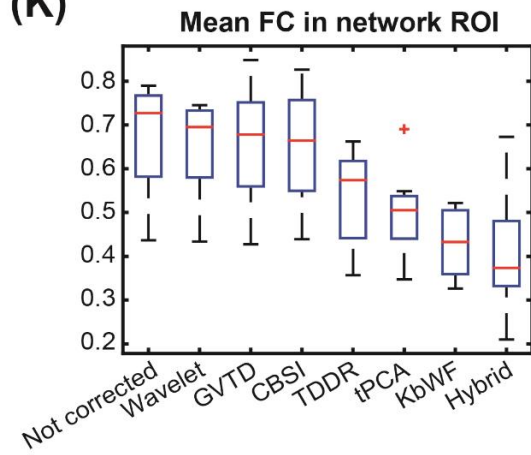


Figure 3.9: Efficacy of motion removal methods in resting state HD-DOT data. Five columns represent the seed maps for visual (VIS.), auditory (AUD.), somatomotor (MOT.), dorsal attention (DAN), and frontoparietal (FPC) networks. (A) fMRI maps based on reference dataset 1. HD-DOT maps for dataset 4 with (B) no motion correction, (C) GVTB-based motion censoring, (D) TDDR, (E) tPCA, (F) CBSI, (G) kbWF, (H) hybrid, and (I) wavelet motion correction methods. Spatial similarity (J) was computed as the Fisher z-transformed spatial correlation between the HD-DOT and fMRI FC maps, evaluated over the HD-DOT FOV (white area illustrated in the top row). (K) ROI-based FC was evaluated as the mean Fisher z-transformed correlation with the seed in the colored regions shown in panel A. These regions were determined by thresholding the group-level fMRI FC maps at 10% for lower-level networks (VIS., AUD., and MOT.) and 5% for higher-level networks (DAN and FPC) of maximum $z(r)$ value.

3.4 Discussion

3.4.1 A general summary of the novel strategies and findings

We developed a novel motion detection method suitable for high-density optical imaging arrays, inspired by the DVARS in fMRI [88]. Specifically, we defined the global measure of variance in the temporal derivative across measurement channels (GVTB) and developed a method for denoising structured artifacts in HD-DOT. We found that GVTB successfully indexes motion artifacts in HD-DOT and has higher sensitivity and specificity (evaluated using AUC of the ROC curve against the ground truth of instructed motion) for motion detection compared to an accelerometer motion sensor and to single-channel motion detection methods commonly used in fNIRS (absolute signal amplitudes and windowed amplitude changes).

While there are a number of papers evaluating motion removal methods for standard fNIRS [46, 48, 83-86, 93, 104-107], the literature on motion removal strategies for HD-DOT is limited. Previous studies lack some combination of HD-DOT datasets and comparisons to gold standard data (fMRI) for image quality validations, and most are restricted to single-channel motion detection. In this paper, we introduce a novel approach for evaluating the efficacy of motion removal methods in HD-DOT by comparison against matched fMRI datasets.

We show that the mean GVTD score is correlated with the similarity of the HD-DOT task images to those of fMRI. Thus, the mean GVTD score can be used to classify datasets as either clean or noisy (Figure 3.7). We also show that applying GVTD censoring to both task and resting state HD-DOT datasets outperforms other fNIRS-based motion correction methods and makes HD-DOT maps more similar to those of fMRI. Together, HD-DOT imaging arrays and anatomical atlas combined with GVTD motion censoring, all aid in making HD-DOT data more comparable to fMRI and furthers the use of HD-DOT as a surrogate to fMRI.

3.4.2 Optimizing the implementation of GVTD in the HD-DOT processing pipeline

We optimized the use of GVTD motion detection in HD-DOT by testing it at different steps of the processing pipeline using the artifact-to-background ratio (ABR). In fMRI, DVARS has only been evaluated before and after filtering [101]. In contrast, in HD-DOT, we can consider GVTD in either measurement space or image space (after image reconstruction). Our results show that the ABR was highest in measurement space prior to image reconstruction and after filtering the high-frequency content of the data. It was also statistically better when performed after SSR, a common fNIRS, and DOT processing step (in datasets 4 and 5). Therefore, based on our ABR analysis, we recommend performing GVTD after filtering the measurements, but prior to image reconstruction.

An important decision with GVTD is to determine the censoring threshold. Since the baseline GVTD value was different across people, similar to findings with DVARS in fMRI [97], we evaluated a noise detection strategy based on the GVTD distribution (histogram) specific to each subject. The differences in the baseline GVTD distribution is possibly due to variable physiological signal levels as well as respiratory patterns, heart rate, facial muscle activity, restlessness, tremor, etc. [30, 101]. Therefore, we developed an outlier detection strategy

individualized for each subject's data that semi-automates the noise threshold determination and takes into account subject differences. Specifically, we set the threshold using the GVTD distribution mode ($\tilde{\kappa}$) plus a constant (c) determined based on the left side (lower side) of the mode of the GVTD distribution. For practical implementation, we recommend that the threshold be greater than the standard deviation of the baseline signal.

3.4.3 Evaluation and validation of denoising through comparisons to fMRI

Most fNIRS studies measure the efficiency of motion removal techniques based on the recovery of a synthetic HRF [27, 28, 48, 82], or, in the case of real data, based on the variance across subjects or datasets [82]. However, since HD-DOT is focused on creating images comparable to fMRI, throughout this paper, we have used an fMRI dataset with the same task and resting state paradigm used in our HD-DOT datasets as a gold standard for evaluating the efficacy of different motion removal methods. The comparisons were based on the voxel-voxel Pearson correlation of the spatial HD-DOT maps and the fMRI maps. We find that, for both task and resting state functional connectivity, comparisons to fMRI enables identifying false negatives, false positives, and localization errors (Figures 3.8, 3.9), all of which would be difficult to determine without a target image. In vivo imaging enables a much stronger evaluation than in silico simulations; fMRI data contains real image features, including the spatial extent, signal magnitude, distribution of spatial frequencies, and time-courses.

Using the fMRI comparisons, we ranked ordered several motion removal methods in both task and resting state data. The general pattern observed was that motion censoring using GVTD worked best, with near contenders being CBSI, TDDR, and following those, targeted PCA in both task and rest data. TDDR and tPCA both suppressed the mean t-value in the auditory ROI and FC in the evaluation ROIs, which may indicate overcorrection, i.e., removal of the true signal. Wavelet

filtering ranked second after GVTD censoring in resting state data both in terms of similarity with fMRI and mean FC in the resting state networks. This is in distinction to its lower performance in the task data.

3.4.4 On the different performance of motion correction methods in fNIRS literature

A striking aspect of the fNIRS literature is the variable performance of motion correction methods across different studies [27, 28, 48, 82, 84, 86]. One possible reason for the variability between the studies could be the different levels of motion present in each study. This variability has also been evaluated in a recent fNIRS study [82]. To address this topic, we performed a supplementary analysis of the low-motion, medium motion, and high-motion HW task data in dataset 2 (Figure 3.7). We evaluated the performance of different motion correction methods on different levels of motion artifacts in these three categories (Figures A.6, A.7).

This analysis shows that, in the low-motion group, all methods can preserve bilateral auditory cortex HW responses. In the medium and instructed motion groups, GVTD, TDDR, CBSI, and tPCA again outperformed other methods by recovering either a unilateral or bilateral HW activation with no obvious false positives in the $P < 0.05$ thresholded maps (Figure A.6). Note that, in the high-motion data (instructed motion group), none of the motion correction techniques fully recovered bilateral auditory responses (present in fMRI). However, GVTD was able to distinguish between clean vs. motion-corrupted data (Figure 3.7). We hypothesize that GVTD can provide a means of rank-ordering data based on quantitative motion estimation (as suggested in Figure 3.7), something that is normally done subjectively prior to applying motion correction methods. Thus, GVTD may be useful also in denoising sparse fNIRS data. This notion could be tested by evaluating the efficacy of GVTD in sparse fNIRS arrays or by subsampling the HD-DOT imaging array.

GVTD focuses on motion detection, followed by simple censoring. GVTD could be used as an alternative to either absolute signal amplitudes or windowed amplitude changes included in the Homer2 code package [108]. Further, GVTD could be used in conjunction with motion correction methods such as spline interpolation (MARA) [83], Kalman filtering [104, 109], PCA [104], tPCA [93], Hybrid methods [48], or any method that depends on motion detection in the temporal domain. However, we note that, in the results presented here, GVTD-based censoring alone provided better image quality than any of the alternative motion correction procedures.

3.4.5 Strengths and limitations of the GVTD-based motion censoring

When tested in HD-DOT, the most promising results were obtained using GVTD-based motion censoring. A likely reason for GVTD efficacy is that it leverages the effect of small artifacts across many measurements. The simplicity of GVTD censoring guarantees that the signal is neither over-smoothed nor overcorrected.

As described here, GVTD is used as a binary classifier to censor the time points marked as noisy. However, it also could work with a non-binary weight associated with the time points based on their GVTD value to soften the impact of threshold choice. For example, time points with GVTD values closer to the GVTD distribution mode could be assigned higher weights than ones further from the mode [110].

Another important challenge in scrubbing data is the tradeoff between losing signal vs. removing noise [111]. For motion criterion, one can ensure that sufficient data remains after censoring by tuning c (Eq. 3.5). Another approach would be to use GVTD to determine the useable data yielded from a run and then adjust the data collection to either collect more data within the session or add sessions to the study. These active data quality approaches are currently being pioneered in fMRI with runtime assessment of motion [112-114].

3.4.6 Summarizing the consensus regarding the top-performing denoising strategies in the fNIRS literature

Among the fNIRS-based methods that worked best for HD-DOT, besides GVTD, CBSI performed well in both task and resting state data. CBSI does not require tuning of parameters but has been less recommended in the literature [48, 84] as it relies on the assumption of a negative correlation between HbO_2 and HbR . Therefore, it is limited to populations in which a normal correlation between HbO_2 and HbR can be assumed [46].

The TDDR method performed well in the task HD-DOT data and fairly well in the resting state analysis. TDDR, like CBSI, does not require tuning of parameters. However, one disadvantage of TDDR is that it relies on the derivative of single measurements and, thus, is less sensitive to small motion artifacts such as eyebrow motion. Moreover, TDDR only performs an efficient motion correction on the low-frequency content of the data, because the higher frequencies inflate the variance of the temporal derivative distribution and create bias in the distribution of estimates [84]. However, we showed that the noise content is still present in the data after band-pass filtering (see post-filtering gray plots in Figure 3.6C showing residual artifact during motion).

Targeted PCA also yielded HD-DOT maps similar to those in fMRI but with decreased response magnitudes in both task and resting state data. tPCA removes a fixed proportion of variance through the removal of the largest principal component; hence, as observed here, is prone to overcorrection [84, 93].

Wavelet filtering, despite a poor performance in task data, showed good performance in resting state HD-DOT data. However, this method is computationally expensive. On average, for both HW and rest HD-DOT runs, wavelet filtering ran ten times slower than other motion correction or

censoring methods. The kbWF method, while faster than the full wavelet approach, did not perform well in either task or rest HD-DOT data.

3.5 Conclusion

We developed GVTd, a novel motion detection metric, and optimized its use in the HD-DOT pre-processing pipeline. GVTd can be used alone or in combination with other motion correction methods to increase the quality of data obtained with multi-channel optical imaging systems. We evaluated GVTd using several independent HD-DOT datasets, including an instructed motion protocol, accelerometer motion measures, and a matched fMRI dataset serving as ground truth. Although GVTd-based censoring removes data, the obtained HD-DOT maps were most similar to those of fMRI, and it outperformed alternative motion correction methods previously described in the fNIRS literature.

Chapter 4: Mapping Deep Brain Stimulation's Impact on Cortical Networks Using HD-DOT²

4.1 Introduction

Deep brain stimulation of the subthalamic nucleus (DBS STN) in Parkinson disease (PD) can provide substantial motor benefit [115, 116], yet can also produce unwanted cognitive side effects [117-127]. Although the neural mechanisms underlying benefits and side effects of these implants are not well understood, current hypotheses center on the potentially measurable yet currently undefined effects within downstream cortical networks [116, 128-131]. The current literature hypothesizes that downstream network-level effects are a critical mechanism of the DBS's influence on motor and non-motor behavior [128, 130, 132]. However, our ability to test this hypothesis has been limited because common imaging modalities either do not have the temporal resolution necessary to discern resting state functional connectivity (FC) of cortical networks (e.g., PET) or are not suitable or safe for patients with implanted DBS (e.g., fMRI) [133, 134].

HD-DOT uses a collection of functional near-infrared spectroscopy (fNIRS) measurements, free of radiation exposure concerns, and without electrical/metal artifacts or contraindications or safety concerns for DBS. However, common fNIRS systems are critically hampered by typically sparse measurement distributions that lead to poor anatomical specificity, unreliable image quality due to crosstalk with scalp signals [12-14], poor spatial resolution, limited field of view [15], unstable point spread functions (PSF) [15], and uneven spatial coverage [6, 16]. HD-DOT solves these problems by using high-density interlaced source and detector imaging arrays that support densely

² This chapter is summarizing the results of a two year study that was submitted and approved for an R01 NIH grant by our team lead by Drs. T. Hershey and J. P. Culver.

overlapping measurements and anatomical head models [17-20] that together result in higher spatial resolution [15], stable PSFs, and greatly improved isolation of brain signals from scalp signals [15, 21]. We have demonstrated that HD-DOT accurately maps functional connectivity (FC) within and between cortical resting state networks (RSNs) in the outer ~1cm of the cortex [20, 22, 55, 135-140] with a comparable temporal and spatial resolution to fMRI in control populations. HD-DOT has greater comfort than fMRI or PET (patients sit upright in a comfortable chair), no radiation exposure (as in PET), no electrical artifacts (as in EEG/MEG), no metal artifacts (as in fMRI), and no contraindications or safety concerns for DBS patients (as in fMRI).

Table 4.1: A comparison of imaging modalities for studying PD with DBS.

	fMRI	PET	EEG/ MEG	fNIRS	HD- DOT
DBS Compatible	No	Yes	Yes	Yes	Yes
Radiation Free	Yes	No	Yes	Yes	Yes
Spatial Resolution	Excellent	Good	Fair	Poor	Good
Free of Scalp Artifacts	Excellent	Excellent	Good	Poor	Good
Tomographic Imaging	Excellent	Excellent	Good	Poor	Good
Temporal Resolution	Good	Poor	Excellent	Good	Good
Electrical Artifact Free	No	Yes	No	Yes	Yes

Compared to fNIRS, HD-DOT has a significantly better spatial resolution, and tomographic imaging is free of scalp artifacts (see Table 4.1 and Figure 4.1 [141]) and uses a standardized stationary and relatively broad field of view imaging array. Both approaches use the same basic measurement type, involving a source that deposits safe near-infrared light into the head and a detector that measures light emanating from the head at some distance away (e.g., 30 mm).

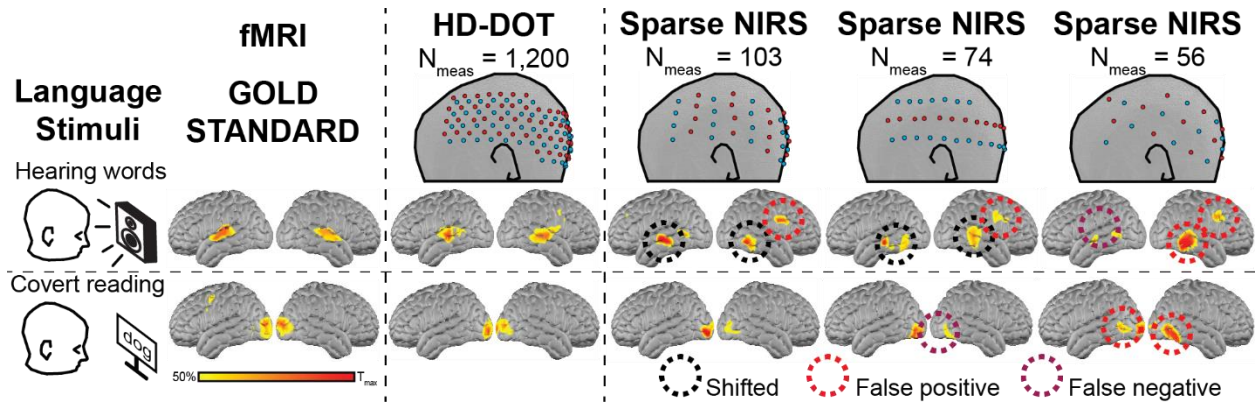


Figure 4.1: Data quality of HD-DOT vs. sparse NIRS. Subject-matched comparisons of functional activations in response to auditory and visual presentations of words clearly highlight multiple artifacts - including shifted, false positive, and false negative activations - when using any of three common sparse NIRS grid layouts. By contrast, HD-DOT yields excellent agreement with fMRI with dramatic improvements in image quality over NIRS. Fishell et al., 2019.

These source-detector pairs (SD-pairs) provide a crescent shape sampling pattern that, while peaked in the scalp, extends deep enough to record hemodynamic changes in the brain. However, the key difference is that sparse fNIRS systems use only a few SD-pairs (typically about 16-40) sparsely distributed, non-overlapping, and only at one SD-pair separation distance. In contrast, HD-DOT uses a dense overlapping pattern of SD-pair measurements (Figure 4.1), with upwards of 1800 measurements, two orders of magnitude greater than most fNIRS systems. The HD-DOT SD-pair measurements have a mixture of short (13 mm), medium (30 mm), and long (40 mm) distances, which enable tomographic reconstructions to isolate the brain from scalp tissue, which can reduce scalp artifacts by $\sim 10\times$ [21]. In addition to sectioning, the dense imaging arrays provide improved resolution (volumetric PSF is $10\times$ better [15]). Perhaps most importantly, HD-DOT provides a consistent PSF that is translationally invariant, whereas the sparse fNIRS systems have PSF's that change with location under the imaging array. Notably, the newest HD-DOT field of view covers most of the cortical surface and does not need to be moved around the scalp to capture important regions (as some fNIRS systems do). Together these attributes enable HD-DOT to

perform functional neuroimaging tasks that fNIRS cannot accomplish including 1) retinotopic mapping of visual angle and eccentricity [15, 17, 20], 2) mapping hierarchical distributed language responses [20], and 3) mapping distributed functional networks such as the default mode network, and the dorsal attention networks [20]. Further, with co-registration to anatomy, HD-DOT can be tested and validated at the voxel level against fMRI, either at the single subject or group level.

Functional imaging methods without such limitations would allow us to better understand the impact of DBS on the functional connectivity of organized networks within the brain [130]. In this chapter, we overcome these significant limitations and apply HD-DOT methods to investigate how DBS modulates cortical functional networks and behavior in PD patients.

4.2 Methods

4.2.1 Subjects

DBS STN: 15 subjects with PD with already implanted and optimized DBS bilaterally in the STN were recruited from the DBS program within the Movement Disorders Clinic at WUSM. DBS STN patients were males or females between 50 and 70 years of age who met the criteria for clinically definite PD [142]. Participants were recruited at least 2 months after DBS has been implanted, and parameters have been clinically optimized. Patients have already passed clinical screening for neurological and psychiatric comorbidities, including dementia at our site. From this group, we also excluded those with clinically determined dementia manifesting after surgery, significant complications of surgery (e.g., stroke), inability to tolerate off medication or off DBS states, or any other condition which could interfere with testing (e.g., severe visual loss, non-English speaking, illiteracy).

Controls: 15 controls matched the age and sex distributions of the DBS groups. Exclusions included any significant past or current neurologic or psychiatric diagnosis or any other condition which could interfere with testing (e.g., severe visual loss, non-English speaking, and illiteracy) and contraindications for MRI.

4.2.2 Study design

To determine the ability of HD-DOT to measure the impact of DBS STN on within and between network FC, we scanned the normal controls and PD patients with DBS STN, respectively. Controls and PD patients were scanned with HD-DOT and assessed with cognitive, mood, and motor tests all on the same day.

We collected data from PD patients with HD-DOT with DBS on and off, order counterbalanced across subjects, after 12 hours of withdrawal of PD medications. After setting stimulators to the determined condition, a 45 min wait was enforced before testing or scanning begins. The purpose of this wait time was to reach a relatively steady state of clinical and behavioral symptoms [115]. This wait time is also consistent with previously collected behavioral and PET blood flow response data [144, 145]. For each condition, scanning consisted of visual, auditory, and resting state runs. Quantitative motor, cognitive, and mood testing were performed after the scan is completed and before changing the DBS conditions. Patients and testers were blind to DBS conditions. However, due to the visible nature of some symptoms, those present at the testing session were not completely unaware. The data were analyzed blind to group and DBS conditions.

Controls also underwent MRI/fMRI scanning. For the DBS groups, we used pre-surgical research quality MRIs, which are collected on most DBS patients. For controls, we obtained research MRI scans. The resting state fMRI data from controls were used to compare to the control HD-DOT

data. We did not do the same with the patient fMRI data since they were acquired many months to years prior to their HD-DOT data collection.

For each block, HD-DOT data were acquired during visual stimulation (block design with flickering left and right checkerboard, 5 min), auditory stimulation (block design with listening to words, 3.5 min), and 30 min of resting state (3x10 min blocks of fixating on a crosshair). The entire block took 45 min to perform (Figure 4.2). During scanning, movement was monitored with digital-video, eye tracking, and accelerometers. After scanning, kinematic, and Unified Parkinson Disease Rating Scale (UPDRS) assessments were also acquired.

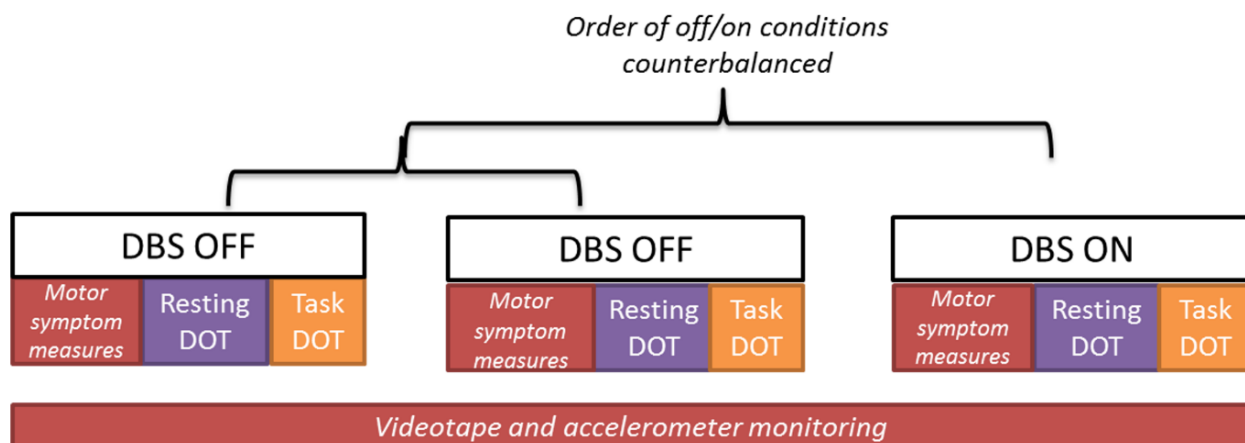


Figure 4.2 DOT-DBS study design. Each scan block takes 45 min, with a 45 min wait in between blocks. Resting and task runs will be interspersed within each block. Controls performed 3 blocks with the same measures (except for clinical motor ratings) and timing.

4.2.3 HD-DOT system

We have used a continuous-wave HD-DOT system with a wide field of view compared to other common fNIRS systems that enables mapping visual, auditory, default mode network, dorsal attention, and motor cortices [55]. Although our imaging cap does not cover all parts of the motor and frontal cortex, it has a large spatial resolution for the areas it covers compared to other fNIRS systems, and it enables 3D tomography and depth profiling in the brain. This HD-DOT system has

96 sources (LEDs, at both 750 and 850 nm) and 92 detectors (coupled to avalanche photodiodes, APDs) that are shining light to the head at multiple separations from the detectors (1.3, 3.0, 3.9, 4.7, and 5.1 cm for the first five nearest neighbor separations), which enable depth profiling (Figure 4.3C, D). The large number of overlapping measurements from each area of the brain increases the spatial resolution.

The first step of the scans is locating the imaging cap on the participant's head by combing the optodes through their hair to increase the optode-scalp coupling. Real-time in-house software was used to adjust or fix the poorly connected optodes.

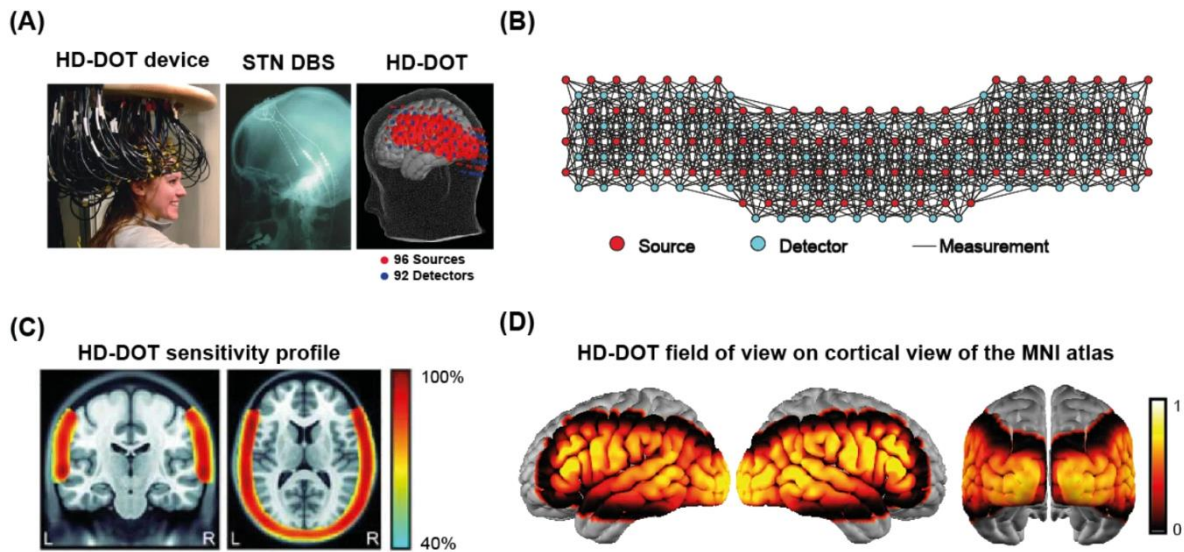


Figure 4.3 HD-DOT measurement array and field of view. (A) Adult HD-DOT cap structure illustrating the optical fibers, CT image of an implanted DBS STN in one PD subject, an overview of the sources and detectors on the head anatomy. (B) The flat distribution of the sources and detectors in the HD-DOT field of view. Black lines indicate source-detector (SD) pairs that have a standard deviation of less than 7.5%. (C) HD-DOT sensitivity profile. (D) HD-DOT field of view spatially registered on the cortical view of the MNI atlas.

4.2.4 Functional MRI (fMRI) system

fMRI data were collected on controls using a research-dedicated Siemens 3.0T Magnetom Prisma system (Siemens Medical Solutions, Erlangen, Germany) with an iPAT compatible 20-channel head coil. Blood Oxygenation Level Dependent (BOLD) sensitized fMRI data with TR = 1230 ms, TE = 33 ms, voxel resolution = 2.4 mm^3 , FA = 63 degrees, with a multi-band factor of 4 for both resting state functional connectivity MRI (3 runs each 10 min) and hearing words (1 run, 3.5 min) and visual (1 run, 5 min) tasks were acquired for all subjects. (i) a 3D MPRAGE (T1) sequence (TR=2500 ms, TI=1070 ms, TE=2.9 ms, FA=8°, 1.0 mm^3 voxels, *6:09-8:42 min); (ii) a T2-weighted sequence (TR=3200 ms, TE=564 ms, 1.0 mm^3 voxels, *4:42-6:51 min); (iii) a BOLD sensitized fMRI (TR=1230 ms, TE=33 ms, 2.4 mm^3 voxels, 11:10 min) for both task and resting state fMRI, and (iv) an asymmetric spin echo (ASE) field map (TR=6470 ms, TE=60 ms, 2.4 mm^3 voxels, 0:26 min). For T1 and T2 scans, short 3D echo-planar imaging volumetric navigators are embedded in a long 3D sequence, and the resulting image volumes are registered to provide an estimate of the subject's location in the scanner at the cost of less than 500 ms, ~ 1% change in contrast, and ~3% change in intensity. Minimum and maximum acquisition times are provided; actual times depend on the amount of motion correction required.

4.2.5 Paradigms (fMRI and HD-DOT)

Hearing words (HW): Subjects were seated for HD-DOT or supine for fMRI and instructed to fixate on a white crosshair against a gray background while listening to words. The HW task was administered as a block design. Each trial consisted of 15 seconds of hearing words followed by 15 seconds of silence. Each run included 6 trials.

Visual left and right checkerboards: Subjects were seated for HD-DOT or supine for fMRI and instructed to fixate on a white crosshair against a gray background while left and right visual stimuli were appearing in the lower left and lower right of their field of view [17]. The visual task

was also administered as a block design. Each trial consisted of 10 seconds of left or right visual checkerboard stimulation followed by 24 seconds of rest. Each run included 5 left and 5 right visual trials.

Resting state: Resting state data were collected over 10 min runs while subjects were seated for HD-DOT or supine for fMRI and visually fixating on a white crosshair against a gray background. Subjects were asked to stay awake and still during data acquisition.

4.2.6 Data processing

fMRI and HD-DOT data processing streams are harmonized as much as possible to facilitate direct comparisons.

4.2.6.1 HD-DOT pre-processing

All HD-DOT data were processed using the NeuroDOT toolbox following the flowchart in Figure A.1 [49, 94, 95]. HD-DOT light intensity measurement data were converted to log-ratio (using the temporal mean of a given SD-pair measurement as the relative baseline for that measurement). Noisy measurements were empirically defined as those with greater than 7.5% temporal standard deviation in the least noisy (lowest mean GVTD) 60 seconds of each run [45] and were excluded from further processing. Then the data were band-pass filtered (0.02-1 Hz cut-off for task-based datasets, 0.009-1 Hz for resting state datasets) to remove low-frequency drifts and high-frequency noise. To serve as an estimate of the global superficial signal, we computed the average of all remaining first nearest neighbor measurements (13 mm SD-pair separation). This global signal estimate was regressed from all measurements [21]. After that, all adult task-based data were low-pass filtered to 0.5 Hz cut-off to remove the cardiac oscillations [28, 46-48]. All resting state data were low-pass filtered to 0.08 Hz to remove the cardiac oscillations and to narrow the signal to the spontaneous, low-frequency fluctuations of the signal following the previous recommendations

for functional connectivity analysis in both adults and infants [49-52]. After bandpass filtering, following our motion detection optimization strategy using the global variance of the temporal derivative (GVTD) technique (explained in chapter 3), we excluded the time points (for resting state) and blocks (for hearing words and visual tasks) that passed a lenient motion threshold [29]. Following that, the time-courses were then down-sampled from 10 Hz to 1 Hz and then used for image reconstruction. Light modeling was computed using the subject-specific absorption models, details described in §2.5.6 and §4.2.8 [71]. Volumetric movies of relative changes in absorption at 750 nm and 850 nm were reconstructed after inverting the sensitivity matrix using Tikhonov regularization and spatially variant regularization [49]. Relative changes in hemoglobin concentration were obtained via a spectral decomposition of the absorption data, as previously described [49, 50].

4.2.6.2 fMRI pre-processing

fMRI pre-processing was performed using in-house 4dfp tools [96]: 1) correction for systematic slice-dependent time shifts; 2 elimination of odd-even slice intensity differences due to interleaved acquisition; 3) rigid-body realignment for head motion within and across runs; 4) normalization of signal intensity to a mode value of 1000. Signal intensity normalization enables identification of artifact by evaluation of the temporal signal derivative. Atlas transformation was computed by the composition of affine transforms derived by a sequence of coregistration of the fMRI volumes via the T2-weighted and MP-RAGE structural scans. Head motion correction and atlas transformation was applied in a single resampling step that generated volumetric time series in $(3\text{mm})^3$ atlas space. Data underwent spatial smoothing (6 mm full width at half maximum in each cardinal direction) and temporal band-pass filtering (0.02-0.5 Hz for the HW task and 0.009-0.08 for resting state). Nuisance regressors included six rigid body values derived from head motion correction, white

matter, and CSF signals and the mean whole-brain signal. Motion artifacts were reduced in resting state data through DVARS-based motion scrubbing using session-specific thresholding expressible as $g_{thresh} = \tilde{\kappa} + 2.5\sigma_L$ similar to the methods we developed for HD-DOT [97]. The fraction of censored frames was $21\% \pm 12\%$.

4.2.7 Motion and tremor censoring

We used GVTM for motion censoring by creating a temporal mask that excluded the time points above a motion threshold to provide a more reliable image series (Figure 4.5B). GVTM censoring increases the similarity of the HD-DOT with fMRI results by decreasing the false positives (Figure 3.9). In addition, wireless accelerometers (Yost labs 3-space sensor) on the cap were used to provide an independent measure of head motion (Figure 4.5A). We validated the GVTM-based motion censoring technique by comparing it with the accelerometer-based motion censoring and evaluating the quality of the resulting FC HD-DOT maps. While both are strongly correlated, GVTM is superior to the accelerometer in quantifying motion artifacts in the HD-DOT data since it directly measures the effects of motion on the data (Figure 3.4).

4.2.8 Subject-specific light modeling

To locate the cap on the head, we measured the distance between fiducials on the optode array and the head using an automated photometric approach. Anatomical landmarks based on the 10/20 international system (including nasion, inion, pre-auricular points, and Cz) were used for fiducials. To ensure adequate optode coupling across the cap, a display presented real-time readouts of the average light level in each optode and noise level of each source and detector pair. If either metric were poor (an optode with light level $<1\%$ of average values, or noise levels $>7.5\%$ cutoff), targeted individual fitting of the fibers is used to improve data fidelity. Measurements were acquired to a depth of 2 cm from the scalp (>1 cm into cortex) with a smooth sensitivity profile.

To generate an accurate model of light propagation in a subject's head, the shape and internal structure of the head and the placement of sources and detectors were estimated. The HD-DOT sensitivity for a given subject was modeled using head anatomy obtained from the subject's MRI or CT scan, according to §2.5.6 (Figure 4.4).

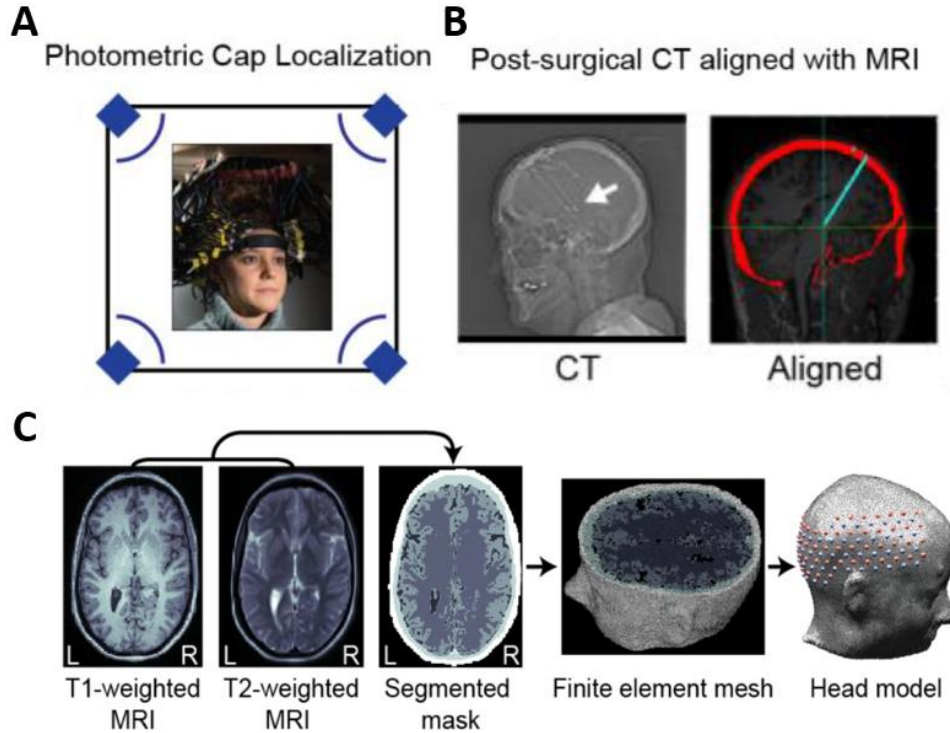


Figure 4.4: HD-DOT head modeling steps in DBS patients. (A) During the HD-DOT imaging session, a multi-camera system captures the location of fiducials on the head and the imaging array to generate a subject-specific light model. (B) Post-surgical CT images provide DBS location in the co-aligned MRI volume (cyan: DBS leads; red: skull). (C) Subject-specific head models of optical properties using MRI-based anatomy obtained before the DBS implantation.

4.2.9 Statistical analysis

4.2.9.1 Hearing words and visual task response mapping

The quantitative response magnitude was calculated with a standard general linear model (GLM).

The design matrix was constructed by convolving the experimental design with a canonical HRF using a two-gamma function fitted to the in-vivo HD-DOT data, as described in [98]. Extracted

hemodynamic response estimations for each subject were then combined in a simple group-level fixed effects analysis [99]. Fixed effect analysis was adopted as we expect the variance in our dataset to be most strongly driven by scan-to-scan variability rather than from subject-to-subject differences.

4.2.9.2 Seed-based correlation analysis of functional connectivity in resting state data

Seed regions were 5 mm radius spheres centered on coordinates used in our previous study [49].

Six seeds representing the auditory (AUD.), visual (VIS.), somatomotor (MOT.), dorsal attention network (DAN), and frontoparietal network (FPC), and default mode network (DMN) were selected within the HD-DOT field of view. Correlation maps were generated by calculating the Pearson correlation between the time-series of each seed region with all other voxels in the field of view. Correlation maps in individuals were Fisher's z-transformed and averaged across subjects.

4.2.9.3 Functional connectivity analysis

Resting state data from fMRI and HD-DOT were used to calculate correlational strength within and between resting state networks (RSNs). While there are several ways of calculating functional connectivity [146], here we used seed correlation approaches, commonly used in fMRI [147, 148] and fcDOT [58]. We calculated seed-based maps of FC by computing the zero-lag correlation between the time-courses of seed regions (5 mm radius spheres, placed in key regions for each network (explained in §4.2.9.3). Maps of Pearson-r correlations were generated separately for each subject and then transformed to Fisher's z maps before averaging across subjects. Similarly, seed-seed correlation matrices were generated by correlating the time-course of each seed to every other seed of interest. Group correlation matrices are generated by averaging across subjects. Resting-state FC was then compared between groups and conditions [137, 149].

4.2.10 Behavioral measurements

4.2.10.1 Motor measurements

The Unified Parkinson Disease Rating Scale III (**UPDRS motor subscale**) [150] was performed by a trained, validated, blinded rater and will be videotaped for quality control review. Kinematics measures were obtained using a wireless triaxial accelerometer/gyroscope (Wireless Motion Sensor, Great Lakes Neurotechnologies). Specific motor symptoms were measured before scanning (e.g., postural and action tremor, bradykinesia) and monitored during scanning. We assessed the movement speed during the UPDRS3 finger tapping, and hand rotation tasks using the gyroscope. The amplitude and frequency of any tremor was assessed using accelerometry measures [151-156].

4.2.10.2 Cognitive measurements

For characterization and screening purposes, PD patients were tested with the **Montreal Cognitive Assessment (MoCA)**; a brief screening instrument for mild cognitive dysfunction, those with scores < 22 were excluded, 10 min [157, 158]) and the **Wechsler Test of Adult Reading (WTAR)**, a measure of premorbid intellectual functioning, 5 min [159]).

4.3 Results

4.3.1 The effects of motion censoring on resting state FC mapping

Non-head motion. The subject motion may not always be captured by head movement parameters. To avoid the confound that symptoms (e.g., foot tremor) or other movements may have on brain activation analyses, we monitored movements in the rest of the body through direct observation, videotaping with subsequent review and time-synched to imaging. Through these methods, we identified the subjects that were having movements in different conditions and time points and

censored the imaging data as needed to avoid contaminated imaging findings. Eye movements were also monitored for wakefulness, which also lead to censoring data.

Head motion. Head motion induces artifact in most neuroimaging techniques, leading to lower signal-to-noise ratio and higher false-positive rates and has been rigorously addressed following motion detection and motion censoring methods presented in chapter 3 [30, 31, 100, 170]. **fMRI:** Data were subjected to frame censoring (“scrubbing”) based on the frame-to-frame DVARS measures [30]. fMRI runs with fewer than 30 uncensored frames were discarded. **HD-DOT:** In optical imaging, head motion changes the coupling of the optodes to the scalp and increases the variance across measurements and voxels time-traces. We used this property to identify the artifacts by setting a threshold on the global variance of the temporal derivative (GVTD) of the signals across the whole field of view. The large number of source-detector (SD) measurements in HD-DOT makes GVTD a fast and unique technique for motion detection. We used GVTD for motion censoring by creating a temporal mask that excluded the time points above a motion threshold to provide more reliable images (Figure 4.5C). GVTD-based censoring increases the similarity of the HD-DOT maps with fMRI by decreasing the false positives (Figure 3.8 and 3.9, 4.5E). In addition, wireless accelerometers (Yost labs 3-space sensor) on the cap were used to provide an independent measure of head motion. We validated the GVTD-based motion censoring technique by comparing it with the accelerometer-based motion censoring and evaluating the quality of the resulting functional HD-DOT maps. While both are strongly correlated, GVTD is shown to be superior to the accelerometer at quantifying motion artifacts in the HD-DOT data (Figure 3.4) since it directly measures the effect of motion on the data, and hence, we used GVTD for censoring the motion artifacts in this study.

HD-DOT correlation matrices for a group of 4 adults show significant improvements in the bilateral pattern in the functional connectivity matrix in the expected areas (black ovals) after GVTD censoring (Figure 4.5D). Example seed maps for default mode network (DMN), motor (Mot), and Visual (Vis) also show more localized connectivity with smaller false positives after censoring (Figure 4.5.E).

Overall, we had sufficient data that survived motion scrubbing for resting state analyses (DBS off = 338 of 460 min, 73%; DBS on = 350 of 690 min, 51%; Controls = 866 of 1130 min, 77%). These data suggested that we could acquire enough high-quality data in groups and conditions to perform reliable analyses. Task data yield lower percentage of high-quality data because data are excluded block-wise rather than frame-wise (DBS off = 29.2 of 135 min, 22%; DBS on = 27 of 173.5 min, 16%; Controls = 115.5 of 338 min, 34%).

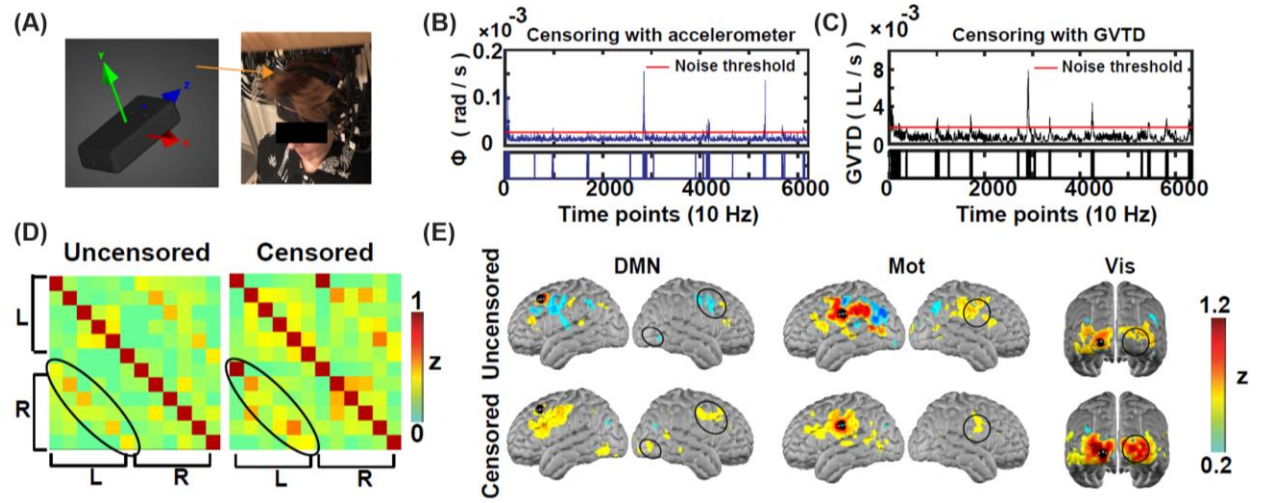


Figure 4.5: Effects of motion censoring on resting state FC HD-DOT data. Here we demonstrate the improvements when using a temporal mask based on the global variance of the temporal derivatives (GVTD). (A) Participant wears an HD-DOT cap with an accelerometer. (B) The head angular rotation (blue) time-trace is highly correlated with the (C) GVTD (black) time-trace. GVTD censoring excludes the time points that pass the noise threshold (red line). (D) HD-DOT correlation matrices for the seed locations show significant improvements in the bilateral pattern in the functional connectivity matrix in the expected areas (black ovals) after GVTD censoring. (E) Seed maps for default mode network (DMN), motor (Mot), and Visual (Vis) are shown before and after censoring.

Another example of the effect of motion censoring in HD-DOT data is an increase in the similarity of the HD-DOT FC maps to those of fMRI (Figure 3.9). Here, we show the FC seed maps from Figure 3.9 before and after GVTD-based motion censoring (Figure 4.6), to emphasize the importance of performing motion censoring for the PD DBS resting state FC analysis using HD-DOT [29].

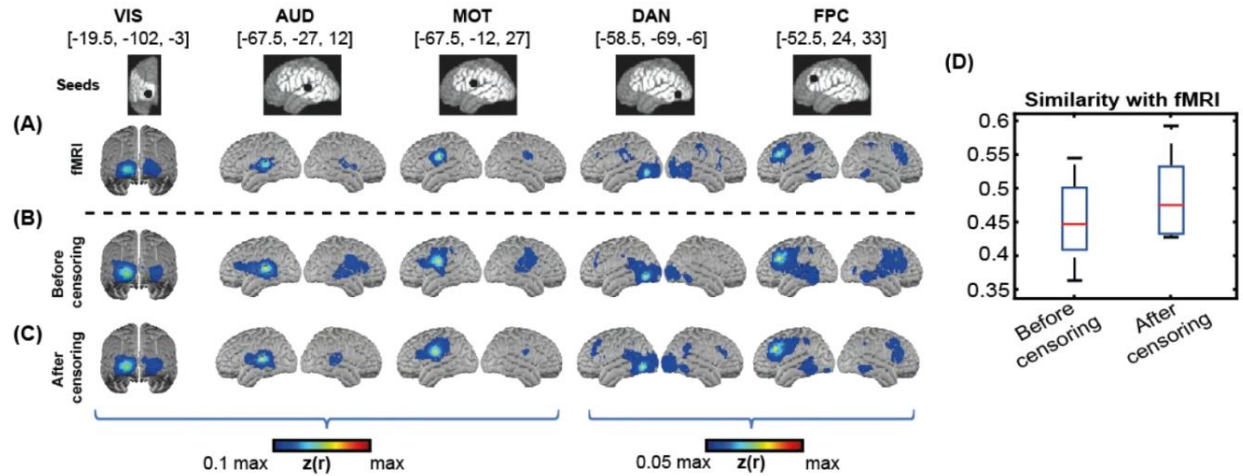


Figure 4.6: Motion censoring increases the similarity of HD-DOT FC maps to fMRI. Five columns represent the seed maps for visual (VIS), auditory (AUD), somatomotor (MOT), dorsal attention (DAN), and frontoparietal (FPC) networks. (A) fMRI maps based on 8 subjects. HD-DOT maps (B) before motion censoring. (C) after motion censoring, (D) Spatial similarity was computed as the Fisher's z-transformed spatial correlation between the HD-DOT and fMRI FC maps, evaluated over the HD-DOT field of view. The similarity of HD-DOT results with fMRI increases after motion censoring.

4.3.2 Cross-modality comparison in mapping single subject task activations

Using subject-specific light modeling and motion censoring, we were able to perform more reliable single subject mapping using HD-DOT. Here is an example of mapping a single subject hearing words and visual activations for a control and a PD subject with DBS STN. The maps for the control subject match the ones for the same subject using fMRI.

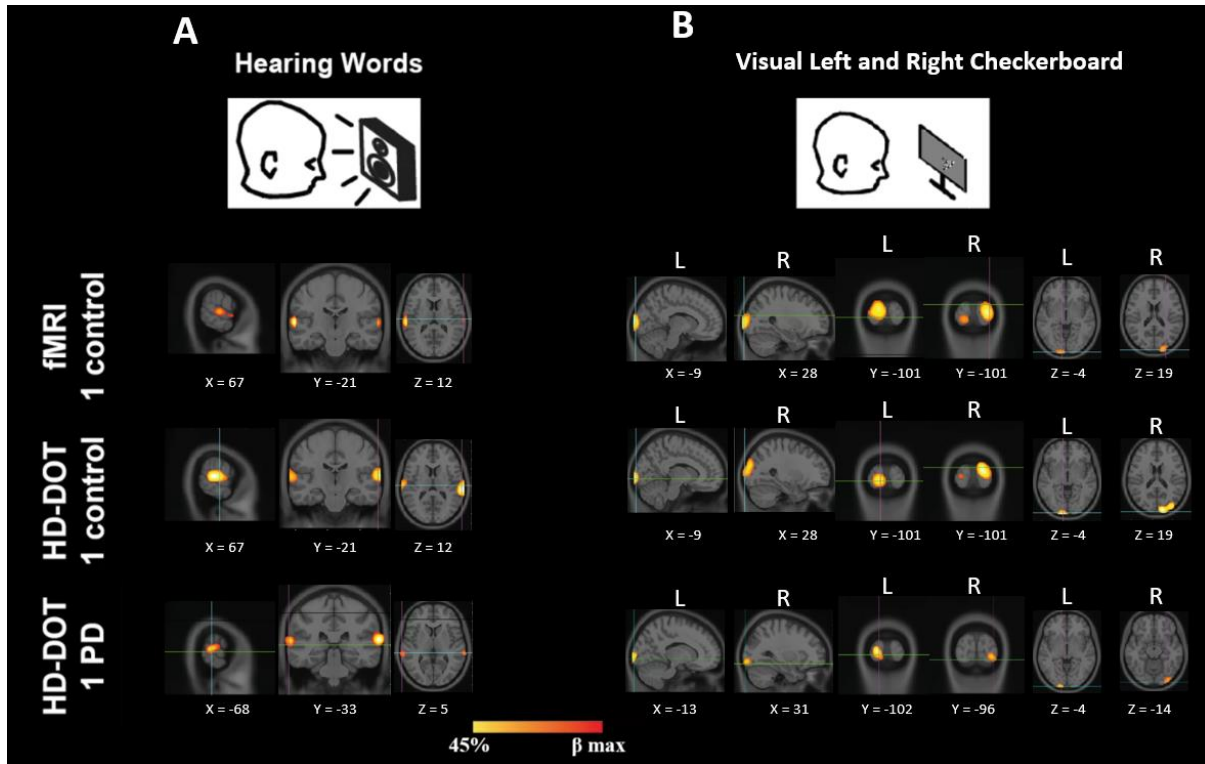


Figure 4.7: More reliable HD-DOT single subject maps using subject-specific light models. (A) Hearing words and (B) left and right visual checkerboard activation maps for a control using fMRI (first row) and HD-DOT (second row). The same sagittal, coronal, and transverse slices were chosen for fMRI vs. HD-DOT. The same maps are shown for a PD subject with DBS STN.

4.3.3 Mapping auditory and visual task activations

We validated the feasibility of imaging people with DBS STN and older controls with both hearing words and visual tasks (Figure 4.8). We show the fMRI gold standard maps collected only for the control group, and the HD-DOT maps collected for both control and PD groups evoked anatomically appropriate patterns in all groups (Figure 4.8), consistent with our previous studies. These results successfully show HD-DOT's image acquisition, data quality assessment methodology, and data processing ability in mapping cortical activations to well-known tasks.

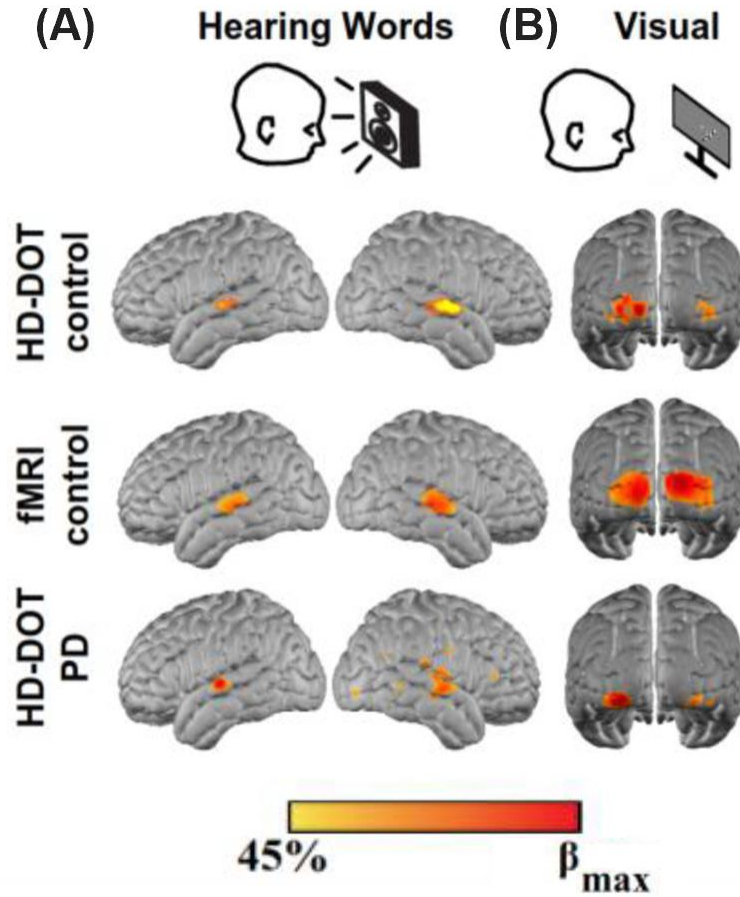


Figure 4.8: Task responses in controls with HD-DOT and fMRI and in PD with HD-DOT. (A) Hearing words vs. rest, (B) right and left side checkerboards vs. rest.

4.3.4 Mapping resting state FC

We also validated the presented data quality measures in chapter 3 in resting state results from older controls and PD subjects. Figure 4.9 shows resting state seed maps (explained in §4.2.9.2) and FC matrices (explained in §4.2.9.3) for matched fMRI/HD-DOT data for controls and only HD-DOT for PD subjects. In the next sections, we assess the between-group differences for controls and PD with DBS.

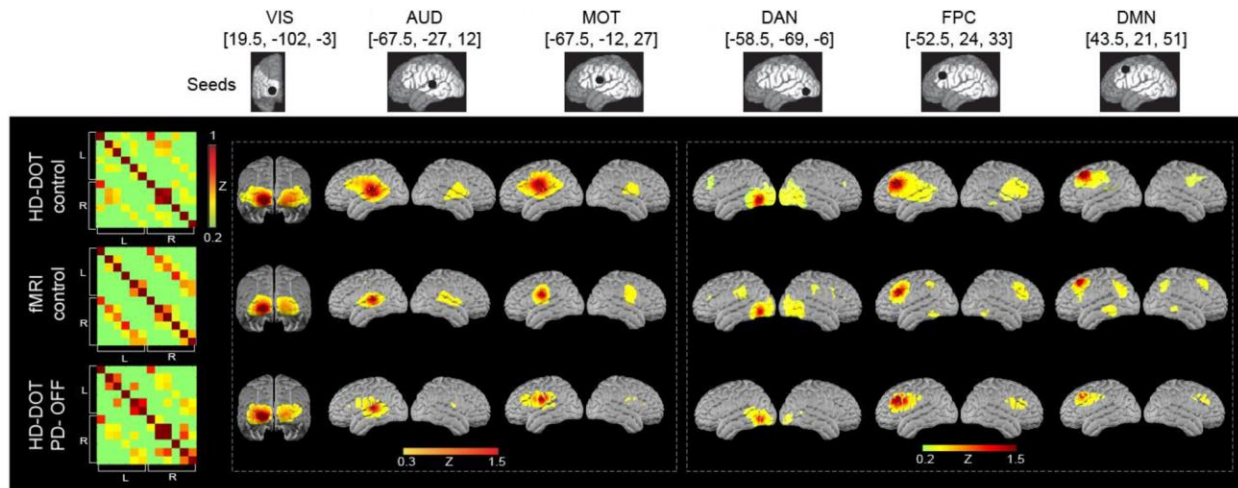


Figure 4.9: Resting state FC in controls with HD-DOT and fMRI and in PD with HD-DOT. (VIS-visual; AUD-auditory; MOT-motor; DAN-Dorsal Attention; FPC-Frontal Parietal; DMN-Default Mode. Black disks: anatomical location of each seed.

4.3.5 DBS STN within and between network FC

We assessed the between-group differences by defining a larger seed set in each of the visual, auditory, somatomotor, DMN, and FPC networks. Our results show that PD subjects with DBS off had reduced within network FC in somatomotor, visual, and auditory RSNs and between network FC with somatomotor and auditory RSNs, as found by Gratton et al., [31] (Figure 4.10, top row). We also observed that somatomotor to FPC network connectivity was greater in PD than controls. Finally, turning DBS on, appears to alter FC within and between network connectivity for somatomotor, auditory, DMN, and other RSNs (Figure 4.10, bottom row). Interestingly, the region identified as having decreased blood flow in our activation study (explained in §4.3.6 and Figure 4.11) was included in the somatomotor (SM) seed set (Figure 4.10; red arrow); DBS decreased FC in this region. Importantly, we have not applied any statistical tests to these comparisons, due to our limited sample size and so cannot definitively interpret these patterns.

With the data that will be collected in the next phase of this study, however, we will be able to confirm or rule out these initial observations and test our explicit hypotheses.

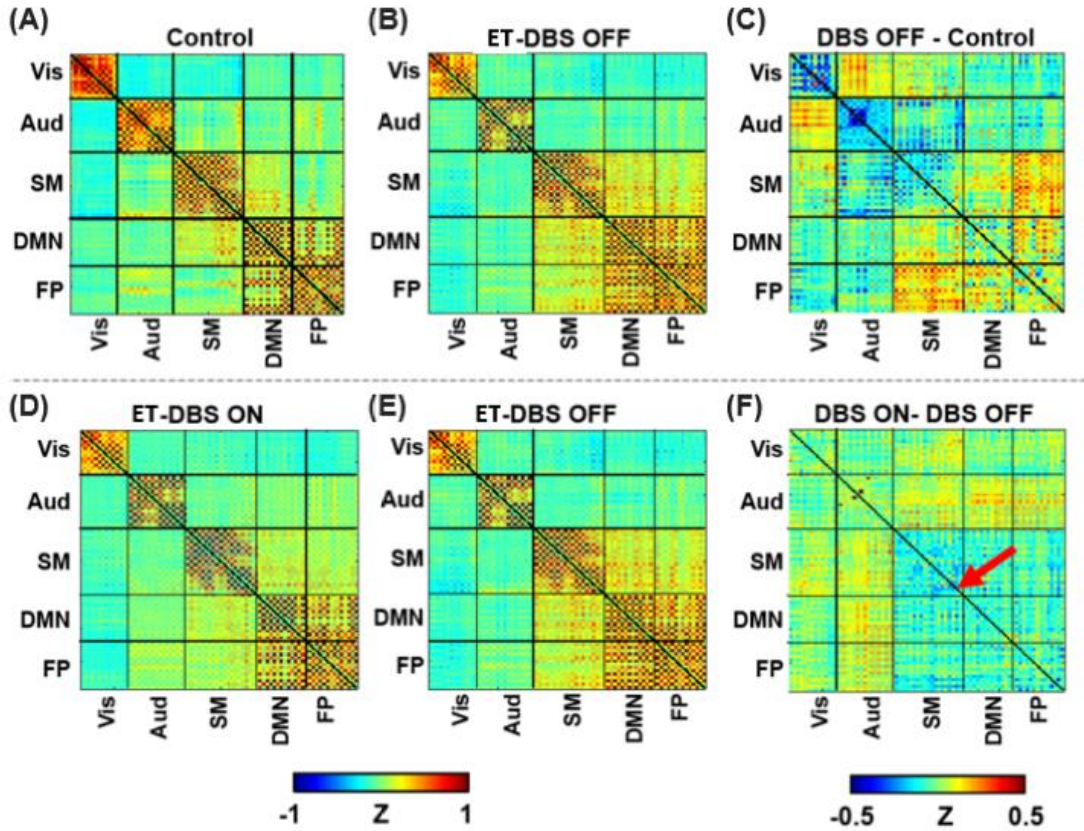


Figure 4.10: Within and between network FC differences in PD DBS using HD-DOT. FC Matrices for groups, conditions, and differences. Diagonal boxes indicate within network FC, off-diagonals are between network FCs. Brighter colors indicate higher correlations between seeds in networks. (A) Controls; (B) PD (DBS off). (C) Difference between PD and Controls. Blue indicates seeds that have lower FC in PD than in controls; Red/yellow indicates seeds that have higher FC in PD than controls. (D) PD DBS on; (E) PD DBS off (repeated to aid visual comparison); (F) Difference between DBS on and off. Blue indicates seeds that have lower FC in DBS on than in off; Red/yellow indicates seeds that have higher FC in DBS on than in off. The red arrow indicates the region in the SM network identified as having decreased blood flow in our activation study (explained in §4.3.6).

4.3.6 DBS STN activation

In order to demonstrate HD-DOT's ability to detect cortical activations induced by DBS STN, we scanned 14 DBS STN patients with HD-DOT while their DBS was turned on and off in a classic block design, similar to the Min et al. paper [171]. To make the testing maximally tolerable for

these patients, they watched a 10 min movie during the study, medications were not withdrawn, and the left DBS was in the on condition throughout. The right DBS was turned on and off repeatedly ($n = 22$) in the following pattern: 8-sec ramp up, 18 sec on, 16-24 sec off (off period randomly jittered between 16 and 24 sec (Figure 4.11A). Clinically optimized settings were used for the on conditions. Data were compared to a set of 5 healthy adult controls who were also scanned watching the same movie clip for the same amount of time. Data were censored for movement detected with the overlap of the temporal masks made by 1) accelerometers on the HD-DOT cap, 2) observations of the full-body video, and 3) GVTD-based motion censoring. On/off blocks were compared within 5 DBS STN patients with no overt symptoms in the on or off states, and identical time-frames were compared in Controls. Results (Figure 4.11) show that DBS decreased oxygenated hemoglobin in the right primary motor cortex in patients.

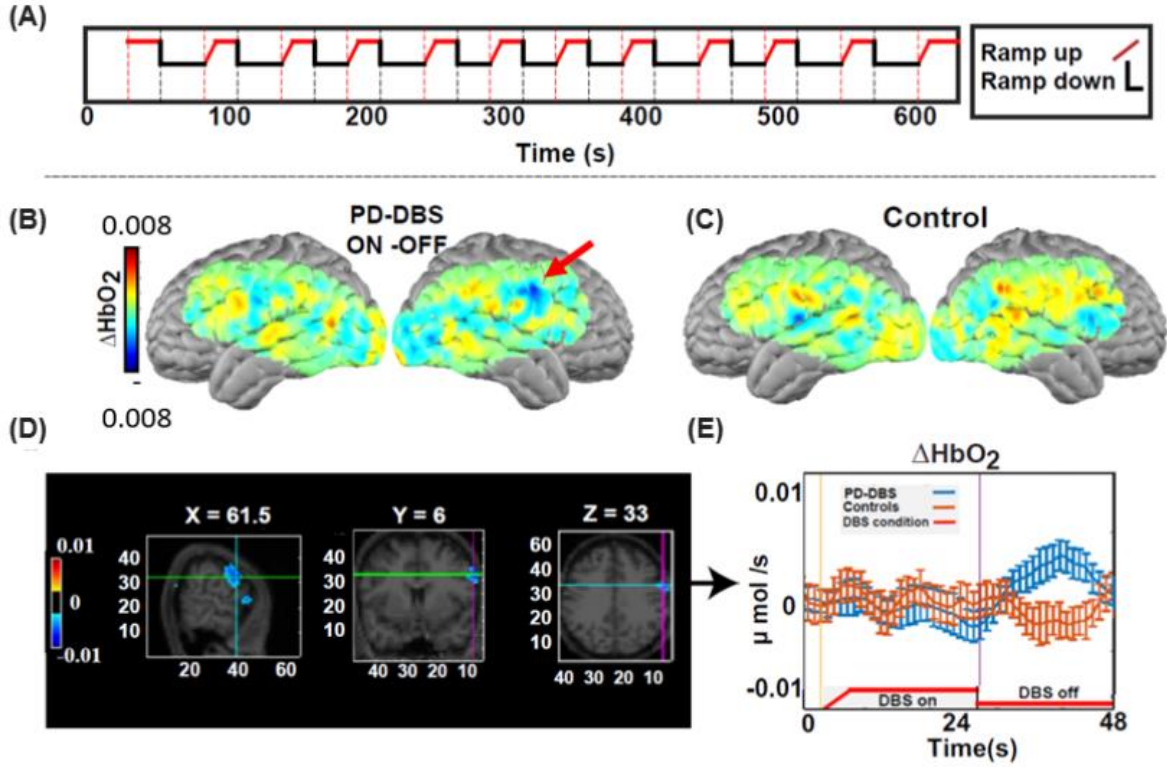


Figure 4.11: DBS activation study. HD-DOT-measured cortical response to block design right DBS (A) in 5 patients (B) compared to 5 control subjects analyzed similarly (C; no DBS). A direct comparison of groups isolated the region (D). (E) Time-courses from the region show decreased oxygenated hemoglobin in on vs. off DBS, whereas controls remain stable.

The low survival rate of this group is mainly due to the tremor during the DBS off periods and short adjustment times for the patients (< 30 s). We performed a variance analysis on the on minus off maps for the patients with no tremor (Figure 4.12A) and the same on minus off maps for the subjects with tremor (Figure 4.12B) and found that although the tremor group data passed the common motion censoring using GVTD, the tremor caused a very high spatial variance across the field of view and therefore, we excluded those subjects from the final group analysis. Further investigation of the effect of tremors is needed when a larger sample size is available.

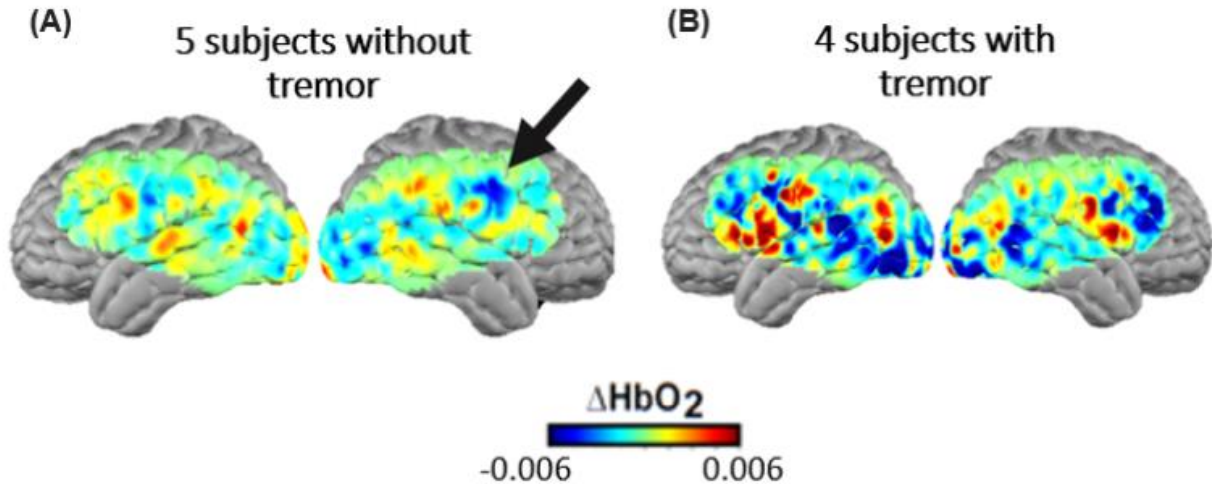


Figure 4.12: Increased spatial variance in HD-DOT maps in PD DBS with tremor. HD-DOT-measured cortical response to block design right DBS for on blocks minus off blocks (A) in 5 patients with no tremor compared to (B) 4 patients with tremor, shows the importance of both tremor and motion tracking in data processing of PD patients.

4.4 Discussion

4.4.1 Regional cortical effects of DBS STN

DBS STN affects cortical function in a clinically significant and anatomically plausible manner in PD and ET. DBS STN-induced changes in regional cerebral blood flow (rCBF) have been measured with PET by our collaborators and others [119, 145, 172-176]. This approach assumes that changes in rCBF reflect changes in neuronal activity [177-181] in target synaptic fields, including local interneurons [177-179, 182, 183]. A previous PET study found that DBS STN decreases blood flow in cortical regions downstream from the site of stimulation [130, 145]. In addition, the degree of DBS STN-induced cortical blood flow changes correlated with the degree of motor benefit or cognitive impairment induced by DBS [119, 172]. However, the behavior is known to be mediated by dynamic brain networks, not single, static regions, so these analyses likely provide an incomplete view of the brain's dynamic and integrated response to DBS. Recent reviews have emphasized the idea that DBS profoundly alters dynamics between distributed

interconnected cortical brain networks [116, 130-132]. Based on evidence from EEG, limited fMRI, and animal studies [131, 184-187], it has been suggested that a primary mechanism of DBS STN's effects may be to modulate or interfere with functional relationships in downstream cortical regions, driving behavioral responses [130].

4.4.2 Mapping cortical networks in PD

Previous studies have described resting glucose metabolism patterns measured with PET, that distinguish groups, change with DBS, or that correlate with cognitive or motor impairment [174-176, 188]. This approach has been useful but is limited in terms of its temporal resolution (each scan lasts several hours), the ability to assess FC, and the ability to easily investigate multiple conditions (e.g., DBS settings) in an individual due to radiation exposure and time constraints. Resting state functional connectivity using fMRI, a more flexible methodology free of these limitations, is sensitive to the intrinsic spontaneous neural activity correlated on a time scale of tens of seconds (frequencies below 0.1 Hz) within constellations of regions distributed over widely separated parts of the brain. The corresponding topographic patterns are known as resting state networks (RSNs) and can be measured in the cortex equally well via fMRI BOLD or by HD-DOT [20, 55, 58, 135].

The measurement of RSNs within disease states and in response to treatments has led to profound insights into the neuropathophysiology underlying behavioral symptoms [189-193]. In PD, results from past studies have been varied, likely due to between-subject clinical heterogeneity, small samples, and limited motion control [194]. However, a recent comprehensive examination of RSN abnormalities in PD applied cutting-edge and converging analysis techniques and rigorous quality control measures to a large sample of non-demented PD patients, scanned while off medications, and controls. Analyses revealed reduced between-network FC involving predominantly cortical

RSNs (somatomotor, visual, auditory, salience, and frontoparietal) and reduced within-network FC in predominantly somatomotor, visual, auditory, thalamic, and cerebellar networks [31]. Some of these effects correlated with cognitive and motor dysfunction in PD. Notably, although there were some differences in subcortical-cortical FC, most of the largest differences were found in the cortex; striatal RSNs were not abnormal [31]. Others have suggested that the abnormality of functional networks measured before DBS electrodes are implanted can predict the clinical response patients experience to DBS [128, 131]. These studies suggest the importance of functional networks in PD and DBS responses but do not explore DBS-induced change within and between FC networks.

4.4.3 Cortical networks in DBS STN

Several groups have attempted to measure DBS-induced changes in FC using fMRI in small samples of DBS subjects on a low strength magnet (1.5T) [187, 195-197]. The largest of these 1.5T studies had 13 patients and found that DBS STN increased FC between the left and right motor cortex and between the motor cortex and thalamus and cerebellum [187]. However, data were collected only 1-3 days post-surgery and so could be confounded by microlesion or other surgical effects. In addition, significant signal artifact around the wires and electrodes limited analyses. Another study reported preliminary safety data from 3T fMRI [129]. Although no adverse events occurred and there was no evidence of heating at the tip of the electrode, the authors concluded that there was “significant artifact” from the electrode leads that impacted functional data quality and that more extensive testing for safety would be needed before this method could be recommended [129, 198, 199]. Finally, one study on sedated pigs implanted with DBS STN electrodes used fMRI to measure the impact of short bursts of unilateral DBS STN in a quasi-event-related design (repeating trials of 6s DBS on, 120s DBS off). For the hemodynamic response

to DBS on, they found increased BOLD response in many ipsilateral cortical regions (somatomotor, prefrontal) and contralateral temporal cortex, but they did not perform functional network analyses [171]. Thus, despite strong interest in applying fMRI to these questions, we are currently unable to use it safely and effectively to measure DBS-influenced network properties in humans.

Therefore, as we discussed in this chapter, HD-DOT could be used as a surrogate to fMRI in the PD DBS population for answering all these questions in a safe and artifact-free environment.

Our results (Figure 4.10) in this chapter show that DBS decreased oxygenated hemoglobin in the right primary motor cortex in patients, similar to the previous PET study and in the same region (although opposite direction) of the sedated pig study [171] (Notably, anesthesia is known to reverse regional blood flow effects of pharmacological challenges [200]). The corresponding area in controls did not change. These new results suggest that HD-DOT can detect the expected regional decrease in blood oxygenation predicted by PET blood flow imaging, which is consistent with the known neurophysiology of STN-thalamocortical pathways.

We showed that DBS STN affects cortical blood flow/hemodynamics using HD-DOT and cognitive function [119, 145, 201], provided extensive and varied data on the validity and feasibility of HD-DOT for measuring resting state FC and task-induced responses in controls and PD patients with implanted DBS STN in different DBS conditions [20, 55, 136, 202]. Our preliminary data suggest that HD-DOT can capture the reduced within and between network cortical FC in PD, and their response to DBS STN, and the fact that the utility of our movement monitoring and correction procedures for HD-DOT analyses are valid.

4.4.4 Limitations and future directions

HD-DOT cannot measure subcortical or cerebellar activity. However, recent fMRI work in PD suggests that cortical RSNs downstream from subcortical pathology are the most prominently affected compared to controls [31]. Future studies could consider combining HD-DOT with PET for complementary subcortical blood flow or pre-surgical recording from the STN and cortical functional connectivity responses to DBS. Furthermore, whole-brain fMRI data on PD subjects (pre-surgically) could allow inferring the subcortical nodes that are most related to RSNs affected by DBS conditions.

Our overarching goal in this project is to define the cortical functional network signature of DBS STN and its relationship to behavior. Results could help shape new optimization procedures for DBS STN parameters, possibly identify cortical targets for less invasive neuromodulation (e.g., transcranial magnetic stimulation, TMS) [128, 131] and reveal fundamental properties of cortical network plasticity in response to up-stream perturbations [203]. Future investigations could leverage this groundwork, identifying unique vs. overlapping DBS-induced network using varying DBS STN parameters (e.g., contact, voltage, frequency, pulse width) or DBS locations (e.g., globus pallidus internus), or in other movement disorders (e.g., essential tremor, dystonia), or over longer-term plasticity (e.g., slow clinical response to DBS for dystonia). In addition, HD-DOT could be combined with methods that reflect different aspects of neurophysiology (e.g., PET, microelectrode recording) to explore neurobiological properties driving cortical hemodynamics (e.g., firing patterns of STN neurons, subcortical changes in blood flow, or glucose metabolism) or with other forms of stimulation (e.g., TMS; tDCS). Finally, with continuing advances in wearability, portability, and automation, HD-DOT could be integrated into clinical programming procedures as an objective biomarker of outcomes, allowing for faster and more objective optimization of DBS settings.

4.5 Conclusion

In summary, in this chapter, I applied the data quality assessment measures presented in chapter 3 on a high-motion clinical population with DBS implants. We not only mapped the evoked responses in these subjects' brains during the well-known auditory and visual tasks but also validated the efficacy of our newly developed data quality and motion censoring methods by finding agreements between the results obtained using HD-DOT with the ones reported in previous fMRI and PET studies with similar experimental designs [31]. We conclude that HD-DOT's data processing pipeline is now more equipped to produce clinically important and physiologically meaningful results in patients with DBS implants with high-motion levels.

Chapter 5: Mapping Neural Mechanisms

Underlying Speech Perception in Listeners

with Cochlear Implants Using HD-DOT³

5.1 Introduction

The neural correlates underlying the perception of the spoken language has been investigated in normal-hearing adults mainly using positron emission tomography (PET) [204], functional magnetic resonance imaging (fMRI), and electrocorticography (ECoG). However, the organization of cortical language networks in listeners with cochlear implants (CIs) with tremendous variability in speech understanding is unknown because the current gold standard neuroimaging tools are limiting for this population [37, 205].

Cochlear implants compensate for the dysfunction in the cochlea by stimulating the auditory nerve and enabling their users to perceive sounds [32, 33]. However, due to the crosstalk between the CI electrodes, there is a lack of spatial selectivity in the internal representation of the sound frequency content [34, 35]. This distortion of the sound contributes to the tremendous variability in how well listeners with CIs understand the spoken speech [36, 37].

Multiple studies have shown that acoustically degraded speech in normal-hearing adults increases cognitive demand [206-208], which contributes to increased listening effort [206]. Thus, in the CI users with a degraded sound quality similar phenomenon might occur. However, studying the neural organization of the CI listeners have been limited by contraindications of these metal implants with the MRI magnet and the artifacts due to their electrical stimulation in EEG and MEG.

³ A version of this chapter is being prepared for submission in a peer-reviewed journal.

Functional near-infrared spectroscopy (fNIRS) provides a quiet, non-invasive, and compatible tool with metal implants for measuring the cortical neuronal activity during various naturalistic settings and listening scenarios [9, 10, 209-218]. However, one of the main limitations of the standard fNIRS imaging is its low spatial resolution and small field of view. Recent progress in the HD-DOT instrumentation with hundreds of sources and detectors overcomes these two limitations and enables a tremendous increase in the spatial resolution and field of view for simultaneously mapping the neuronal activity in multiple cortical areas [49, 219, 220]. In this study, we have used an HD-DOT system that covers parts of the auditory, occipital, motor, and frontal areas. This device has been validated in multiple studies by our lab in successfully mapping the cortical activity during hierarchical language paradigms and naturalistic stimuli in control adults [22, 49, 98, 220-222].

The goal of this chapter is to assess the degree of auditory activation in listeners with CIs compared to normal hearing individuals and to determine the extent to which regions beyond auditory regions are recruited for speech perception in the CI user group.

To this goal, we mapped the neural mechanisms underlying speech perception in a group of 18 CI listeners and 18 age and gender equivalent controls using our HD-DOT device with 96 sources and 92 detectors [20]. We used a variety of speech paradigms, including single words, noise-vocoded speech, sentences, and audiovisual movie stimulus, and performed region of interest (ROI)-based statistical analysis across the control and CI group for quantifying the between-cohort differences. Based on our preliminary observations, we selected the left and right auditory and the left dorsolateral prefrontal cortex (DLPFC) as our ROIs. We localized the DLPFC ROI using an independent non-auditory spatial working memory task in a subset of the subjects. We also used a

separate resting state fMRI dataset to define the left and right auditory ROIs by performing a seed-based analysis on that dataset.

Our results showed that right-ear CI users had decreased activation in their left and right auditory cortex, and they also recruited their left DLPFC during speech perception. Our study provides supporting evidence following the hypothesis that compensatory mechanisms in the frontal cortex are needed to understand the degraded acoustic signal in the CI users [206, 208, 223].

5.2 Methods

5.2.1 Dataset

We compared brain activity in 18 CI patients (age 58.42 ± 12.41 y, 11f) with a group of 18 age and sex equivalent controls (age 54.77 ± 13.06 y, 11f). Patients all had unilateral right-side CI, and controls had normal hearing. The right-side CI users were selected to avoid blocking the optodes by the CI's external transducer on the left side; based on the previous studies, the left hemisphere is more dominantly active during language processing. These CI listeners either had normal hearing in their left ear or were using their hearing aid during the scan. All aspects of these studies were approved by the Human Research Protection Office of the Washington University School of Medicine. All adult participants were right-handed or ambidexter native English speakers and reported no history of neurological or psychiatric disorders. Adults were recruited from the Washington University campus and the surrounding community (IRB 201101896, IRB 201709126). All subjects gave informed consent and were compensated for their participation in accordance with institutional and national guidelines.

5.2.2 HD-DOT system

Data were collected using a previously described continuous-wave HD-DOT system comprising 96 sources (LEDs, at both 750 and 850 nm) and 92 detectors (coupled to avalanche photodiodes,

APDs, Hamamatsu C5460-01) to enable oxy- and deoxyhemoglobin spectroscopy [49]. The design of this HD-DOT cap provides more than 1200 usable source-detector pair measurements at a 10 Hz full-field frame rate that covers parts of the auditory, occipital, motor, and frontal areas (Figure 5.1). This HD-DOT system has been validated for successfully mapping the brain's response to hierarchical language paradigms and naturalistic stimuli with comparable sensitivity and specificity to fMRI [22, 49, 220].

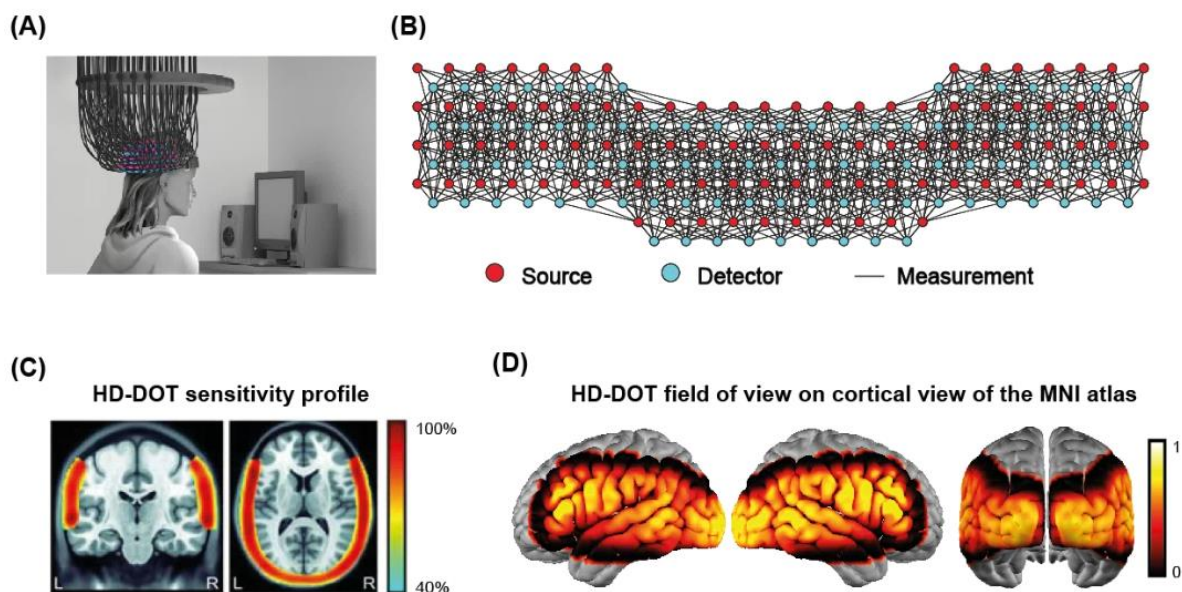


Figure 5.1: Schematic of the HD-DOT measurement array and field of view. (A) A participant is wearing the HD-DOT cap. (B) Regional distribution of SD-pair measurements (~1200 pairs) are illustrated as solid black lines between sources and detectors in a flat view of the HD-DOT cap. (C) HD-DOT sensitivity profile. (D) HD-DOT field of view spatially registered on the cortical view of the MNI atlas.

5.2.3 Experimental design

Subjects were seated on a comfortable chair in an acoustically isolated room facing a 20-inch LCD screen located 76 cm from them, approximately at their eye level. The HD-DOT cap was located on the subject's head in a process that maximized the coupling of the optodes to their scalp via real-time coupling coefficient readouts using in-house software (Figure 5.1A). The stimuli were

presented using the Psychophysics Toolbox 3 package for MATLAB (2010b) [224]. The auditory stimuli were presented through two speakers located around 150 cm from the subjects' ear level (sound level fixed at 60dB). Subjects were instructed to fixate on a white crosshair against a gray background while listening to the auditory stimuli, holding a keyboard on their lap for the stimuli that required their response. Our experimental design (Figure 5.2A) included a hierarchy of speech paradigms including single words (Figure 5.2B), noise-vocoded speech and short sentences (Figure 5.2C), and a movie watching task (Figure 5.2D), to examine the reliability of the findings through different experimental designs. We also performed a spatial working memory task in a subset of the subjects to localize the DLPFC ROI (Figure 5.2E). Following each neuroimaging session, the participants underwent an audiometric, speech, and cognitive measurements off the HD-DOT scanner.

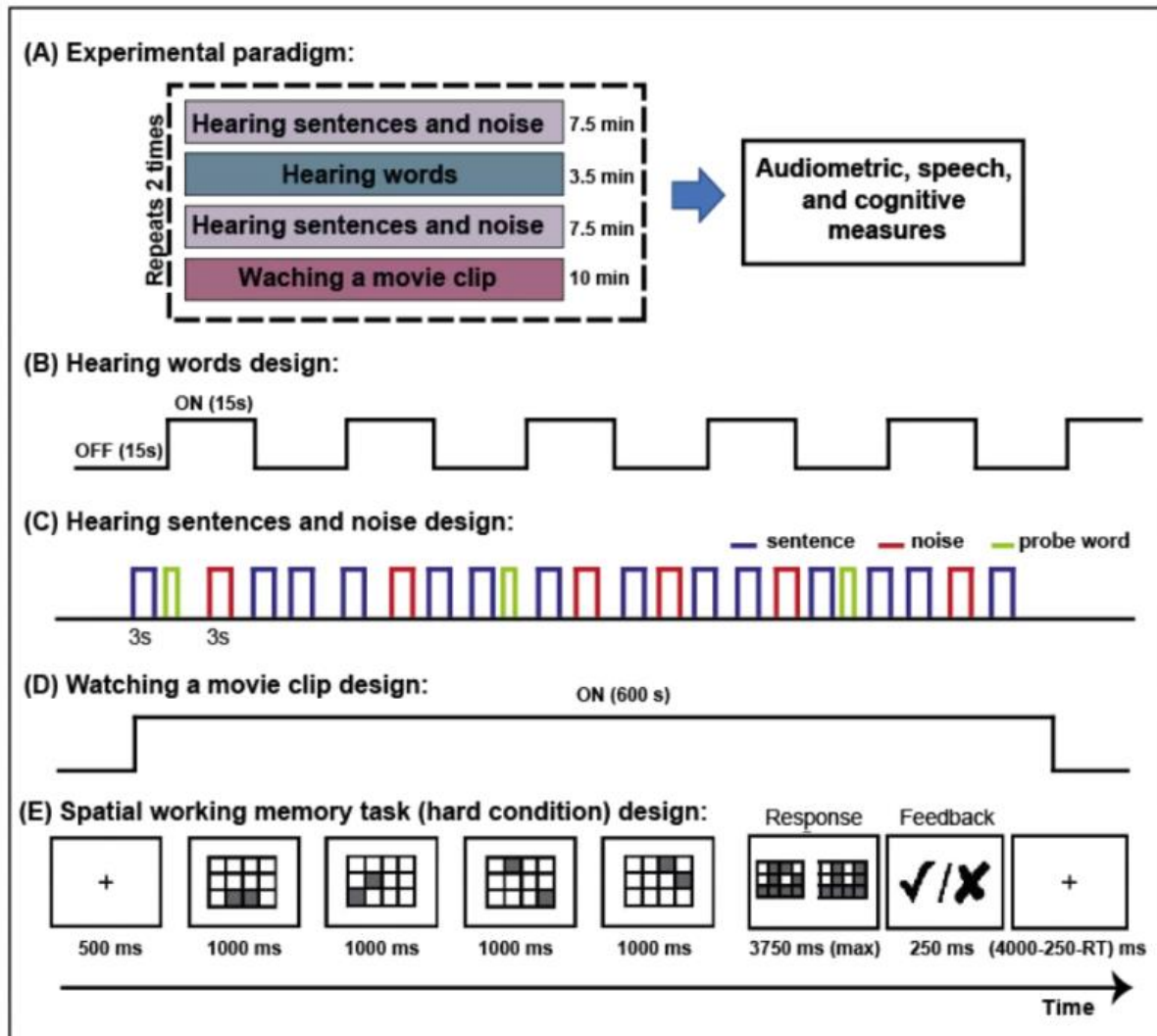


Figure 5.2: CI-DOT study design. A schematic illustration of (A) the study design and the four tasks used in this study. (B) Block design hearing words task, (C) event-related sentence and noise task (inter-stimulus interval: between 5-11 sec), (D) a 10 min movie clip from “The good, The bad, and The ugly”, and (E) a spatial working memory task adopted from reference, Federenko et al., 2013.

5.2.4 Paradigms

5.2.4.1 Hearing words

The hearing words paradigm consisted of data acquisition runs that included six hearing words blocks. Each block consisted of 15 seconds of hearing words (with a frequency of one word per

second), followed by 15 seconds of silence. Two hearing words runs were performed in each study session (a total of 180 words in about 6 minutes, Figure 5.2B).

5.2.4.2 Sentences and noise

The speech and noise run included 40 AzBio sentences (set of sentences designed for speech perception evaluation in hearing-impaired listeners) [225]. Eight of the sentences were followed by a visual probe word. Listeners were instructed to press a key if the probe word was semantically related to the last sentence presented.

This paradigm also included 20 unintelligible speech (noise) trials. The noise stimuli consisted of one channel noise-vocoded speech created by modulating white noise (low pass filtered at 8 kHz) with the amplitude envelope of a subset of AzBio sentence (low pass filtered at 30 Hz). Noise vocoding removes the spectral detail from the sentence while retaining its temporal amplitude envelope [226]. The mean length of auditory stimuli (sentence or noise) was 2.03 ± 0.51 s (range: 1.03 -3.44s). Each sentence and noise run took around 7 min, and each participant performed 4 runs (a total of 280 short sentences, 80 noise, and 32 probe words, 30 min total, Figure 5.2C). Prior to the data collection session, we presented a short practice session containing 12 trials (4 noise and 8 sentences, 2 followed by a probe word) to train the individuals for performing this task [227].

5.2.4.3 Movie watching

Naturalistic movie viewing engages multiple cortical processing systems such as lower-order auditory and visual processes and higher-order narrative content that recapitulates real-life sensory processing. Especially for the CI recipients, passive movie viewing is a scenario of a more realistic cognitive effort, including an audiovisual stimulus. The combination of mapping the synchronous brain activity during movie stimuli and HD-DOT has been studied in a recent paper using the same HD-DOT device [220]. We adopted the same movie paradigm for both CI recipients and age-

equivalent controls. For this task, we asked the participants to sit still and watch a 10 min clip from the “The good, The bad, and the ugly” movie while their brain hemodynamic activity was being recorded with the HD-DOT system (Figure 5.2D).

5.2.4.4 Spatial working memory

Spatial working memory stimulus was used in one CI user in four different scanning sessions after patterns of the engagement of the frontal cortex has emerged in our preliminary results. For this mean, we adopted the spatial working memory task introduced in a previous study [228, 229] in the one CI user across four different sessions. In this spatial working memory task, the subject was asked to remember four or eight flashing locations in a 3×4 grid in easy and hard conditions, respectively. Following each trial, participants had to choose the pattern they saw among 2-choice grids, one with correct and one with incorrect locations (Figure 5.2E). This task requires keeping sequences of elements in memory for a brief period, and it was shown that it activates parts of the dorsolateral prefrontal cortex (DLPFC) as part of the multiple demand (MD) network.

5.2.5 Data processing

HD-DOT data were pre-processed using the NeuroDOT toolbox [26, 49]. Source-detector (SD) pair light level measurements were converted to log-ratio by calculating the temporal mean of a given SD-pair measurement as the baseline for that measurement. Then, channels with greater than 33% noisy first or second nearest neighbor measurements (nn1 and nn2) were excluded. Noisy measurements were empirically defined as those that have greater than 7.5% temporal standard deviation in the least noisy (lowest mean GVTD) 60 seconds of each run [49, 230]. Then the data were high-pass filtered to 0.02 Hz frequency. The global superficial signal was estimated as the average of the nn1 measurements (13 mm SD-pair separation) and removed from the data [21]. The optical density time-courses were then low-pass filtered to 0.5 Hz to the physiological brain

signal band. Noisy time-points were identified at this stage by setting a threshold (mode + 10 times the standard deviation of the values below the mode) on the global variance of the temporal derivatives (GVTD) index described in chapter 3 and later included as separate events (columns) in the GLM design matrix. Then the data were down-sampled from 10 Hz to 1 Hz. Wavelength dependent forward model of light propagation was computed using the standard non-linear Montreal Neurological Institute (ICBM152) anatomical atlas using the non-uniform tissue structures: scalp, skull, CSF, gray matter, and white matter [71]. Relative changes in the concentrations of oxy, deoxy, and total hemoglobin (ΔHbO_2 , HbR , ΔHbT) were obtained from the absorption coefficient changes by the spectral decomposition of the extinction coefficients of oxy and deoxyhemoglobin at the two wavelengths. Relative changes in absorption at 750 nm and 850 nm were then reconstructed using Tikhonov regularization and spatially variant regularization after inverting the sensitivity matrix [49]. For group analysis, we resampled all data to the $3 \times 3 \times 3$ mm³ MNI atlas using a linear affine transformation.

In addition to the standard HD-DOT data processing steps, a comprehensive data quality assessment pipeline (Appendix B) has been used to exclude the data runs with low heartbeat SNR, non-linear light falloff, and high motion levels. Details in Appendix B.

5.2.6 Hearing words task response mapping

The hearing words response was estimated using a standard general linear model (GLM). The design matrix was constructed representing the durations of the word presentation in the column and by convolving the experimental design with a canonical hemodynamic response function (HRF) using a two-gamma function (2 s delay time, 7 s time to peak, and 17 s undershoot) fitted to the HD-DOT data described in [98]. Motion regression was performed by adding a column in the design matrix for every time-point that passed the GVTD threshold. Extracted hemodynamic

response estimations (β maps) for each subject were then passed to the group-level summary statistics [231, 232].

5.2.7 Sentence and noise response mapping

For the sentence and noise task, we used a standard GLM with a design matrix with five columns representing: sentences, noise, visual probe word, left button press, and right button press. Auditory stimuli (sentences and noise) were modeled as 3 s events and button presses as 0 s events. Events were convolved with the same canonical HRF described in the hearing words task to model hemodynamic neural responses [98]. Similar to the hearing words task, motion regression was performed by adding a column in the design matrix for every time-point that passed the GVTD threshold. We included all data for each subject (4 runs) in one design matrix, using inhouse MATLAB code. In the main text, we only present the ΔHbO_2 results as we have found that the ΔHbO_2 signal exhibits a higher contrast-to-noise ratio compared to ΔHbR or ΔHbT [49, 98]. Extracted hemodynamic response estimations (β maps) for each subject were then passed to the group-level statistical analysis.

5.2.8 Audiovisual feature extraction from the movie viewing task

Similar to our previous study, the movie stimulus was decomposed into three features: auditory envelope, speech, and faces for extracting the related hemoglobin responses. Here, we are mainly interested in comparing the two auditory features, including the envelope of the auditory intensity, as well as the human-generated speech between the control and the CI group. The details regarding the generation of these feature indices can be found in the original paper [220]. For modeling the response to each feature, we convolved the raw feature time-traces with the same HRF used in the hearing words and sentence and noise analysis [98] and then performed a bandpass filtering ($0.02\text{ Hz} < f < 0.5\text{ Hz}$) on the regressor time-series to match the frequency band to the optical

density measurements [98]. We then calculated the temporal correlation between each feature time-series and the ΔHbO_2 time-course for all the voxels in the field of view, which resulted in a spatial map for each feature and each subject [220].

5.3 Results

5.3.1 Mapping the brain response to the hearing words task

We first investigated the degree of auditory activation in both control and CI groups by looking at the activity in a control block-design single word presentation condition (Figure 5.2B) and mapped robust responses to acoustic stimulation. These auditory responses helped to validate our approach and set the stage for more complex analyses looking at language-specific activity.

Our results showed strong bilateral superior temporal gyrus (STG) activations in controls similar to our previous studies for the same paradigm [22], as well as a strong left STG and a smaller right STG activation for the CI users. In addition to that, we found strong left-lateralized activations in regions beyond the auditory cortex, including parts of the prefrontal cortex in the CI user group (Figure 5.3).

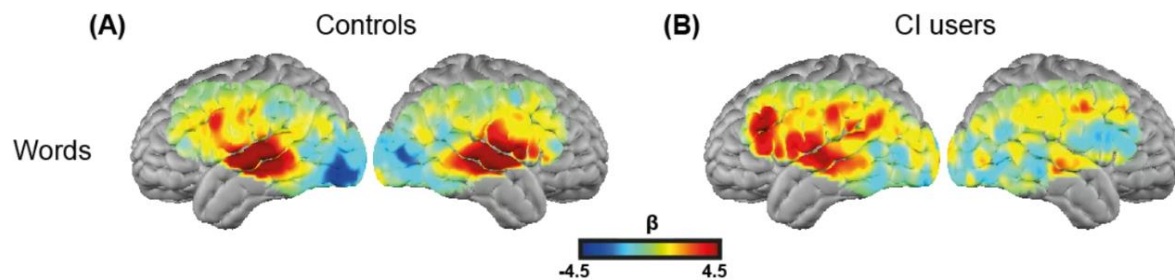


Figure 5.3: Hearing words task response mapping in controls and CI users. Response to the hearing words task for (A) 18 controls, and (B) 18 right-ear CI users.

5.3.2 Mapping the brain response to the sentences and noise-vocoded speech

The sentence and noise paradigm was designed to evaluate the differences between the cortical responses to intelligible speech and unintelligible noise between the control and CI groups. Our

preliminary analysis showed that the quantity and extent of the auditory and non-auditory activations are different between these two cohorts. In response to sentences, controls showed a strong bilateral STG activation as well as a strong left and right occipital cortex deactivation. However, CI listeners showed a strong left STG and a weaker right STG activation as well as some activity in the left prefrontal cortex in response to the intelligible sentences. When the response to noise was subtracted from the response from the sentences, the results looked very similar to the hearing words response (Figure 5.4) (bilateral STG for controls and left-lateralized STG and prefrontal cortex activation for the CI users, similar to Figure 5.3). Further statistical analysis and larger sample size are needed for this paradigm based on the estimated effect size for any interpretations of the results for this task.

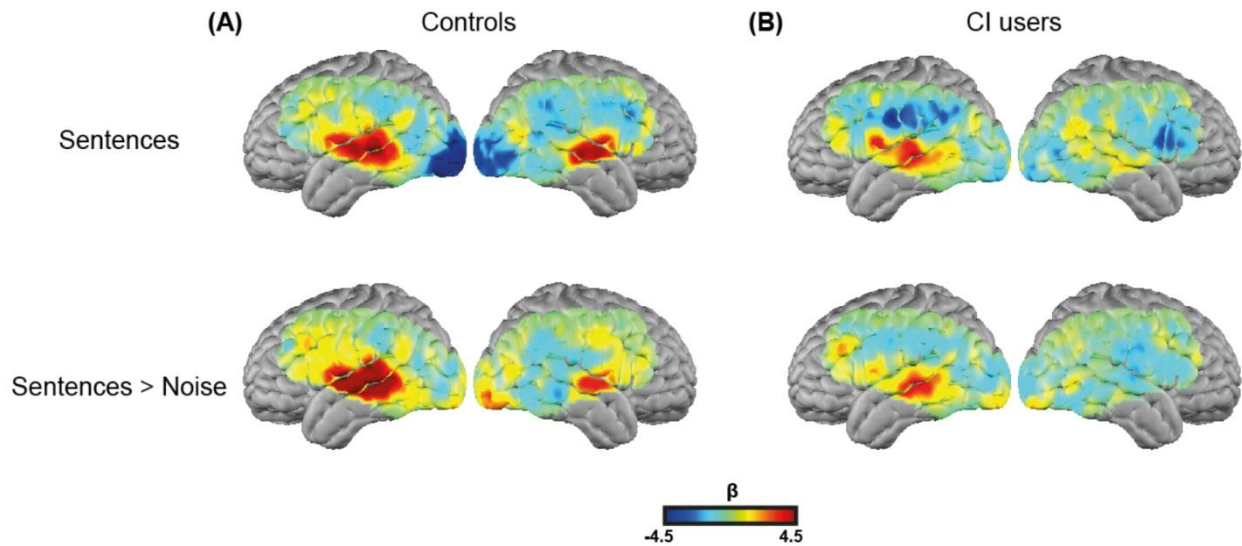


Figure 5.4: Sentence and noise task response mapping in controls and CI users. Responses to the noise-vocoded sentences, sentences, and sentences minus noise for (A) 18 controls, and (B) 18 right-ear cochlear implant users.

5.3.3 Mapping the brain response to movie features

The feature extraction procedure was applied following a prior study in our lab by Fishell et al., 2019, using multiple movie features across visual and auditory modalities. Here, I selected three

movie features, auditory envelope, speech, and visual face scenes. These audiovisual features were selected since previous studies in the CI users suggest possible differences in the auditory and visual cortex involvements in this cohort.

Our results show that voxels in the bilateral STG had the highest correlation coefficients to the audio envelope feature time-series in controls, while this strong correlation is missing in the CI group (Figure 5.5 first row). This could underscore the lack of sensitivity of this cohort to the amplitude and frequency features of the auditory signal due to the low spectral resolution of the CI.

The correlations between voxel-wise ΔHbO_2 and the speech feature revealed a bilateral response in the STG and left prefrontal cortex in the age-matched controls similar to the young control cohort reported in Fishell et al. However, the magnitude of the response to the speech was mostly dominated to the left STG and left prefrontal cortex for the CI group (Figure 5.5 second row).

Voxel-wise correlations between the time-courses of ΔHbO_2 and the face feature in controls revealed patterns of activation not only in extrastriate visual regions but also in auditory and speech processing regions similar to Fishell et al. and Wilson et al., 2008 [141, 233]. Surprisingly, in the CI cohort, the brain response to the faces was dominated in the left temporal cortex.

These results provide preliminary evidence for the expectation of the CI users to hear auditory stimuli when a face stimulus is present.

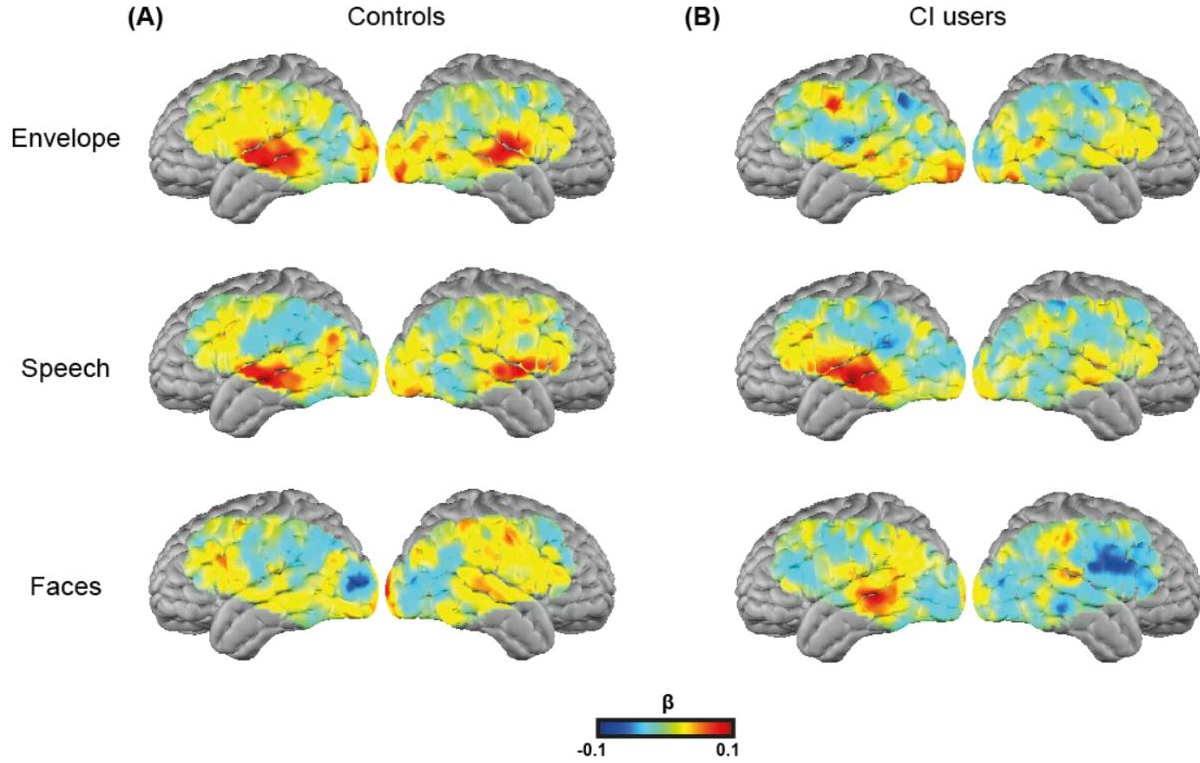


Figure 5.5: Movie feature mapping in controls and CI users. Examples of regression maps are shown for the audio power envelope, speech, faces, and hands in (A) 18 controls and (B) 18 right-ear CI users.

5.3.4 Mapping the brain response to all speech-related paradigms

Preliminary observations from all speech-related aspects of these tasks revealed a consistent involvement of bilateral STG in controls as previously presented for words [20], for sentences [22], for the speech from the movie [141], as well as a left prefrontal cortex activation for the speech features from the movie task. However, in the CI cohort, we observed more left-lateralized STG and prefrontal activation in response to both words and sentence > noise (Figure 5.6). These preliminary observations provide supporting evidence for the hypothesis of increased recruitment of the frontal cortex in the CI users as characterized in an effortful listening context due to their degraded sound quality where there is a lack of other visual assistance in the stimuli.

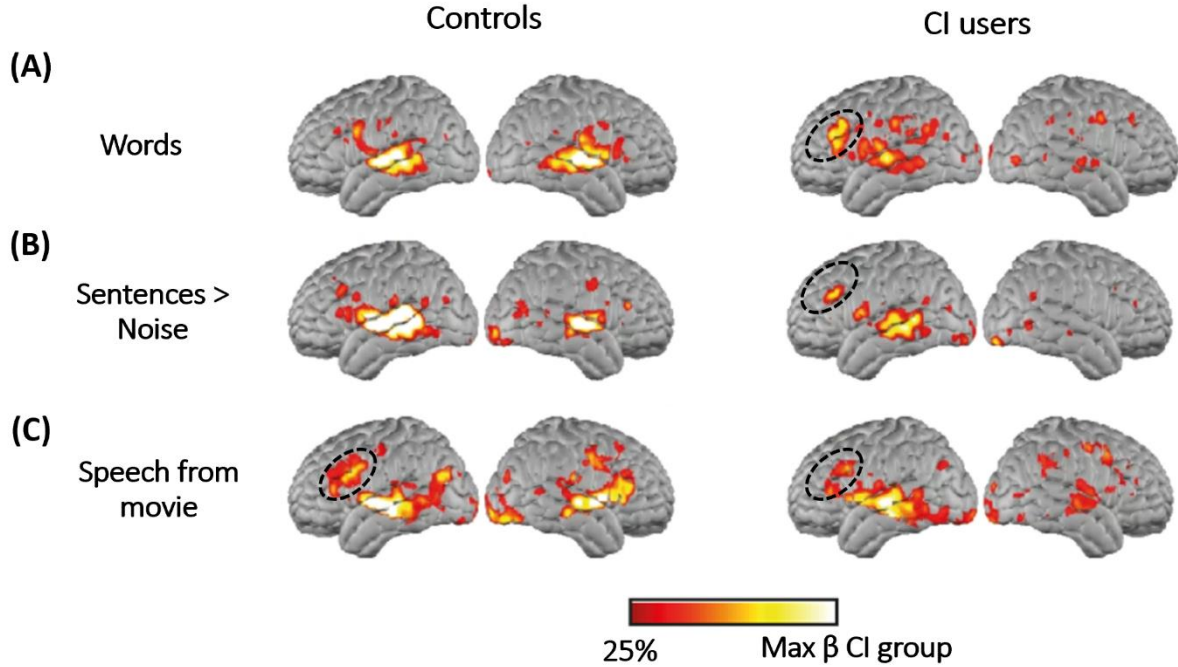


Figure 5.6: Summarizing the response to all speech paradigms in controls and CI users. Speech perception activation mapped in 18 controls and 18 CI recipients from the (A) hearing words paradigm, (B) sentence greater than noise, and (C) speech regressor analysis from a clip from “The Good, The Bad and The Ugly” movie.

5.3.5 Mapping the brain response to the spatial working memory task

In order to accurately localize the elevated prefrontal cortex activation in the CI user group, we adopted the spatial working memory task from [228] one CI user averaged over four different sessions. This task activates the multiple demand network (which includes the DLPFC region) as well as the occipital cortex due to its visual component. We chose this task to better localize the DLPFC ROI for performing an ROI-based statistical analysis between controls and CI users. Our results show a strong visual and DLPFC activation in response to this task (Figure 5.7A). We then defined the left DLPFC ROI by selecting a seed location based on the peak of the activation in the DLPFC region and found the strongest contiguous region that showed 50% or higher activation with respect to that seed location (Figure 5.7B).

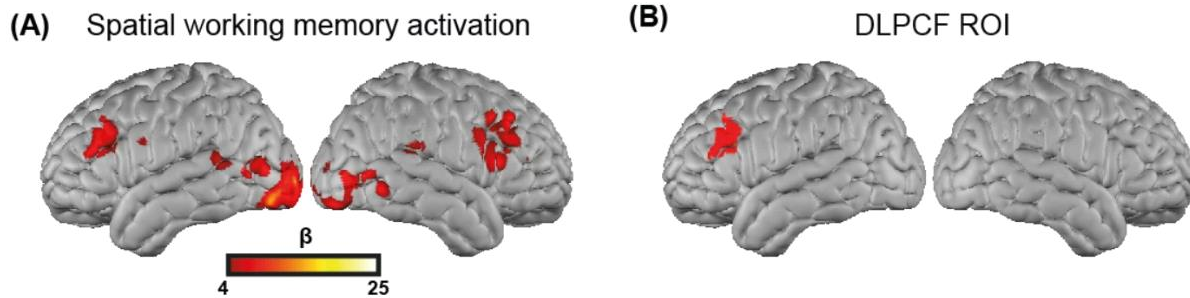


Figure 5.7: Defining the left DLPFC ROI using the spatial working memory task (A) Spatial working memory activation for one CI user averaged over four sessions. (B) The DLPFC ROI was defined based on the strongest contiguous region to a seed in that region with at least 50% of the activation magnitude to the seed location.

5.3.6 Statistical analysis and group differences for the hearing words task

The hearing words task showed the greatest effect size in the defined DLPFC ROI (Figure 5.6A). Therefore, we further investigated the differences between the control and CI group in response to the HW activation by first performing a voxel-wise subtraction of the control group map from the CI group map. This voxel-wise subtraction map (Figure 5.8A) showed a clear decrease in response in the left and right auditory cortex in the CI group as well as an increase in parts of the prefrontal cortex and left and right visual cortices. Based on these observations, we performed a paired t-test analysis between the sample of mean beta values of single subjects in controls and a sample of mean beta values of single subjects in the CI group in three ROIs: left DLPFC and left and right auditory cortices. The DLPFC was defined based on the spatial working memory task, as explained in §5.2.4.4. The left (right) auditory ROI was determined based on the seed map analysis of resting state data from a separate dataset (dataset 2 in chapter 3 §3.3) by locating a seed at the right (left) auditory ROI and finding the correlation of the seed time-trace in that region to all other voxels of the brain (more details in chapter 3 §3.2.9.2). This approach was used to objectively determine the left and right auditory ROIs for performing statistical analysis for between-group comparisons.

Our statistical analysis showed a significant decrease in left and right auditory ROIs and a significant increase in the left DLPFC ROI in the CI user group ($P < 0.05$) (Figure 5.8).

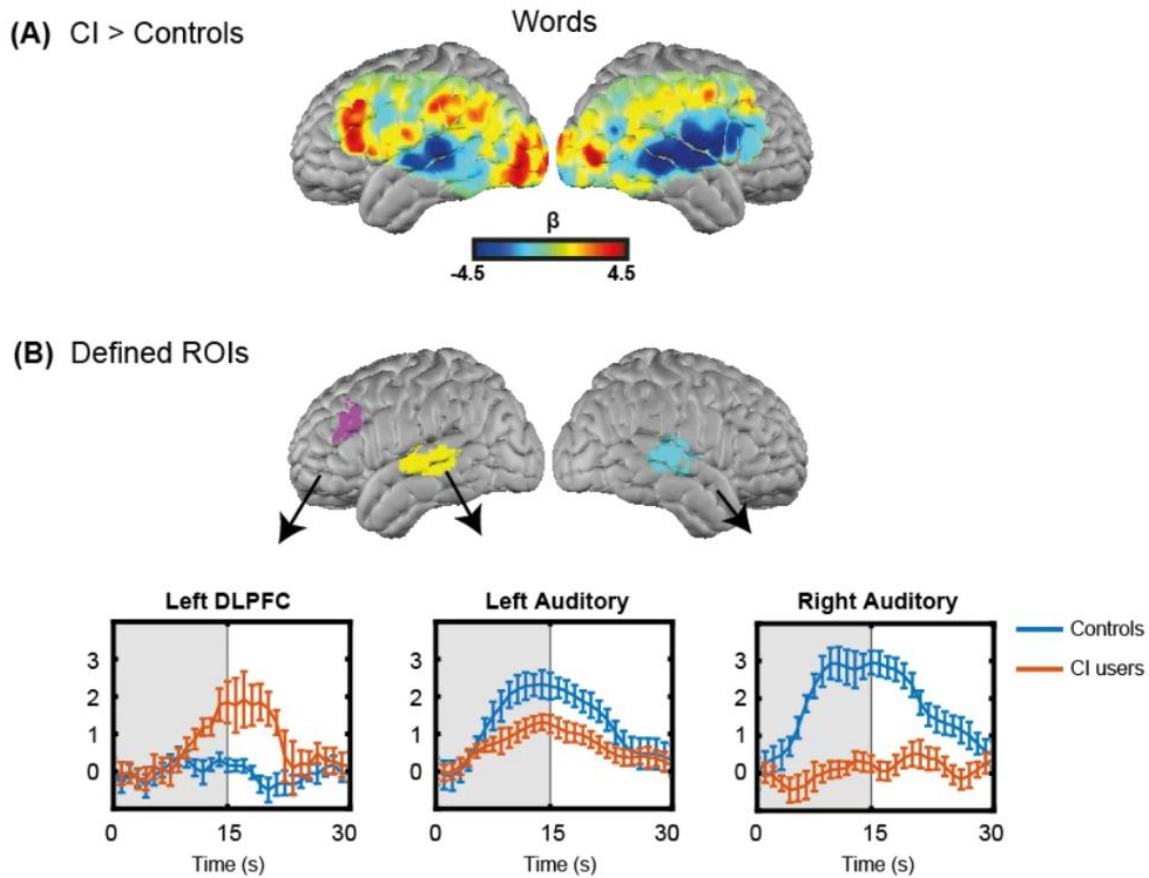


Figure 5.8: ROI-based analysis for the hearing words task in controls vs. CI users. (A) Differential activation in response to the hearing words task by CI > Control highlights the group differences in certain brain areas. (B) Temporal profile of the hemodynamic response to the hearing words task in three selected ROIs with $P < 0.05$ statistical significance difference; left DLPFC, left auditory, and right auditory ROI.

5.3.7 Behavioral measurements

An important consideration in studying the CI users is the variability in their speech understanding and the relationship between their cortical activity and their behavioral measures. This is a long-term goal for this project to make these CI surgeries more efficient for individuals by learning more about each individual's brain activity before surgery. For this study, we have collected a

comprehensive set of behavioral data including handedness, age of deafness, length of implant use, age at the scan, etiology, speech intelligibility, audibility threshold, Shipley, MoCA, and Stroop test scores. Our future goal is to perform a more comprehensive statistical analysis between these behavioral measures and the HD-DOT results.

5.3.7.1 Speech intelligibility

Among all the behavioral measures presented in §5.3.7, speech intelligibility is one of the most important scores. More importantly, our hypothesis was whether there is any correlation between the recruitment of the DLPFC and the individual's speech intelligibility score. Figure 5.9 shows the speech intelligibility scores for all controls and all CI users. As evident, the speech intelligibility score is very consistent across controls (~100% for all subjects) and is more variable across the CI users (~60-100%). Future work is needed for finding the correlation values between the speech intelligibility scores and the magnitude of the activations in each of these ROIs.

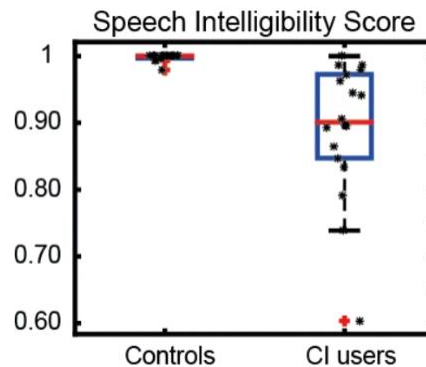


Figure 5.9: Speech intelligibility score across controls and CI users. 1 is 100% accuracy.

5.4 Discussion

In this chapter, we presented a preliminary analysis of the HD-DOT neuroimaging results for the data collected from 18 right-ear CI users and 18 age- and sex-equivalent controls performing various speech-related tasks. Our results from three speech paradigms (words, sentences and noise,

and movies) show a consistent decrease in the left and right auditory cortex activation in the CI user group across all paradigms compared to the controls. Further, we have found an increase in the left prefrontal cortex in the CI users across two auditory-only tasks (words and sentence greater than noise) (Figure 5.6A, B) which is supporting the evidence for the hypothesis of increased recruitment of the frontal lobe in the CI users in an effortful listening situation. This was as opposed to seeing a significant increase in this area in the movie paradigm, which has the visual element besides the auditory feature.

In the previous studies regarding the effortful listening and CI-aided listening, there is supporting evidence for the involvement of both left inferior frontal gyrus (IFG) and left dorsolateral prefrontal cortex (DLPFC) (two spatially close regions of the frontal lobe) in supporting cognitive demand [266]. Given the possibility of the variable optode placements in the optical imaging techniques and for eliminating concerns regarding our localization accuracy, we have added a previously described spatial working memory paradigm that is shown to activate the DLPFC region in a subset of our participants [267]. Defining the DLPFC ROI using the working memory task provides a quantitative functionally defined ROI that enabled performing an ROI-based statistical significance analysis for finding differences across controls and the CI group without concerns about the multiple comparisons problem. DLPFC is a region that is known to play an important role in executive functions such as working memory and abstract reasoning. DLPFC is also one of the nodes of the frontoparietal attention network and plays a key role when people pay more attention to the meaning of a sound [7, 8]. This frontal activation is consistent with a need to rely on executive resources to compensate for a degraded acoustic signal. These findings support the theory of cognitive demand increase in the effortful listening situation in hearing [245] with a

CI and provide the very first high-quality fMRI-like measurement of the cortical language network organization in the CI user population.

Prior to this study, in multiple other studies, we have made comprehensive comparisons between the HD-DOT results and fMRI results by calculating the voxel-wise similarity of both hearing words task and other resting state networks (visual, auditory, somatomotor, dorsal attention, etc.) using the same HD-DOT cap (Chapter 3, Figures 3.6, 3.7, and 3.8). However, this is the first time the DLPFC ROI has been localized with this HD-DOT imaging device.

Another important issue in studying the CI users is the variability in their speech understanding and the relationship between their cortical activity and their behavioral measures. For this study, we have collected a comprehensive set of behavioral data including handedness, age of deafness, length of implant use, age at the scan, etiology, speech intelligibility, audibility threshold, Shipley, MoCA, and Stroop test scores. Our future goal is to perform a more comprehensive statistical analysis between these behavioral measures and the HD-DOT results.

In order to use HD-DOT to study patients with cochlear implants, we need to reliably map language networks at the level of individual listeners. Doing so has proven extremely challenging in fMRI, and several additional HD-DOT-specific technical hurdles need to be addressed relating to the signal-to-noise ratio (SNR) and source localization accuracy of single subject data. Solutions require developing algorithms that can reduce noise and motion artifacts, as presented in chapter 3 and implemented in this chapter, for data denoising and data processing to gain more reliable single subject mapping with HD-DOT in the future.

5.5 Conclusion

In this chapter, we mapped the neural systems supporting speech perception in listeners with CIs

using HD-DOT. Across each of the three different speech paradigms, the HD-DOT mappings demonstrate robust responses in subjects with CIs and age-equivalent controls. Further, the CI responses were shown to be statistically different compared to the control group. More specifically, we provided evidence that the DLPFC supports speech processing in CI listeners and compensates for the decrease in the left and right auditory cortex activations.

Chapter 6: Conclusion

High-density diffuse optical tomography (HD-DOT) has tremendous potential to be a surrogate for fMRI in naturalistic settings and when fMRI is contraindicated. However, methods for dealing with detection and suppression of motion artifacts are relatively underdeveloped for HD-DOT, which limits its application to many important clinical populations.

In this thesis, I have provided a comprehensive assessment of the data quality measures for HD-DOT data and validated the efficacy of these measures in multiple datasets. In chapter 3, I implemented all the current motion correction methods in the fNIRS literature for HD-DOT, as well as presenting a novel global motion detection technique called GVTD, inspired by the methods used in fMRI. The results presented in chapter 3 show that similar to fMRI, none of the current motion correction methods can fully reverse the effect of severe motion artifacts. We conclude that for the current versions of the HD-DOT system, a process called motion censoring or motion scrubbing outperforms other motion correction methods and makes HD-DOT maps more similar to those of fMRI.

In chapter 4, I adopted the proposed motion detection and motion censoring methods to a clinical HD-DOT dataset in Parkinson disease (PD) patients with high-motion and high tremor levels with DBS STN implants. Our results showed that with a sample size of $n = 15$ PD patients with their DBS off, HD-DOT replicates the results obtained with fMRI for $n = 107$ PD patients without DBS [31]. We could also replicate the results of another similar PET study but with a faster DBS on/off paradigm using HD-DOT using our DBS activation study (8 sec ramp up, 18 sec on, 16-24 sec off) and showed that these results would not have been achieved if the data has not been denoised properly. The results presented in chapter 4 are a steppingstone for a broader application of HD-

DOT as a reliable surrogate to fMRI in people with severe tremors and high levels of motion artifacts.

Finally, in chapter 5, I applied the analysis methods explained in chapters 2 and 3 to another clinical HD-DOT dataset for people with auditory impairments using cochlear implants (CI). The speech intelligibility is highly variable and very poorly understood in these people after their CI surgery due to their contraindications with the current gold standard neuroimaging techniques. Therefore, the ability to reliably map the cortical brain function in these people and finding meaningful relationships between their brain activity and their behavioral measures can shed light on better optimizing these cochlear implant surgeries. The importance of selecting this population for this thesis was the incomplete spatial sampling of the cap-based HD-DOT imaging system due to the external CI transducer attached to these people's heads. To overcome this problem, in the supplementary material for chapter 5 (Appendix B), I presented a step by step data quality assessment pipeline for analyzing this cohort's data and showed that HD-DOT could reliably map the neural correlates of speech processing in the CI users by obtaining plausible results that were in agreement with the previous literature. This chapter enabled the tools needed for finding the correlations between the behavioral scores and HD-DOT brain images when a larger sample size is in hand.

In summary, this thesis presents an in-depth analysis of the effects of motion artifacts in HD-DOT data at both single-channel level and across channels. I also developed software for implementing all these measures compatible with the current HD-DOT data processing toolbox, NeuroDOT [95]. These implementations at the software level provide a substantial advancement in neuroimaging capabilities of HD-DOT in various clinical and non-clinical situations. In particular, this thesis enables the critical milestones of scanning real clinical populations such as PD patients with DBS

STN implants, essential tremor (ET) patients with DBS VIM implants, and people with CIs using HD-DOT and paves the way for reliably using this modality as a surrogate to fMRI.

Appendix A: Supplementary Materials for

Chapter 3

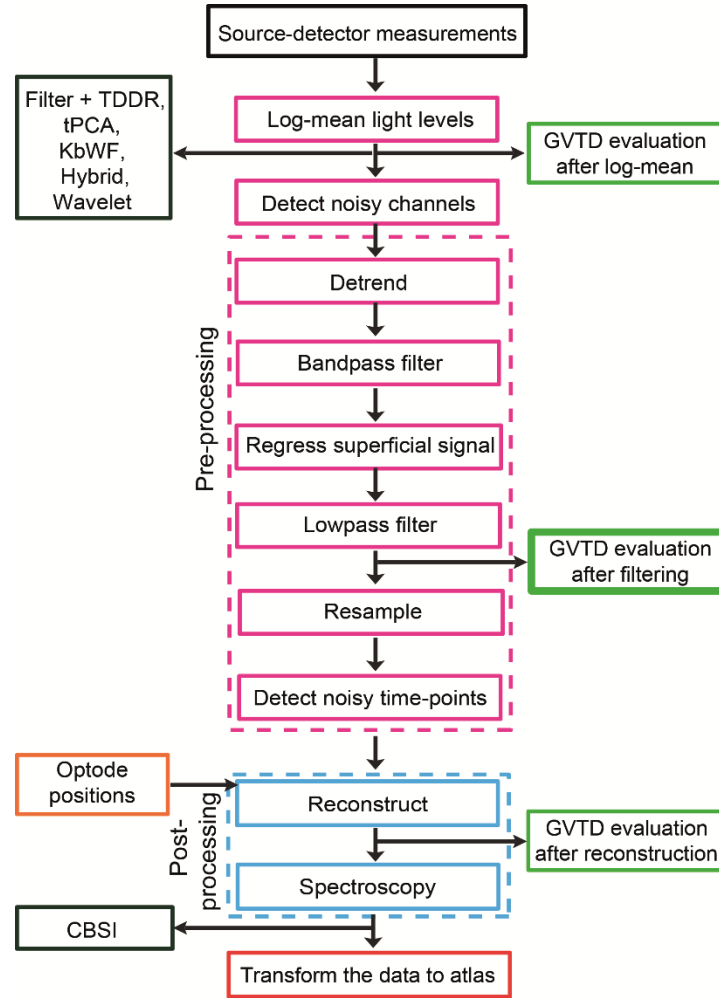


Figure A.1: Motion removal methods in HD-DOT data processing pipeline. Dashed pink and blue boxes show the pre- and post-processing steps, respectively. GVTD was evaluated (§3.4) at three stages in the pipeline indicated by green boxes. The best separation between baseline signal and motion artifact was obtained “after filtering” (thicker outlined green box).

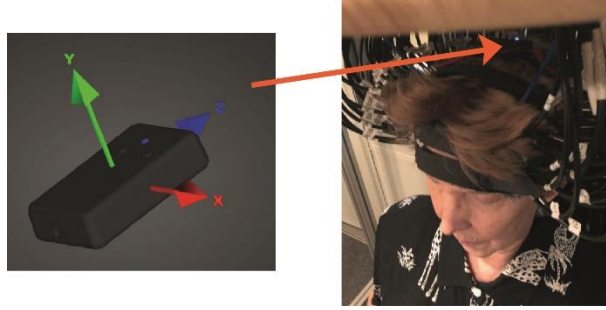


Figure A.2. The placement of the motion sensor on HD-DOT cap. 3-space™ USB/RS232, Yost Labs, was attached to the top strap of the HD-DOT device for concurrent recording of the head motion and optical data in dataset 2.

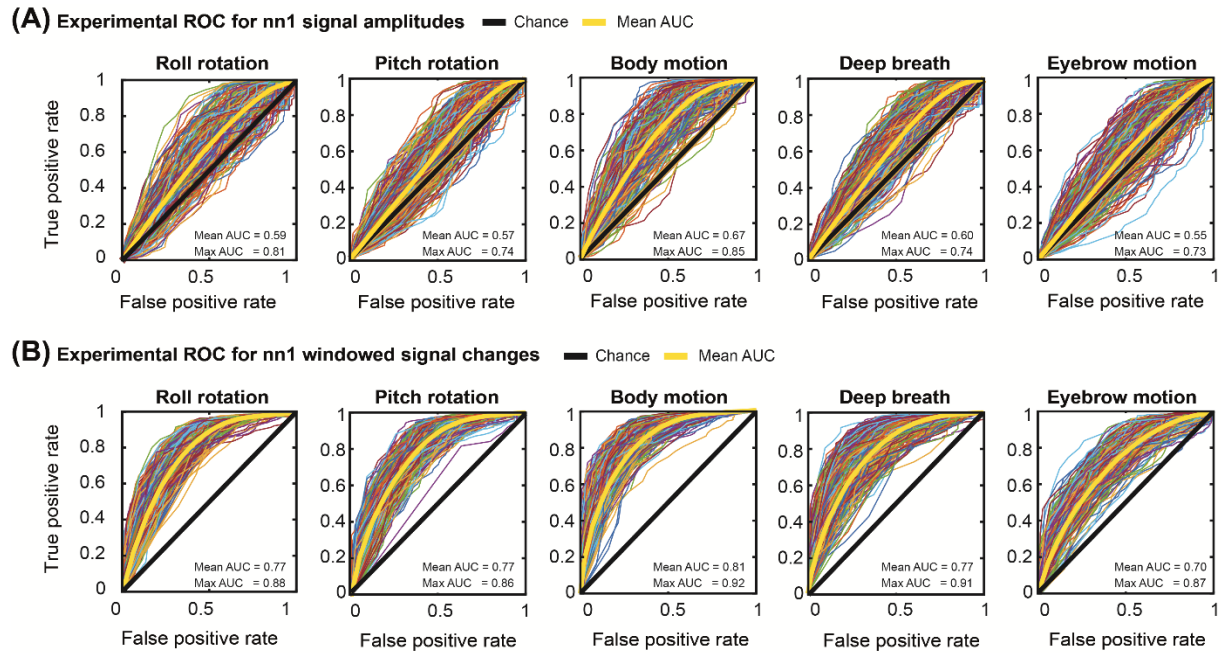


Figure A.3: The ROC curves for signal amplitudes and windowed signal amplitudes. The experimental ROC curves are drawn for (A) the absolute signal amplitude of 850 nm nn1 measurements, the yellow curve shows the mean of all ROC curves and (B) the windowed amplitude changes of the signals in (A), the dark magenta curve shows the mean of all ROC curves. The goal of this figure is to show that regardless of the type of motion, both maximum and mean of the area under the curve (AUC) of the ROC curves in each figure is still lower than or equal to the AUC of GVTD in Figure 3.4.

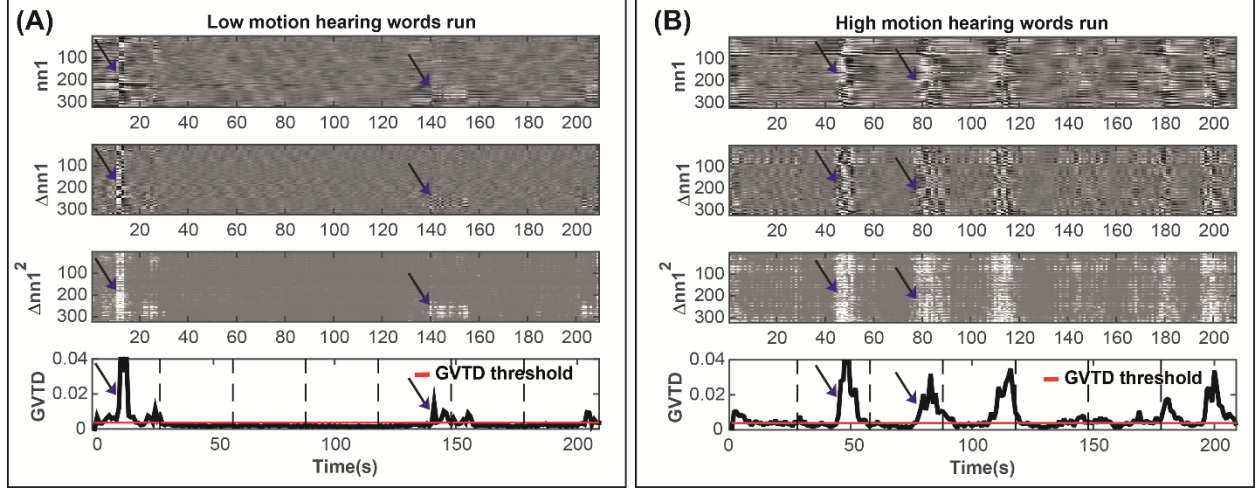


Figure A.4: Motion censoring process for the hearing words task. The four-step process for calculating the GVTD time-courses (A) for a low motion subject and (B) a high motion subject in dataset 3. Dashed lines indicate the onsets of the blocks of hearing words run (6 runs each 30 sec). The red line shows the GVTD threshold of $g_{thresh} = \tilde{\kappa} + 3\sigma_L$. Blocks with time points exceeding the GVTD threshold are excluded from the analysis (4, 5, 6 for the low motion subject, and all blocks for the high motion subject). Dark blue arrows indicate some examples of the high contrast in both the gray plots and the spikes of the GVTD time-courses for instances of motion artifacts.

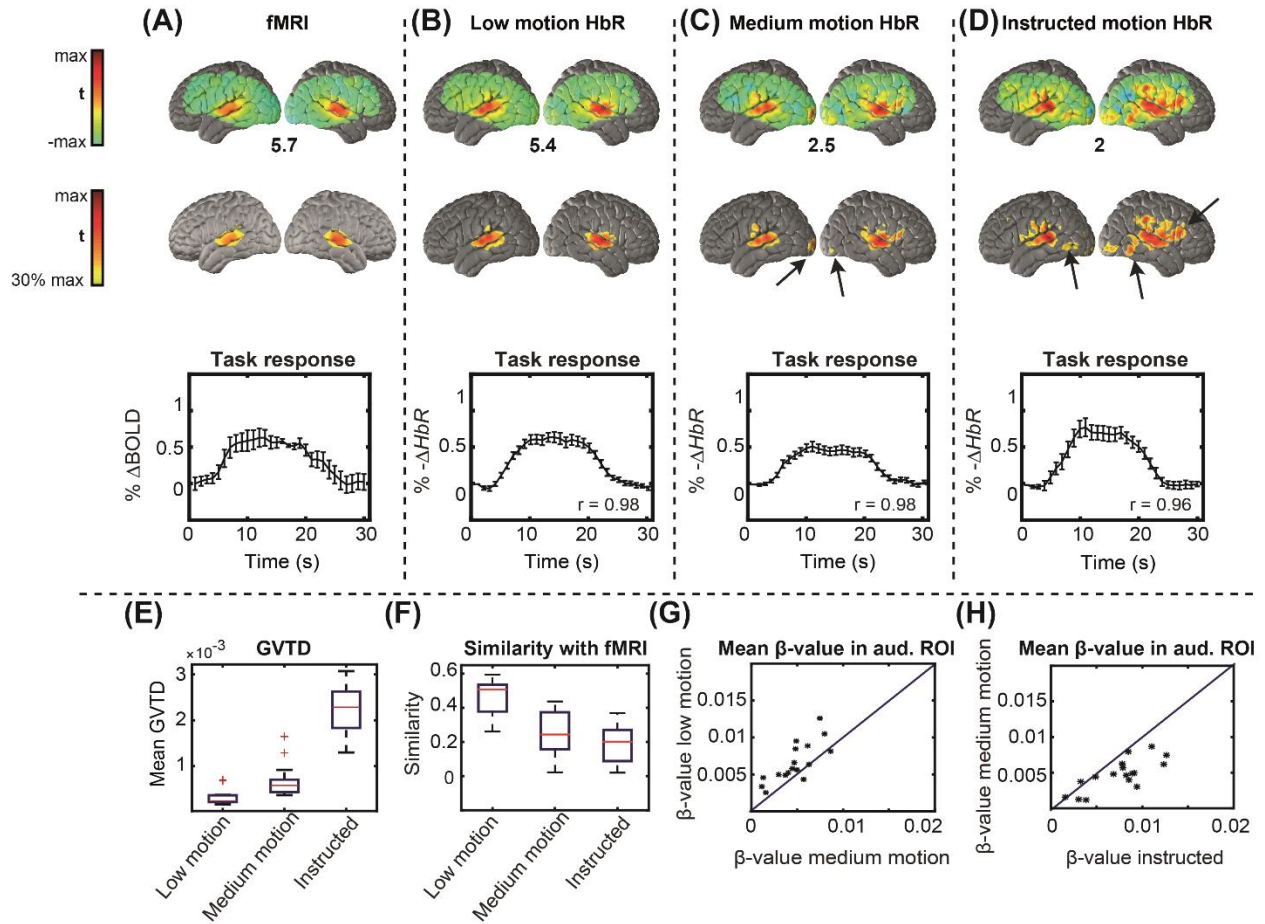


Figure A.5: Indexing motion using GVT in HD-DOT hearing words HbR maps. Same HW task t-statistic evoked responses, as Figure 3.6 are replicated with HbR contrasts. (A) Reference dataset. (B) Low-motion data. (C) Medium motion data. (D) Instructed motion data. Black arrows indicate false-positive responses, designated since they occur outside auditory ROI defined based on the reference fMRI dataset. The maximum t-value of each group is shown below the maps. (E) Mean GVT values across all trials in low-motion, medium motion, and instructed motion data. (F) Mean similarity of the maps in each condition with the reference dataset, similarity defined as the voxel-voxel Pearson correlation. (G) Scatter plot of responses in low vs. medium motion ordinary trials; GVT indexed stronger responses in low-motion trials in 15 of 17 sessions. (D) Scatter plot of medium motion vs. instructed motion trials; note the higher spurious response magnitudes for the instructed motion.

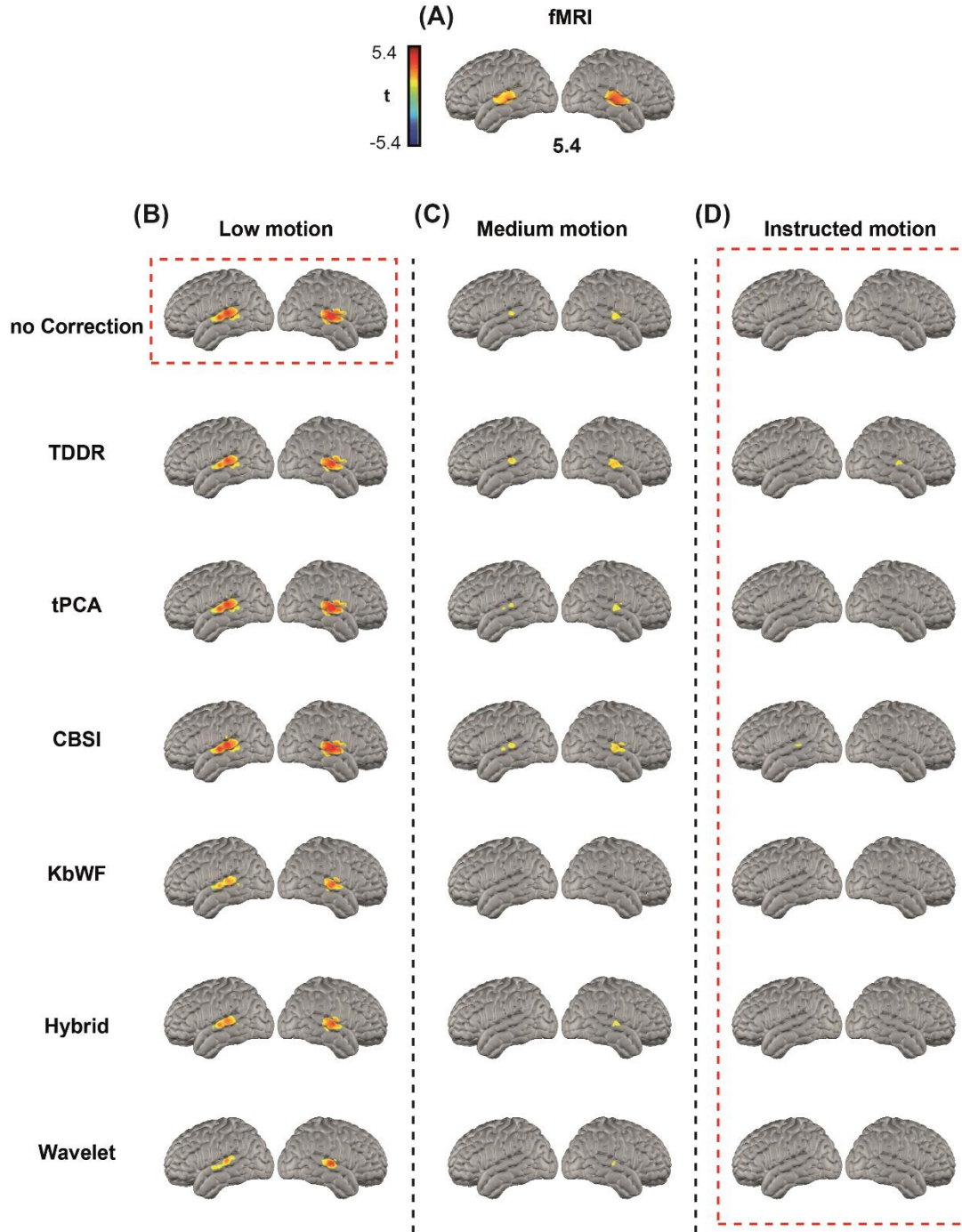


Figure A.6: Efficiency of motion removal methods in task HD-DOT data with different motion levels; thresholded. Voxel-wise maps are shown for (A) Reference fMRI dataset. (B) Low-motion data. (C) Medium motion data. (D) Instructed motion data for the three motion level categories determined with mean GVTD scores. Rows represent maps corrected with TDDR, tPCA, CBSI, Kurtosis wavelet, Hybrid, and wavelet filtering methods. All maps are thresholded at $P < 0.05$.

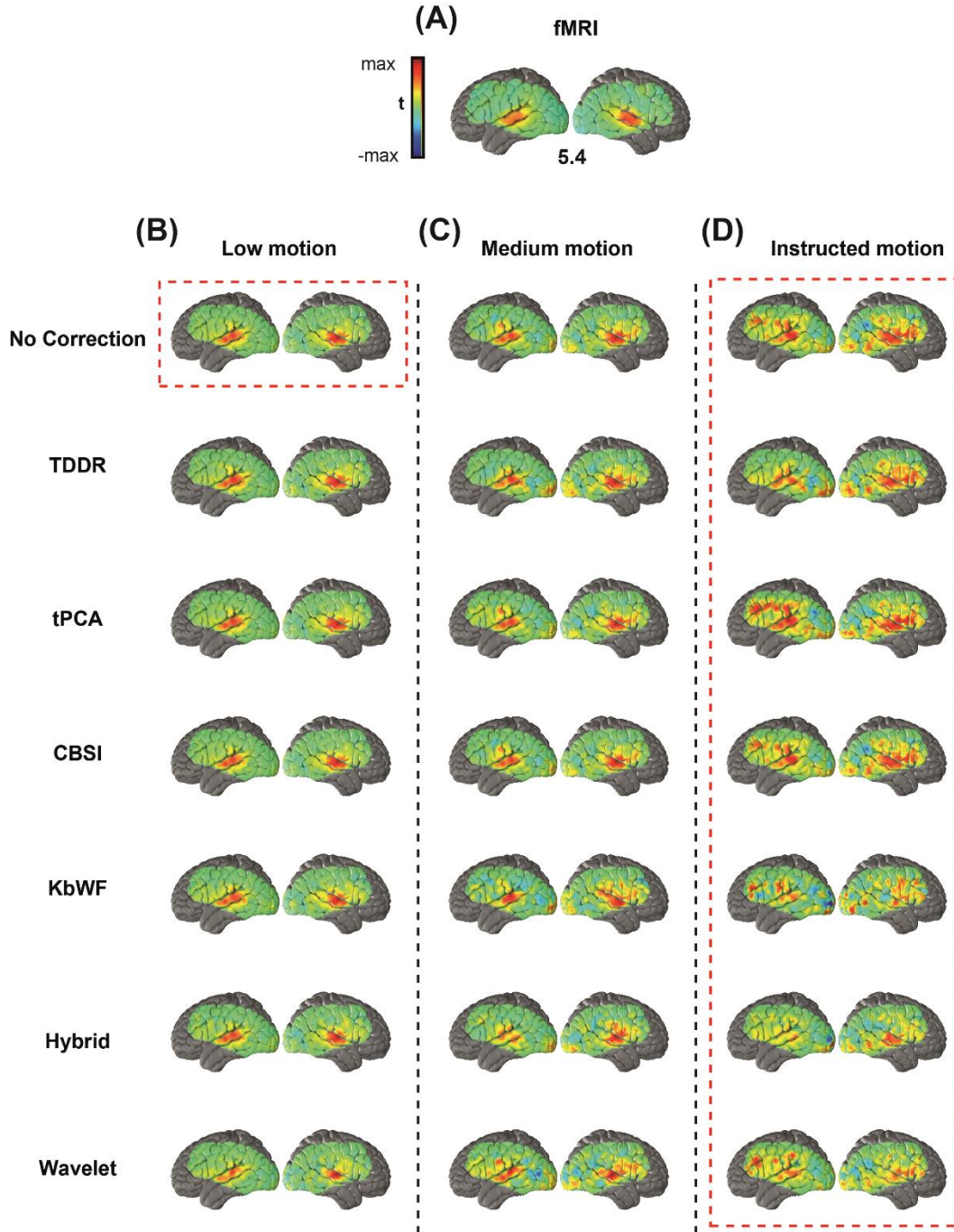


Figure A.7: Efficiency of motion removal methods in task HD-DOT data with different motion levels; no threshold. The same maps described in Figure A.6 visualized with no thresholding. Voxel-wise maps are shown for (A) Reference fMRI dataset. (B) Low-motion data. (C) Medium motion data. (D) Instructed motion data for the three motion level categories determined with mean GVTD scores. Rows represent maps corrected with TDDR, tPCA, CBSI, Kurtosis wavelet, Hybrid, and wavelet filtering methods.

Table A.1: List of the parameters for motion correction in task data.

	StatType	numStd	tMotion	tMask	STDEV thresh	AMP thresh	nSV	iqr	kurt	p	FrameSize_ sec	tune	filter_cutoff
GVTD	Histogram _Mode	3											
CBSI													
TPCA			0.5	2	20	0.5	0.97						
Wavelet								1.5					
KbWF									3.3				
Hybrid (S+SG)										0.99	15		
TDDR												4.695	0.5

Table A.2: List of the parameters for motion correction in resting state data.

	StatType	numStd	tMotion	tMask	STDEV thresh	AMP thresh	nSV	iqr	kurt	p	FrameSize_ sec	tune	filter_cutoff
GVTD	Histogram _Mode	10											
CBSI													
TPCA			0.5	2	20	0.5	0.97						
Wavelet								1.5					
KbWF									3.3				
Hybrid (S+SG)										0.99	15		
TDDR												4.695	0.5

A.1 Finding the histogram mode based on the parabolic interpolation

For estimating the mode of a given GVTD time-course, we calculated a histogram for each run by defining the width of the bins, $w = \max \mathbf{g} / nint(M/\ell)$, based on the maximum value of the GVTD time-course (\mathbf{g}) and the nearest integer ($nint$) to the quotient of the length of the GVTD time-course (M) and a fixed parameter for the minimum count per bin (ℓ) (in our case we chose 5 minimum counts per bin). Finding the mode based on the histogram is sensitive to the binning process. Therefore, an alternative method for better estimating the mode (bin with the maximum value) of the histogram is to use the parabolic interpolation approximation. Parabolic interpolation estimates the local extremum value of a function by fitting a quadratic parabola on three successive

points in the function. In our case, we can estimate the mode based on the parabolic interpolation of the bin with the maximum value (x_2, y_2) and its preceding (x_1, y_1) and succeeding bins (x_3, y_3) (Eq. (A.1), Figure A.8).

$$mode = \frac{1}{2} \frac{(x_2^2 - x_1^2)(y_2 - y_3) - (x_2^2 - x_3^2)(y_2 - y_1)}{(x_2 - x_1)(y_2 - y_3) - (x_2 - x_3)(y_2 - y_1)}, \quad (A.1)$$

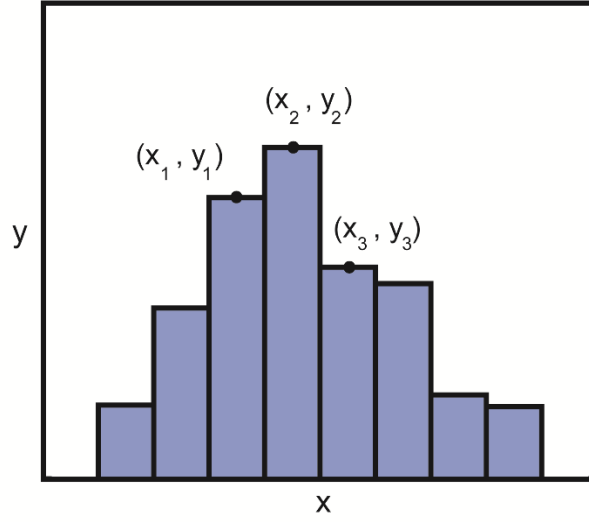


Figure A.8. Parabolic interpolation. Demonstration of mode identification using parabolic interpolation of binned data. The histogram peak occurs at (x_2, y_2) .

A.2 Finding the mode of GVTD values based on the kernel density estimation

As discussed in §3.3, because of the sum over the square of the temporal derivative, the GVTD distribution is not normal and is skewed to the right. Therefore, for overcoming the binning problem, one can perform a kernel density estimation. However, we need to perform a curve-fitting approach to find the best match for the type of kernel.

Mathematically, the GVTD definition is very similar to the Chi distribution (assuming that the input optical density signals are normal). However, in order to have an exact Chi distribution, we need to have a standard normal distribution before finding the RMS of the square of the derivatives

of measurements or voxels j at time-point i (y_{ji}). Therefore, an alternative metric to GVTD could be defined as the global variance in the standardized temporal derivative, $X_i = \sqrt{\sum_{j=1}^N ((\delta_{ji} - \mu)/\sigma)^2}$, where $\delta_{ji} = y_{ji} - y_{ji-1}$, μ is the mean of the δ_{ji} values, σ is the standard deviation of the δ_{ji} values and N is the number of SD- pair measurements. Another approach is to find the kernel density estimation of the logarithm of the GVTD values, which is closer to normal than GVTD itself. Then, one could find the mode of the probability density function (pdf) of the $\log(\text{GVTD})$ and find the corresponding mode value for GVTD itself.

Appendix B: Supplementary Materials for

Chapter 5

B.1 Data quality measures

After preprocessing, all data were passed through a rigorous data quality assessment, including three steps: 1) linearity of the log of light fall-off with source-detector distance (characteristic of the modified Beer-Lambert law). 2) Presence of the ~1 Hz frequency content of the heartbeat. 3) Exclusion of the motion content using the gray plots and GVTD time-traces. These steps are elaborated in more detail below. All data not passing these measures were excluded from the group analysis.

B.2 Linear logarithmic falloff

One way to ensure that the collected data with the DOT devices are reliable is to evaluate the coupling extent of the optodes to the scalp by looking at the plot of the detected light levels (optical density changes) vs. the source-detector separation. The detected optical density changes from each subject at the baseline are following a linear log falloff, which is the characteristic of the modified Beer-Lambert Law (Figure B.1C).

Based on the modified Beer-Lambert law, the changes in the optical density (ΔOD) of the sample (determined by the negative log ratio of the detected intensity of light I with respect to the incident intensity of light I_0) is proportional to the change in the absorption coefficient of the tissue μ_a multiplied by the net distance traveled by the light from the source to the detector, L , scaled by the differential path-length factor D_{PF} . D_{PF} accounts for the extra total distance that light travels through the tissue due to scattering.

$$\Delta OD = -\log I / I_0 = \Delta \mu_a \times L D_{PF} \quad (A.2)$$

Therefore, in an ideal measurement, the detected light levels should be linearly dependent to the source-detector separation:

$$-\log I / I_0 \sim L \quad (\text{A.3})$$

In our HD-DOT device, the light from each source is detected at multiple source-detector distances (Fig. B.1A). We define the closest separation as 1st-nearest neighbors, and increasing distances are known as second-, third-, and fourth-nearest neighbors (shortened to nn1, nn2, nn3, nn4, etc.). Therefore, the detected optical density changes can be plotted with respect to all source-detector separations and be evaluated whether they follow a reasonable trend (Figure B.1C) or not (Figure B.1D). If the changes in the light levels detected from nn2 or nn3 do not drop in a linear trend, that could be an indicator of poor absorption and scattering of light to the head tissue and, thus, a low-quality measurement.

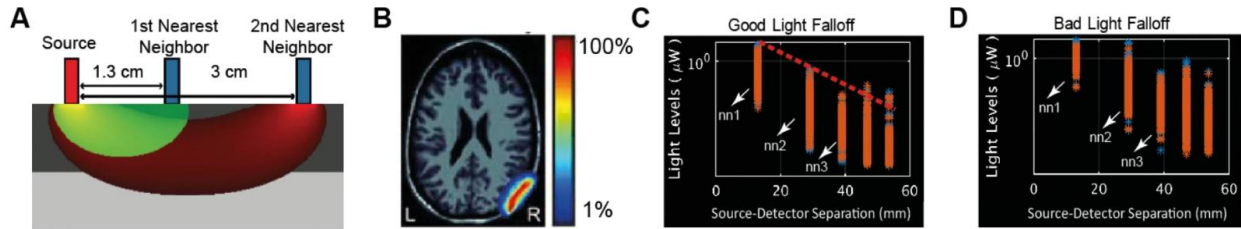


Figure B.1: Examples of a good and a bad light falloff plot in HD-DOT data. (A) Slices through a semi-infinite simulation of photon flow for 1st- and 2nd-nearest neighbor separation, Greg et al., 2010. We see that 1st-nearest neighbors are sensitive mostly to scalp and skull, while 2nd-nearest neighbors' sample into the brain Eggebrecht et al., 2014. (B) (C) As source-detector distance increases, the power detected falls off exponentially, until it reaches the noise floor (~ 10 pW) in a good quality scan. However, if the optodes are not fully coupled to the head or there is a lot of noise due to motion, this linear log falloff is not present as the source-detector separation increases.

B.3 Presence of the heartbeat frequency in the signal

In order to evaluate how well the collected HD-DOT data could capture the physiological signal in each data run, it is easy to look for the very well-known measure of heartbeat frequency (typically ~ 1 Hz in adult humans) in both time and frequency domains (Figure B.2A, B). If the intensity of this frequency is low or missing, that is an indicator of a low-quality data that could not capture the physiological signal with lower frequencies (task responses 0.02-0.5 Hz and resting state 0.009-0.08 Hz) (Figure B.2).

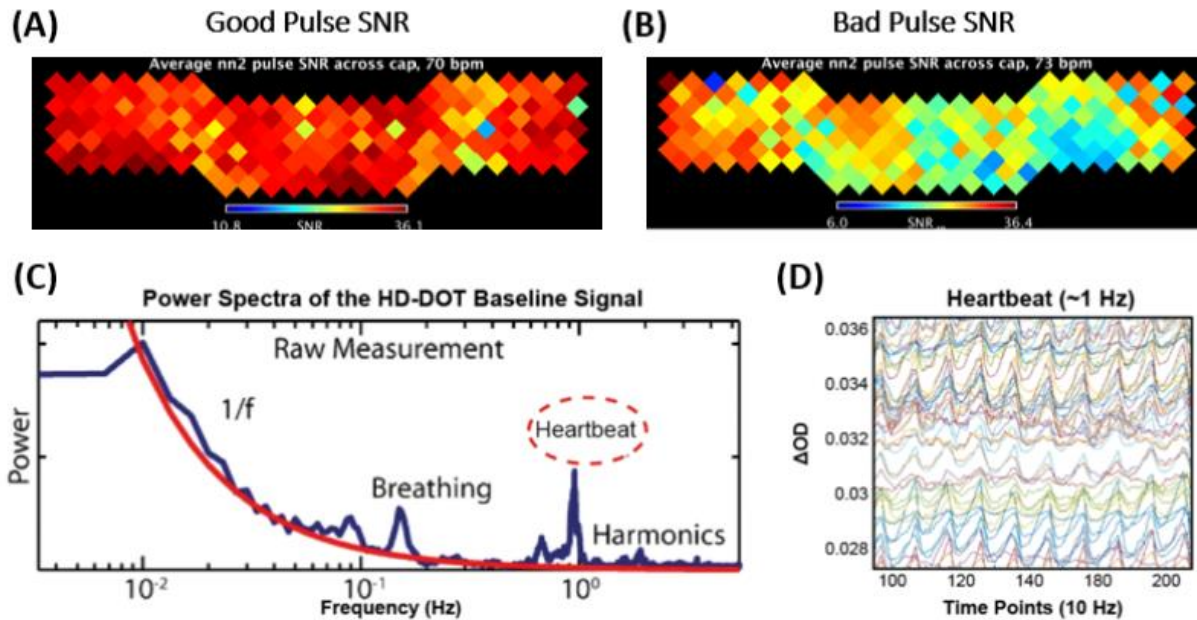


Figure B.2: Examples of a good and a bad heartbeat SNR plot in HD-DOT data. High SNR for the frequency of the heartbeat (~ 1 Hz) is a characteristic of high-quality HD-DOT data (A, B). (C) power spectra of the HD-DOT baseline signal, White 2010. (D) The plot of a selection of the measurements from the HD-DOT array shows the heartbeat frequency (10 peaks in 100 time-points, equivalent of 10 sec = 1 Hz).

B.4 Motion detection using GVTD

Motion artifacts were detected in a time-point by time-point manner on the 10 Hz light-level signals, using the global variance of the temporal derivatives (GVTD) motion index fully described in chapter 3 [29].

Figure B.3 shows an example GVTD time-trace for a low-motion and a high-motion hearing words run. For this project, I evaluated different methods for using the GVTD time-trace in denoising HD-DOT block-design (hearing words) and event-related design (sentence and noise task).

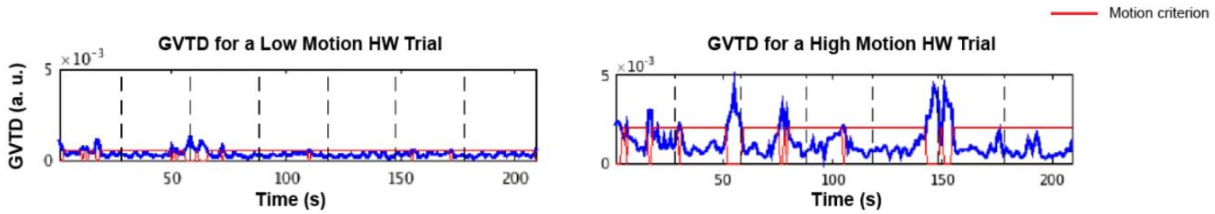


Figure B.3: Examples of GVTD time-traces for a low-motion and a high-motion HD-DOT data.

References/Bibliography/Works Cited

1. Ogawa, S., et al., *Oxygenation-sensitive contrast in magnetic resonance image of rodent brain at high magnetic fields*. Magn Reson Med, 1990. **14**(1): p. 68-78.
2. Sereno, M.I., et al., *Borders of multiple visual areas in humans revealed by functional magnetic resonance imaging*. Science, 1995. **268**(5212): p. 889-93.
3. Obata, K., et al., *Atrial natriuretic polypeptide is removed by the lungs and released into the left atrium as well as the right atrium in humans*. J Am Coll Cardiol, 1990. **15**(7): p. 1537-43.
4. Raichle, M.E. and M.A. Mintun, *Brain work and brain imaging*. Annual Review of Neuroscience, 2006. **29**: p. 449-476.
5. Heeger, D.J. and D. Ress, *What does fMRI tell us about neuronal activity?* Nature Reviews Neuroscience, 2002. **3**(2): p. 142-151.
6. Villringer, A. and B. Chance, *Non-invasive optical spectroscopy and imaging of human brain function*. Trends Neurosci, 1997. **20**(10): p. 435-42.
7. White, B., *Developing high-density diffuse optical tomography for neuroimaging*. 2012.
8. Franceschini, M.A. and D.A. Boas, *Noninvasive measurement of neuronal activity with near-infrared optical imaging*. Neuroimage, 2004. **21**(1): p. 372-386.
9. Abia, D. and K. Okanoya, *Statistical segmentation of tone sequences activates the left inferior frontal cortex: a near-infrared spectroscopy study*. Neuropsychologia, 2008. **46**(11): p. 2787-95.
10. Lawrence, R.J., et al., *Cortical correlates of speech intelligibility measured using functional near-infrared spectroscopy (fNIRS)*. Hear Res, 2018. **370**: p. 53-64.
11. Saliba, J., et al., *Functional near-infrared spectroscopy for neuroimaging in cochlear implant recipients*. Hearing Research, 2016. **338**: p. 64-75.
12. Kirilina, E., et al., *The physiological origin of task-evoked systemic artefacts in functional near infrared spectroscopy*. Neuroimage, 2012. **61**(1): p. 70-81.
13. Obrig, H. and A. Villringer, *Beyond the visible--imaging the human brain with light*. J Cereb Blood Flow Metab, 2003. **23**(1): p. 1-18.
14. Gagnon, L., et al., *Quantification of the cortical contribution to the NIRS signal over the motor cortex using concurrent NIRS-fMRI measurements*. Neuroimage, 2012. **59**(4): p. 3933-40.
15. White, B.R. and J.P. Culver, *Quantitative evaluation of high-density diffuse optical tomography: in vivo resolution and mapping performance*. J Biomed. Opt, 2010. **15**(2): p. 026006.

16. Ferrari, M. and V. Quaresima, *A brief review on the history of human functional near-infrared spectroscopy (fNIRS) development and fields of application*. Neuroimage, 2012. **63**(2): p. 921-35.
17. Zeff, B.W., et al., *Retinotopic mapping of adult human visual cortex with high-density diffuse optical tomography*. Proc. Natl. Acad. Sci. U. S. A, 2007. **104**(29): p. 12169-12174.
18. Culver, J.P., et al., *Volumetric diffuse optical tomography of brain activity*. Opt Lett, 2003. **28**(21): p. 2061-3.
19. Joseph, D.K., et al., *Diffuse optical tomography system to image brain activation with improved spatial resolution and validation with functional magnetic resonance imaging*. Appl Opt, 2006. **45**(31): p. 8142-51.
20. Eggebrecht, A.T., et al., *Mapping distributed brain function and networks with diffuse optical tomography*. Nat. Photonics, 2014. **8**(6): p. 448-454.
21. Gregg, N.M., et al., *Brain specificity of diffuse optical imaging: improvements from superficial signal regression and tomography*. Front Neuroenergetics, 2010. **2**.
22. Hassanpour, M.S., et al., *Mapping cortical responses to speech using high-density diffuse optical tomography*. Neuroimage, 2015. **117**: p. 319-326.
23. Sherafati, A., Hassanpour, M. S., Eggebrecht, A. E., Culver, J. P. , Firszt, J. B., Peelle, J. E., *Optical Neuroimaging of Speech Perception in Listeners with Cochlear Implants*, in *ARO 2018 conference*. 2018: San Diego, United States.
24. Sherafati, A., et al., *Mapping deep brain stimulation's impact on cortical networks using high-density diffuse optical tomography (Conference Presentation)*. SPIE BiOS. Vol. 11226. 2020: SPIE.
25. Burke, B., et al. *Brain functional connectivity changes in acute ischemic stroke measured with bedside diffuse optical tomography*. in *JOURNAL OF CEREBRAL BLOOD FLOW AND METABOLISM*. 2019. SAGE PUBLICATIONS INC 2455 TELLER RD, THOUSAND OAKS, CA 91320 USA.
26. Eggebrecht, A.T. and J.P. Culver, https://github.com/WUSTL-ORL/NeuroDOT_Beta.
27. Cooper, R.J., et al., *A systematic comparison of motion artifact correction techniques for functional near-infrared spectroscopy*. Front Neurosci, 2012. **6**: p. 147.
28. Brigadoi, S., et al., *Motion artifacts in functional near-infrared spectroscopy: A comparison of motion correction techniques applied to real cognitive data*. Neuroimage, 2014. **85**: p. 181-191.
29. Sherafati, A., et al., *Global motion detection and censoring in high-density diffuse optical tomography*. Hum Brain Mapp, 2020.
30. Power, J.D., et al., *Spurious but systematic correlations in functional connectivity MRI networks arise from subject motion*. Neuroimage, 2012. **59**(3): p. 2142-2154.
31. Gratton, C., et al., *Emergent Functional Network Effects in Parkinson Disease*. Cereb Cortex, 2018.

32. Djourno, A. and C. Eyries, [*Auditory prosthesis by means of a distant electrical stimulation of the sensory nerve with the use of an indwelt coiling*]. La Presse medicale, 1957. **65**(63): p. 1417.
33. House, W.F., *Cochlear implants*. Ann Otol Rhinol Laryngol, 1976. **85 suppl 27**(3Pt2): p. 1-93.
34. Kral, A., et al., *Spatial resolution of cochlear implants: the electrical field and excitation of auditory afferents*. Hearing Research, 1998. **121**(1-2): p. 11-28.
35. McDermott, H.J. and C.M. McKay, *Pitch ranking with nonsimultaneous dual-electrode electrical stimulation of the cochlea*. J Acoust Soc Am, 1994. **96**(1): p. 155-62.
36. Firszt, J.B., et al., *Changes in auditory perceptions and cortex resulting from hearing recovery after extended congenital unilateral hearing loss*. Front Syst Neurosci, 2013. **7**: p. 108.
37. Firszt, J.B., et al., *Recognition of speech presented at soft to loud levels by adult cochlear implant recipients of three cochlear implant systems*. Ear Hear, 2004. **25**(4): p. 375-87.
38. Smith, A.M., M.C. Mancini, and S. Nie, *Bioimaging: second window for in vivo imaging*. Nat Nanotechnol, 2009. **4**(11): p. 710-1.
39. Boas, D., Franceschini, MA, *Near infrared imaging*. Scholarpedia, 2009: p. 6997.
40. Jobsis, F.F., *Noninvasive, infrared monitoring of cerebral and myocardial oxygen sufficiency and circulatory parameters*. Science, 1977. **198**(4323): p. 1264-7.
41. Arridge, S.R., M. Cope, and D.T. Delpy, *The theoretical basis for the determination of optical pathlengths in tissue: temporal and frequency analysis*. Phys Med Biol, 1992. **37**(7): p. 1531-60.
42. Yamada, Y., H. Suzuki, and Y.J.A.S. Yamashita, *Time-domain near-infrared spectroscopy and imaging: A review*. 2019. **9**(6): p. 1127.
43. Wang, L.V. and H.-i. Wu, *Biomedical optics: principles and imaging*. 2012: John Wiley & Sons.
44. Wheelock, M.D., J.P. Culver, and A.T. Eggebrecht, *High-density diffuse optical tomography for imaging human brain function*. Rev Sci Instrum, 2019. **90**(5): p. 051101.
45. Eggebrecht, A.T., et al., *A quantitative spatial comparison of high-density diffuse optical tomography and fMRI cortical mapping*. Neuroimage, 2012. **61**(4): p. 1120-1128.
46. Cui, X., S. Bray, and A.L. Reiss, *Functional near infrared spectroscopy (NIRS) signal improvement based on negative correlation between oxygenated and deoxygenated hemoglobin dynamics*. Neuroimage, 2010. **49**(4): p. 3039-3046.
47. Fishell, A.K., et al., *Mapping brain function during naturalistic viewing using high-density diffuse optical tomography*. Sci Rep, 2019. **9**(1): p. 11115.
48. Jahani, S., et al., *Motion artifact detection and correction in functional near-infrared spectroscopy: a new hybrid method based on spline interpolation method and Savitzky-Golay filtering*. Neurophotonics, 2018. **5**(1).

49. Eggebrecht, A.T., et al., *Mapping distributed brain function and networks with diffuse optical tomography*. Nature Photonics, 2014. **8**(6): p. 448-454.
50. Ferradal, S.L., et al., *Functional Imaging of the Developing Brain at the Bedside Using Diffuse Optical Tomography*. Cerebral Cortex, 2016. **26**(4): p. 1558-1568.
51. Biswal, B., et al., *Functional connectivity in the motor cortex of resting human brain using echo-planar MRI*. Magn Reson Med, 1995. **34**(4): p. 537-41.
52. Smyser, C.D., A.Z. Snyder, and J.J. Neil, *Functional connectivity MRI in infants: exploration of the functional organization of the developing brain*. Neuroimage, 2011. **56**(3): p. 1437-52.
53. Bluestone, A.Y., et al., *Three-dimensional optical tomography of hemodynamics in the human head*. Optics Express, 2001. **9**(6): p. 272-286.
54. Jermyn, M., et al., *Fast segmentation and high-quality three-dimensional volume mesh creation from medical images for diffuse optical tomography*. J Biomed Opt, 2013. **18**(8): p. 86007.
55. Eggebrecht, A.T., et al., *A quantitative spatial comparison of high-density diffuse optical tomography and fMRI cortical mapping*. Neuroimage, 2012. **61**(4): p. 1120-1128.
56. Dehghani, H., et al., *Near infrared optical tomography using NIRFAST: Algorithm for numerical model and image reconstruction*. 2009. **25**(6): p. 711-732.
57. Wray, S., et al., *Characterization of the near infrared absorption spectra of cytochrome aa3 and haemoglobin for the non-invasive monitoring of cerebral oxygenation*. 1988. **933**(1): p. 184-192.
58. White, B.R., et al., *Resting-state functional connectivity in the human brain revealed with diffuse optical tomography*. Neuroimage, 2009. **47**(1): p. 148-156.
59. Hassanpour, M.S., *Developing Diffuse Optical Tomography (DOT) for Neuroimaging of Speech Perception in People with Cochlear Implants*. 2015.
60. Fishell, A.K., et al. *Response Reproducibility and Functional Localization using High-Density Diffuse Optical Tomography During Naturalistic Viewing*. in *Biomedical Optics 2016*. 2016. Fort Lauderdale, Florida: Optical Society of America.
61. Farzam, P., et al., *Shedding light on the neonatal brain: probing cerebral hemodynamics by diffuse optical spectroscopic methods (vol 7, 15786, 2017)*. Scientific Reports, 2018. **8**.
62. Dashtestani, H., et al., *Canonical correlation analysis of brain prefrontal activity measured by functional near infra-red spectroscopy (fNIRS) during a moral judgment task*. 2019. **359**: p. 73-80.
63. Dashtestani, H., et al., *The role of prefrontal cortex in a moral judgment task using functional near-infrared spectroscopy*. Brain and Behavior, 2018: p. e01116.
64. Lloyd-Fox, S., A. Blasi, and C.E. Elwell, *Illuminating the developing brain: The past, present and future of functional near infrared spectroscopy*. Neuroscience and Biobehavioral Reviews, 2010. **34**(3): p. 269-284.

65. Liao, S.M., et al., *High-density diffuse optical tomography of term infant visual cortex in the nursery*. Journal of Biomedical Optics, 2012. **17**(8).
66. Morishita, T., et al., *Changes in Motor-Related Cortical Activity Following Deep Brain Stimulation for Parkinson's Disease Detected by Functional Near Infrared Spectroscopy: A Pilot Study*. Frontiers in Human Neuroscience, 2016. **10**.
67. Fishell, A.K., et al., *Portable, field-based neuroimaging using high-density diffuse optical tomography*. Neuroimage, 2020: p. 116541.
68. Salsabilian, S., et al. *Quantifying Changes in Brain Function Following Injury via Network Measures*. in *2019 41st Annual International Conference of the IEEE Engineering in Medicine and Biology Society (EMBC)*. 2019. IEEE.
69. Salsabilian, S., et al. *Study of Functional Network Topology Alterations after Injury via Embedding Methods*. in *Optics and the Brain*. 2020. Optical Society of America.
70. Khaksari, K., et al. *Effects of Performance and task duration on mental workload during working memory task*. in *Photonics*. 2019. Multidisciplinary Digital Publishing Institute.
71. Ferradal, S.L., et al., *Atlas-based head modeling and spatial normalization for high-density diffuse optical tomography: in vivo validation against fMRI*. Neuroimage, 2014. **85 Pt 1**: p. 117-26.
72. Wu, X., et al., *Quantitative evaluation of atlas-based high-density diffuse optical tomography for imaging of the human visual cortex*. Biomedical Optics Express, 2014. **5**(11): p. 3882-3900.
73. Siegel, J.S., et al., *Data Quality Influences Observed Links Between Functional Connectivity and Behavior*. Cereb Cortex, 2017. **27**(9): p. 4492-4502.
74. Fair, D.A., et al., *Distinct neural signatures detected for ADHD subtypes after controlling for micro-movements in resting state functional connectivity MRI data*. Front Syst Neurosci, 2012. **6**: p. 80.
75. Power, J.D., et al., *Temporal interpolation alters motion in fMRI scans: Magnitudes and consequences for artifact detection*. Plos One, 2017. **12**(9).
76. Satterthwaite, T.D., et al., *Impact of in-scanner head motion on multiple measures of functional connectivity: Relevance for studies of neurodevelopment in youth*. Neuroimage, 2012. **60**(1): p. 623-632.
77. Van Dijk, K.R.A., M.R. Sabuncu, and R.L. Buckner, *The influence of head motion on intrinsic functional connectivity MRI*. Neuroimage, 2012. **59**(1): p. 431-438.
78. Satterthwaite, T.D., et al., *An improved framework for confound regression and filtering for control of motion artifact in the preprocessing of resting-state functional connectivity data*. Neuroimage, 2013. **64**: p. 240-256.
79. Yan, C.G., et al., *A comprehensive assessment of regional variation in the impact of head micromovements on functional connectomics*. Neuroimage, 2013. **76**(1): p. 183-201.
80. Friston, K.J., et al., *Movement-related effects in fMRI time-series*. Magnetic Resonance in Medicine, 1996. **35**(3): p. 346-355.

81. Friston, K.J., et al., *Analysis of fMRI time-series revisited*. Neuroimage, 1995. **2**(1): p. 45-53.
82. Di Lorenzo, R., et al., *Recommendations for motion correction of infant fNIRS data applicable to multiple data sets and acquisition systems*. Neuroimage, 2019. **200**: p. 511-527.
83. Scholkmann, F., et al., *How to detect and reduce movement artifacts in near-infrared imaging using moving standard deviation and spline interpolation*. Physiological Measurement, 2010. **31**(5): p. 649-662.
84. Fishburn, F.A., et al., *Temporal Derivative Distribution Repair (TDDR): A motion correction method for fNIRS*. Neuroimage, 2019. **184**: p. 171-179.
85. Molavi, B. and G.A. Dumont, *Wavelet-based motion artifact removal for functional near-infrared spectroscopy*. Physiological Measurement, 2012. **33**(2): p. 259-270.
86. Chiarelli, A.M., et al., *A kurtosis-based wavelet algorithm for motion artifact correction of fNIRS data*. Neuroimage, 2015. **112**: p. 128-137.
87. Aghayee, S., et al., *Particle Tracking Facilitates Real Time Capable Motion Correction in 2D or 3D Two-Photon Imaging of Neuronal Activity*. Front Neural Circuits, 2017. **11**: p. 56.
88. Smyser, C.D., et al., *Longitudinal Analysis of Neural Network Development in Preterm Infants*. Cerebral Cortex, 2010. **20**(12): p. 2852-2862.
89. Sherafati, A., et al. *Improvements in functional diffuse optical tomography maps by global motion censoring techniques*. in *Biophotonics Congress: Biomedical Optics Congress 2018 (Microscopy/Translational/Brain/OTS)*. 2018. Hollywood, Florida: Optical Society of America.
90. Sherafati, A., et al. *A global metric to detect motion artifacts in optical neuroimaging data (Conference Presentation)*. in *Neural Imaging and Sensing*. 2017. International Society for Optics and Photonics.
91. Siegel, J.S., et al., *Statistical improvements in functional magnetic resonance imaging analyses produced by censoring high-motion data points*. Human Brain Mapping, 2014. **35**(5): p. 1981-1996.
92. Birn, R.M., R.W. Cox, and P.A. Bandettini, *Experimental designs and processing strategies for fMRI studies involving overt verbal responses*. Neuroimage, 2004. **23**(3): p. 1046-58.
93. Yucel, M.A., et al., *Targeted principle component analysis: A new motion artifact correction approach for near-infrared spectroscopy*. Journal of Innovative Optical Health Sciences, 2014. **7**(2).
94. Eggebrecht, A.T. and J.P. Culver. *NeuroDOT: An extensible Matlab toolbox for streamlined optical functional mapping*. in *Clinical and Preclinical Optical Diagnostics II*. 2019. Munich: Optical Society of America.
95. Eggebrecht, A.T. and J.P. Culver. https://github.com/WUSTL-ORL/NeuroDOT_Beta.
96. Snyder, A.Z., <https://readthedocs.org/projects/4dfp/>. 2019.

97. White, R.L., 3rd, et al., *Little Change in Functional Brain Networks Following Acute Levodopa in Drug-Naive Parkinson's Disease*. *Mov Disord*, 2019.
98. Hassanpour, M.S., et al., *Statistical analysis of high density diffuse optical tomography*. *Neuroimage*, 2014. **85 Pt 1**: p. 104-16.
99. Friston, K.J., A.P. Holmes, and K.J. Worsley, *How many subjects constitute a study?* *Neuroimage*, 1999. **10**(1): p. 1-5.
100. Power, J.D., et al., *Methods to detect, characterize, and remove motion artifact in resting state fMRI*. *Neuroimage*, 2014. **84**: p. 320-341.
101. Power, J.D., et al., *Steps toward optimizing motion artifact removal in functional connectivity MRI; a reply to Carp*. *Neuroimage*, 2013. **76**(1): p. 439-441.
102. Laumann, T.O., et al., *On the Stability of BOLD fMRI Correlations*. *Cereb Cortex*, 2017. **27**(10): p. 4719-4732.
103. Afyouni, S. and T.E. Nichols, *Insight and inference for DVARS*. *Neuroimage*, 2018. **172**: p. 291-312.
104. Zhang, Y.H., et al., *Eigenvector-based spatial filtering for reduction of physiological interference in diffuse optical imaging*. *Journal of Biomedical Optics*, 2005. **10**(1).
105. Yucel, M.A., et al., *Reducing motion artifacts for long-term clinical NIRS monitoring using collodion-fixed prism-based optical fibers*. *Neuroimage*, 2014. **85**: p. 192-201.
106. Metz, A.J., et al., *A New Approach for Automatic Removal of Movement Artifacts in Near-Infrared Spectroscopy Time Series by Means of Acceleration Data*. *Algorithms*, 2015. **8**(4): p. 1052-1075.
107. Izzetoglu, M., et al., *Motion artifact cancellation in NIR spectroscopy using Wiener filtering*. *Ieee Transactions on Biomedical Engineering*, 2005. **52**(5): p. 934-938.
108. Huppert, T.J., et al., *HomER: a review of time-series analysis methods for near-infrared spectroscopy of the brain*. *Applied Optics*, 2009. **48**(10): p. D280-D298.
109. Izzetoglu, M., et al., *Motion artifact cancellation in NIR spectroscopy using discrete Kalman filtering*. *Biomedical Engineering Online*, 2010. **9**.
110. Tanenbaum, A.B., et al., *A method for reducing the effects of motion contamination in arterial spin labeling magnetic resonance imaging*. *Journal of Cerebral Blood Flow and Metabolism*, 2015. **35**(10): p. 1697-1702.
111. Raut, R.V., et al., *On time delay estimation and sampling error in resting-state fMRI*. *Neuroimage*, 2019. **194**: p. 211-227.
112. Dosenbach, N.U.F., et al., *Real-time motion analytics during brain MRI improve data quality and reduce costs*. *Neuroimage*, 2017. **161**: p. 80-93.
113. Fair, D.A., et al., *Correction of respiratory artifacts in MRI head motion estimates*. *Neuroimage*, 2019. **208**: p. 116400.
114. Greene, D.J., et al., *Behavioral interventions for reducing head motion during MRI scans in children*. *Neuroimage*, 2018. **171**: p. 234-245.

115. Temperli, P., et al., *How do parkinsonian signs return after discontinuation of subthalamic DBS?* Neurology, 2003. **60**(1): p. 78-81.
116. Lozano, A.M. and N. Lipsman, *Probing and regulating dysfunctional circuits using deep brain stimulation.* Neuron, 2013. **77**(3): p. 406-24.
117. Ballanger, B., et al., *Stimulation of the subthalamic nucleus and impulsivity: release your horses.* Ann Neurol, 2009. **66**(6): p. 817-24.
118. Biseul, I., et al., *Fear recognition is impaired by subthalamic nucleus stimulation in Parkinson's disease.* Neuropsychologia, 2005. **43**(7): p. 1054-1059.
119. Campbell, M.C., et al., *Neural correlates of STN DBS-induced cognitive variability in Parkinson disease.* Neuropsychologia, 2008. **46**(13): p. 3162-3169.
120. Castelli, L., et al., *Chronic deep brain stimulation of the subthalamic nucleus for Parkinson's disease: effects on cognition, mood, anxiety and personality traits.* Eur. Neurol, 2006. **55**(3): p. 136-144.
121. Drapier, D., et al., *Emotion recognition impairment and apathy after subthalamic nucleus stimulation in Parkinson's disease have separate neural substrates.* Neuropsychologia, 2008. **46**(11): p. 2796-2801.
122. Eisenstein, S.A., et al., *Acute changes in mood induced by subthalamic deep brain stimulation in Parkinson disease are modulated by psychiatric diagnosis.* Brain Stimul, 2014. **7**(5): p. 701-8.
123. Frank, M.J., et al., *Hold your horses: impulsivity, deep brain stimulation, and medication in parkinsonism.* Science, 2007. **318**(5854): p. 1309-12.
124. Funkiewiez, A., et al., *Long term effects of bilateral subthalamic nucleus stimulation on cognitive function, mood, and behaviour in Parkinson's disease.* J. Neurol. Neurosurg. Psychiatry, 2004. **75**(6): p. 834-839.
125. Hershey, T., et al., *Mapping Go-No-Go performance within the subthalamic nucleus region.* Brain, 2010. **133**(Pt 12): p. 3625-34.
126. Hershey, T., et al., *Unilateral vs. bilateral STN DBS effects on working memory and motor function in Parkinson disease.* Exp. Neurol, 2007.
127. Jahanshahi, M., et al., *The impact of deep brain stimulation on executive function in Parkinson's disease.* Brain, 2000. **123** (Pt 6): p. 1142-1154.
128. Fox, M.D., et al., *Resting-state networks link invasive and noninvasive brain stimulation across diverse psychiatric and neurological diseases.* Proc Natl Acad Sci U S A, 2014. **111**(41): p. E4367-75.
129. Sammartino, F., et al., *3-Tesla MRI in patients with fully implanted deep brain stimulation devices: a preliminary study in 10 patients.* J Neurosurg, 2017. **127**(4): p. 892-898.
130. Alhourani, A., et al., *Network Effects of Deep Brain Stimulation.* J Neurophysiol, 2015: p. jn.

131. Horn, A., et al., *Connectivity Predicts deep brain stimulation outcome in Parkinson disease*. Ann Neurol, 2017. **82**(1): p. 67-78.
132. Albaugh, D.L. and Y.Y. Shih, *Neural circuit modulation during deep brain stimulation at the subthalamic nucleus for Parkinson's disease: what have we learned from neuroimaging studies?* Brain Connect, 2014. **4**(1): p. 1-14.
133. Zrinzo, L., et al., *Clinical safety of brain magnetic resonance imaging with implanted deep brain stimulation hardware: large case series and review of the literature*. World Neurosurg, 2011. **76**(1-2): p. 164-72; discussion 69-73.
134. Gupte, A.A., et al., *MRI-related heating near deep brain stimulation electrodes: more data are needed*. Stereotact Funct Neurosurg, 2011. **89**(3): p. 131-40.
135. Ferradal, S.L., et al., *Functional Imaging of the Developing Brain at the Bedside Using Diffuse Optical Tomography*. Cereb. Cortex, 2015.
136. Ferradal, S.L., et al., *Atlas-based head modeling and spatial normalization for high-density diffuse optical tomography: in vivo validation against fMRI*. Neuroimage, 2014. **85 Pt 1**: p. 117-126.
137. Hassanpour, M.S., et al., *Statistical analysis of high density diffuse optical tomography*. Neuroimage, 2014. **85 Pt 1**: p. 104-116.
138. Wu, X., et al., *Evaluation of rigid registration methods for whole head imaging in diffuse optical tomography*. Neurophotonics, 2015. **2**(3): p. 035002.
139. Wu, X., et al., *Quantitative evaluation of atlas-based high-density diffuse optical tomography for imaging of the human visual cortex*. Biomed. Opt. Express, 2014. **5**(11): p. 3882-3900.
140. Zhan, Y., et al., *Image quality analysis of high-density diffuse optical tomography incorporating a subject-specific head model*. Front Neuroenergetics, 2012. **4**: p. 6.
141. Fishell, A.K., *High-Density Diffuse Optical Tomography During Passive Movie Viewing: A Platform for Naturalistic Functional Brain Mapping*. 2019.
142. Racette, B.A., et al., *Evaluation of a screening questionnaire for genetic studies of Parkinson's disease*. Am. J. Med. Genet, 1999. **88**(5): p. 539-543.
143. Bain, P., et al., *Criteria for the diagnosis of essential tremor*. Neurology, 2000. **54**(11 Suppl 4): p. S7.
144. Hershey, T., et al., *Stimulation of STN impairs aspects of cognitive control in PD*. Neurology, 2004. **62**(7): p. 1110-1114.
145. Hershey, T., et al., *Cortical and subcortical blood flow effects of subthalamic nucleus stimulation in PD*. Neurology, 2003. **61**(6): p. 816-821.
146. Beckmann, C.F., et al., *Investigations into resting-state connectivity using independent component analysis*. Philos Trans R Soc Lond B Biol Sci, 2005. **360**(1457): p. 1001-13.
147. Power, J.D., et al., *Functional network organization of the human brain*. Neuron, 2011. **72**(4): p. 665-78.

148. Zhang, D. and M.E. Raichle, *Disease and the brain's dark energy*. Nat Rev Neurol, 2010. **6**(1): p. 15-28.
149. Markham, J., et al., *Blind identification of evoked human brain activity with independent component analysis of optical data*. Hum Brain Mapp, 2009. **30**(8): p. 2382-92.
150. Fahn, S., R.L. Elton, and M.o.t.U.D. Committee, *Unified Parkinson's disease rating scale*, in *Recent developments in Parkinson's disease*, S. Fahn, et al., Editors. 1987, Macmillan: New York. p. 153-163.
151. Heldman, D.A., et al., *The modified bradykinesia rating scale for Parkinson's disease: reliability and comparison with kinematic measures*. Mov Disord, 2011. **26**(10): p. 1859-1863.
152. Heldman, D.A., et al., *Essential tremor quantification during activities of daily living*. Parkinsonism. Relat Disord, 2011. **17**(7): p. 537-542.
153. Heldman, D.A., et al., *Clinician versus machine: reliability and responsiveness of motor endpoints in Parkinson's disease*. Parkinsonism. Relat Disord, 2014. **20**(6): p. 590-595.
154. Stamatakis, J., et al., *Finger tapping clinimetric score prediction in Parkinson's disease using low-cost accelerometers*. Comput. Intell. Neurosci, 2013. **2013**: p. 717853.
155. Ushe, M., et al., *Effect of stimulation frequency on tremor suppression in essential tremor*. Movement Disorders, 2004. **19**(10): p. 1163-1168.
156. Tabbal, S.D., et al., *Unilateral subthalamic nucleus stimulation has a measurable ipsilateral effect on rigidity and bradykinesia in Parkinson disease*. Experimental Neurology, 2008. **211**(1): p. 234-242.
157. Zadikoff, C., et al., *A comparison of the mini mental state exam to the Montreal cognitive assessment in identifying cognitive deficits in Parkinson's disease*. Mov Disord, 2008. **23**(2): p. 297-299.
158. Nasreddine, Z.S., et al., *The Montreal Cognitive Assessment, MoCA: a brief screening tool for mild cognitive impairment*. J Am Geriatr Soc, 2005. **53**(4): p. 695-9.
159. Wechsler, D., *Wechsler Test of Adult Reading Manual*. 2001, San Antonio, TX: The Psychological Corporation.
160. Chafee, M. and P.S. Goldman-Rakic, *Prefrontal cooling dissociated memory- and sensory-guided oculomotor delayed response functions*. Abstracts of the Society for Neuroscience, 1994. **20**(808).
161. Friedman, H.R. and P.S. Goldman-Rakic, *The circuitry of working memory revealed by anatomy and metabolic imaging*, in *Frontal Lobe Function and Dysfunction*, H.S. Levin, H.M. Eisenberg, and A.L. Benton, Editors. 1991, Oxford University Press: New York. p. 72-91.
162. Funahashi, S., C.J. Bruce, and P.S. Goldman-Rakic, *Mnemonic coding of visual space in the monkey's dorsolateral prefrontal cortex*. Journal of Neurophysiology, 1989. **61**(2): p. 331-349.
163. Goldman-Rakic, P.S., *Cellular and circuit basis of working memory in prefrontal cortex of nonhuman primates*. Prog. Brain Res, 1990. **85**: p. 325-335.

164. McCarthy, G., et al., *Activation of human prefrontal cortex during spatial and nonspatial working memory tasks measured by functional MRI*. Cereb. Cortex, 1996. **6**(4): p. 600-611.
165. Hershey, T., et al., *Dopaminergic modulation of response inhibition: An fMRI study*. Cognitive Brain Research, 2004. **20**(3): p. 438-448.
166. Beste, C., et al., *Response inhibition subprocesses and dopaminergic pathways: basal ganglia disease effects*. Neuropsychologia, 2010. **48**(2): p. 366-73.
167. Greenhouse, I., et al., *Stimulation at dorsal and ventral electrode contacts targeted at the subthalamic nucleus has different effects on motor and emotion functions in Parkinson's disease*. Neuropsychologia, 2011. **49**(3): p. 528-34.
168. Aron, A.R. and R.A. Poldrack, *Cortical and subcortical contributions to Stop signal response inhibition: role of the subthalamic nucleus*. J Neurosci, 2006. **26**(9): p. 2424-33.
169. Obeso, I., et al., *Bilateral stimulation of the subthalamic nucleus has differential effects on reactive and proactive inhibition and conflict-induced slowing in Parkinson's disease*. Exp Brain Res, 2013. **226**(3): p. 451-62.
170. Eggebrecht, A.T., et al., *Joint Attention and Brain Functional Connectivity in Infants and Toddlers*. Cereb Cortex, 2017. **27**(3): p. 1709-1720.
171. Min, H.K., et al., *Deep brain stimulation induces BOLD activation in motor and non-motor networks: an fMRI comparison study of STN and EN/GPi DBS in large animals*. Neuroimage, 2012. **63**(3): p. 1408-20.
172. Karimi, M., et al., *Subthalamic nucleus stimulation-induced regional blood flow responses correlate with improvement of motor signs in Parkinson disease*. Brain, 2008.
173. Perlmutter, J.S., et al., *Blood flow responses to deep brain stimulation of thalamus*. Neurology, 2002. **58**(9): p. 1388-1394.
174. Fukuda, M., et al., *Networks mediating the clinical effects of pallidal brain stimulation for Parkinson's disease: a PET study of resting-state glucose metabolism*. Brain, 2001. **124**(Pt 8): p. 1601-1609.
175. Fukuda, M., et al., *Thalamic stimulation for parkinsonian tremor: correlation between regional cerebral blood flow and physiological tremor characteristics*. Neuroimage, 2004. **21**(2): p. 608-615.
176. Trost, M., et al., *Network modulation by the subthalamic nucleus in the treatment of Parkinson's disease*. Neuroimage, 2006. **31**(1): p. 301-307.
177. McCulloch, J., *Mapping functional alterations in the CNS with [14C]deoxyglucose*, in *Handbook of Psychopharmacology: New Techniques in Psychopharmacology*, L.L. Iverson, S.D. Iverson, and S.H. Snyder, Editors. 1982, Plenum: New York. p. 321-410.
178. Schwartz, W.J., et al., *Metabolic mapping of functional activity in the hypothalamo-neurohypophyseal system of the rat*. Science, 1979. **205**(4407): p. 723-725.
179. Raichle, M.E., *Circulatory and metabolic correlates of brain function in normal humans*, in *Handbook of physiology: The nervous system*, F. Plum, Editor. 1987, American Physiological Society: Bethesda. p. 643-674.

180. Lauritzen, M., *Relationship of spikes, synaptic activity, and local changes of cerebral blood flow*. J. Cereb. Blood Flow Metab, 2001. **21**(12): p. 1367-1383.
181. Gold, L. and M. Lauritzen, *Neuronal deactivation explains decreased cerebellar blood flow in response to focal cerebral ischemia or suppressed neocortical function*. Proc. Natl. Acad. Sci. U. S. A, 2002. **99**(11): p. 7699-7704.
182. Black, K.J., M.H. Gado, and J.S. Perlmutter, *PET measurement of dopamine D2 receptor-mediated changes in striatopallidal function*. Journal of Neuroscience, 1997. **17**(9): p. 3168-3177.
183. Jueptner, M. and C. Weiller, *Review: does measurement of regional cerebral blood flow reflect synaptic activity? Implications for PET and fMRI*. Neuroimage, 1995. **2**: p. 148-156.
184. Shimamoto, S.A., et al., *Subthalamic nucleus neurons are synchronized to primary motor cortex local field potentials in Parkinson's disease*. J Neurosci, 2013. **33**(17): p. 7220-33.
185. Li, Q., et al., *Therapeutic deep brain stimulation in Parkinsonian rats directly influences motor cortex*. Neuron, 2012. **76**(5): p. 1030-41.
186. Ng, B., et al., *Distinct alterations in Parkinson's medication-state and disease-state connectivity*. Neuroimage Clin, 2017. **16**: p. 575-585.
187. Mueller, K., et al., *Brain connectivity changes when comparing effects of subthalamic deep brain stimulation with levodopa treatment in Parkinson's disease*. Neuroimage Clin, 2018. **19**: p. 1025-1035.
188. Fukuda, M., et al., *Functional correlates of pallidal stimulation for Parkinson's disease*. Ann Neurol, 2001. **49**(2): p. 155-164.
189. Andrews-Hanna, J.R., et al., *Disruption of large-scale brain systems in advanced aging*. Neuron, 2007. **56**(5): p. 924-935.
190. Bero, A.W., et al., *Neuronal activity regulates the regional vulnerability to amyloid-beta deposition*. Nat. Neurosci, 2011.
191. Brier, M.R., et al., *Loss of Intranetwork and Internetwork Resting State Functional Connections with Alzheimer's Disease Progression*. Journal of Neuroscience, 2012. **32**(26): p. 8890-8899.
192. Sheline, Y.I., et al., *Amyloid plaques disrupt resting state default mode network connectivity in cognitively normal elderly*. Biol. Psychiatry, 2010. **67**(6): p. 584-587.
193. Vlassenko, A.G., et al., *Spatial correlation between brain aerobic glycolysis and amyloid-beta (A β) deposition*. Proc. Natl. Acad. Sci. U. S. A, 2010. **107**(41): p. 17763-17767.
194. Badea, L., et al., *Exploring the reproducibility of functional connectivity alterations in Parkinson's disease*. PLoS One, 2017. **12**(11): p. e0188196.
195. Kahan, J., et al., *The Safety of Using Body-Transmit MRI in Patients with Implanted Deep Brain Stimulation Devices*. PLoS. One, 2015. **10**(6): p. e0129077.

196. Kahan, J., et al., *Therapeutic subthalamic nucleus deep brain stimulation reverses cortico-thalamic coupling during voluntary movements in Parkinson's disease*. PLoS. One, 2012. **7**(12): p. e50270.
197. Saenger, V.M., et al., *Uncovering the underlying mechanisms and whole-brain dynamics of deep brain stimulation for Parkinson's disease*. Sci Rep, 2017. **7**(1): p. 9882.
198. Uitti, R.J., et al., *Magnetic resonance imaging and deep brain stimulation*. Neurosurgery, 2002. **51**(6): p. 1423-1428.
199. Georgi, J.C., et al., *Active deep brain stimulation during MRI: A feasibility study*. Magn Reson. Med, 2004. **51**(2): p. 380-388.
200. Hershey, T., et al., *Regional blood flow changes induced by l-DOPA methyl ester in normal monkeys*. Abstracts of the Society for Neuroscience, 1997. **23**(Part 2): p. 2038.
201. Hill, K.K., et al., *Cerebral blood flow responses to dorsal and ventral STN DBS correlate with gait and balance responses in Parkinson's disease*. Exp Neurol, 2013. **241**: p. 105-12.
202. Hassanpour, M.S., et al., *Mapping effective connectivity within cortical networks with diffuse optical tomography*. Neurophotonics, 2017. **4**(4): p. 041402.
203. Rastogi, A., et al., *Modulation of cognitive cerebello-cerebral functional connectivity by lateral cerebellar continuous theta burst stimulation*. Neuroimage, 2017. **158**: p. 48-57.
204. Wong, D., et al., *PET imaging of cochlear-implant and normal-hearing subjects listening to speech and nonspeech*. Hear Res, 1999. **132**(1-2): p. 34-42.
205. Firszt, J.B., et al., *Speech recognition in cochlear implant recipients: comparison of standard HiRes and HiRes 120 sound processing*. Otol Neurotol, 2009. **30**(2): p. 146-52.
206. Peelle, J.E., *Listening Effort: How the Cognitive Consequences of Acoustic Challenge Are Reflected in Brain and Behavior*. Ear Hear, 2018. **39**(2): p. 204-214.
207. Van Engen, K.J. and J.E. Peelle, *Listening effort and accented speech*. Front Hum Neurosci, 2014. **8**: p. 577.
208. Wild, C.J., et al., *Effortful listening: the processing of degraded speech depends critically on attention*. J Neurosci, 2012. **32**(40): p. 14010-21.
209. McKay, C.M., et al., *Connectivity in Language Areas of the Brain in Cochlear Implant Users as Revealed by fNIRS*. Physiology, Psychoacoustics and Cognition in Normal and Impaired Hearing, 2016. **894**: p. 327-335.
210. Mushtaq, F., et al., *Evaluating time-reversed speech and signal-correlated noise as auditory baselines for isolating speech-specific processing using fNIRS*. PLoS One, 2019. **14**(7): p. e0219927.
211. Plichta, M.M., et al., *Auditory cortex activation is modulated by emotion: A functional near-infrared spectroscopy (fNIRS) study*. Neuroimage, 2011. **55**(3): p. 1200-1207.
212. Rowland, S.C., D.E.H. Hartley, and I.M. Wiggins, *Listening in Naturalistic Scenes: What Can Functional Near-Infrared Spectroscopy and Intersubject Correlation Analysis Tell Us About the Underlying Brain Activity?* Trends Hear, 2018. **22**: p. 2331216518804116.

213. Sevy, A.B.G., et al., *Neuroimaging with near-infrared spectroscopy demonstrates speech-evoked activity in the auditory cortex of deaf children following cochlear implantation*. Hearing Research, 2010. **270**(1-2): p. 39-47.
214. Weder, S., et al., *Cortical Processing Related to Intensity of a Modulated Noise Stimulus- a Functional Near-Infrared Study*. J Assoc Res Otolaryngol, 2018. **19**(3): p. 273-286.
215. Wiggins, I.M., et al., *Speech-evoked activation in adult temporal cortex measured using functional near-infrared spectroscopy (fNIRS): Are the measurements reliable?* Hear Res, 2016. **339**: p. 142-54.
216. Wiggins, I.M. and D.E. Hartley, *A synchrony-dependent influence of sounds on activity in visual cortex measured using functional near-infrared spectroscopy (fNIRS)*. PLoS One, 2015. **10**(3): p. e0122862.
217. Wijayasiri, P., D.E.H. Hartley, and I.M. Wiggins, *Brain activity underlying the recovery of meaning from degraded speech: A functional near-infrared spectroscopy (fNIRS) study*. Hear Res, 2017. **351**: p. 55-67.
218. Zhou, X., et al., *Cortical Speech Processing in Postlingually Deaf Adult Cochlear Implant Users, as Revealed by Functional Near-Infrared Spectroscopy*. Trends in Hearing, 2018. **22**.
219. Eggebrecht, A.T., et al., *A quantitative spatial comparison of high-density diffuse optical tomography and fMRI cortical mapping*. Neuroimage, 2012. **61**(4): p. 1120-8.
220. Fishell, A.K., et al., *Mapping brain function during naturalistic viewing using high-density diffuse optical tomography*. Scientific Reports, 2019. **9**.
221. Hassanpour, M.S., et al., *Mapping effective connectivity within cortical networks with diffuse optical tomography*. Neurophotonics, 2017. **4**(4).
222. Schroeder, M.L., et al. *Cortical activity underlying overt and covert language generation measured using high-density diffuse optical tomography*. in *Clinical and Preclinical Optical Diagnostics II*. 2019. Munich: Optical Society of America.
223. Peelle, J.E., I.S. Johnsrude, and M.H. Davis, *Hierarchical processing for speech in human auditory cortex and beyond*. Front Hum Neurosci, 2010. **4**: p. 51.
224. Brainard, D.H., *The Psychophysics Toolbox*. Spatial vision, 1997. **10**(4): p. 433-436.
225. Spahr, A.J., et al., *Development and validation of the pediatric AzBio sentence lists*. Ear Hear, 2014. **35**(4): p. 418-22.
226. Shannon, R.V., et al., *Speech recognition with primarily temporal cues*. Science, 1995. **270**(5234): p. 303-4.
227. Hassanpour, M., *Developing Diffuse Optical Tomography (DOT) for Neuroimaging of Speech Perception in People with Cochlear Implants*. 2015.
228. Fedorenko, E., J. Duncan, and N. Kanwisher, *Broad domain generality in focal regions of frontal and parietal cortex*. Proc Natl Acad Sci U S A, 2013. **110**(41): p. 16616-21.

229. Fedorenko, E., M.K. Behr, and N. Kanwisher, *Functional specificity for high-level linguistic processing in the human brain*. Proc Natl Acad Sci U S A, 2011. **108**(39): p. 16428-33.
230. Sherafati, A., et al., *Global Motion Detection and Censoring in High-Density Diffuse Optical Tomography*. 2020: p. 2020.02.22.961219.
231. Smith, S.M., et al., *Advances in functional and structural MR image analysis and implementation as FSL*. Neuroimage, 2004. **23**: p. S208-S219.
232. Woolrich, M.W., et al., *Bayesian analysis of neuroimaging data in FSL*. Neuroimage, 2009. **45**(1 Suppl): p. S173-86.
233. Wilson, S.M., I. Molnar-Szakacs, and M.J.C.c. Iacoboni, *Beyond superior temporal cortex: intersubject correlations in narrative speech comprehension*. 2008. **18**(1): p. 230-242.